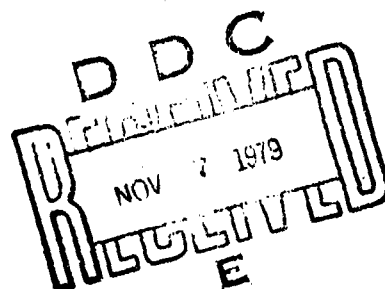AFRPL-TR-79-55

AD A076199

LEVEL

DEVELOPMENT AND VALIDATION OF STANDARDIZED

INFRARED RADIATION MODEL (SIRRM)

GAS/PARTICLE RADIATION TRANSFER MODEL

Prepared by:

PHOTON RESEARCH ASSOCIATES, INC.
2223 AVENIDA DE LA PLAYA/SUITE 301
LA JOLLA, CA 92037
and
GRUMMAN AEROSPACE CORPORATION
SOUTH OYSTER BAY ROAD
BETHPAGE, L.I., N.Y. 11714

Authors:

G. N. FREEMAN (PRA)
C. B. LUDWIG (PRA)
W. MALKMUS (PRA)
R. REED (GAC)

D D C

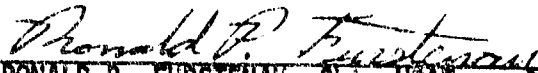NOV 7 1979

E

OCTOBER 1979

DDC FILE COPY

N O T I C E S

When U. S. Government drawings, specifications, or other data are used for any purpose other than a definitely related Government procurement operation, the Government thereby incurs no responsibility nor any obligation whatsoever, and the fact that the Government may have formulated, furnished, or in any way supplied the said drawings, specifications, or other data is not to be regarded by implication or otherwise, or in any manner licensing the holder or any other person or corporation, or conveying any rights or permission to manufacture, use or sell any patented invention that may in any way be related hereto.

F O R E W O R D

This report was submitted by Photon Research Associates, Inc., La Jolla, CA 92037, under Contract No. F04611-78-C-0081 with the Air Force Rocket Propulsion Laboratory, Edwards AFB, CA 93523. The report documents the development of gas/particle radiative transfer model techniques as part of the Standardized InfraRed Radiation Model (SIRRM) during the time period from September 18, 1978 to June 30, 1979, under Air Force Project Task 305813BB.
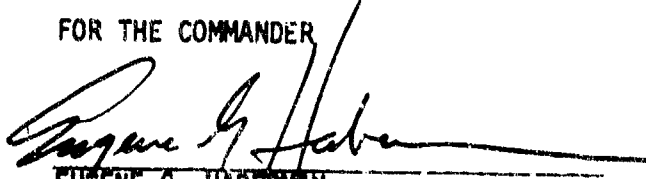
The program manager and principal investigator is C. B. Ludwig and the co-investigators of this phase of the program covered in this report are G. N. Freeman and W. Malkmus (Photon Research Associates, Inc.) and M. Slack and R. Reed (Grumman Aerospace Corporation).

This report has been reviewed, and is approved for publication in accordance with the distribution statement on the cover, and on the DD Form 1473.

RONALD P. FURSTENAU, 2Lt, USAF
Project Manager

DAVID M. MANN
Chief, Plume Technology Section

FOR THE COMMANDER

EUGENE G. HABERMAN
Chief, Propulsion Analysis Division

PREFACE

REPORT DOCUMENTATION PAGE	READ INSTRUCTIONS BEFORE COMPLETING FORM

1. REPORT NUMBER	2. GOVT ACCESSION NO.	3. RECIPIENT'S CATALOG NUMBER
AFRPL-TR-79-55		

4. TITLE (and Subtitle)

DEVELOPMENT AND VALIDATION OF STANDARDIZED INFRARED RADIATION MODEL (SIRRM).

Gas/Particle Radiative Transfer Model.

5. TYPE OF REPORT & PERIOD COVERED

Computer Code Development rept.
8 Sep 78 — 30 Jun 79

6. PERFORMING ORG. REPORT NUMBER

7. AUTHOR(s)

G. N. Freeman (PRA)
C. B. Ludwig (PRA)
W. Malkmus (PRA)
R. Reed (GAC)

8. CONTRACT OR GRANT NUMBER(s)

F04611-78-C-0081

9. PERFORMING ORGANIZATION NAME AND ADDRESS

Photon Research Associates, Inc.
2223 Avenida de la Playa - Suite 301
La Jolla, CA 92037

10. PROGRAM ELEMENT, PROJECT, TASK AREA & WORK UNIT NUMBERS

JON: 3058 3BB 13

11. CONTROLLING OFFICE NAME AND ADDRESS

Air Force Rocket Propulsion Laboratory
PACP
Edwards Air Force Base, CA 93523

12. REPORT DATE

30 Oct 79

13. NUMBER OF PAGES

164

14. MONITORING AGENCY NAME & ADDRESS(if different from Controlling Office)	15. SECURITY CLASS. (of this report)
	UNCLASSIFIED
	15a. DECLASSIFICATION/DOWNGRADING SCHEDULE

16. DISTRIBUTION STATEMENT (of this Report)

Approved for public release; distribution unlimited.

17. DISTRIBUTION STATEMENT (of the abstract entered in Block 20, if different from Report)

18. SUPPLEMENTARY NOTES

19. KEY WORDS (Continue on reverse side if necessary and identify by block number)

Rocket Plumes
Computer Code
Infrared Signature

Particle/Gas Radiation
Band Model
Optical Parameters

20. ABSTRACT (Continue on reverse side if necessary and identify by block number)

Analytical models have been developed to treat the coupled gas/particle radiative transfer in exhaust plumes, monochromatically and in a band model approach. In addition, the availability of the particle optical parameters has been investigated.

The requirements for the plume scattering model in SIRRM are:
- Coupled emission, absorption and scattering treatment
- Multiple scattering with cylindrical geometry

DD FORM 1JAN 73 1473   EDITION OF 1 NOV 65 IS OBSOLETE

410 443

- Three-dimensional, non-uniform, axisymmetric medium
- Arbitrary particle mixtures and size distribution
- Line-by-line and band-model treatments
- Alternate levels of engineering approximation

These requirements are met by developing two basic approaches, a 6-flux
and a N-flux approach. This distinction refers to the associated sub-
division in angular space, six-orthogonal coordinates versus N non-
orthogonal coordinates in azimuth and elevation, thus providing the alter-
natives of computational simplicity of the 6-flux model with generality of
the N-flux model. Numerous parametric calculations were performed to study
the effect of optical depth, scattering albedo, phase function and medium
geometry on the target signature and computational requirements. Comparisons
with independent calculations such as the two-dimensional Monte Carlo
method were made. The results show the different degrees of accuracy
achievable with the various models as functions of the radiation field
parameters. To the authors' knowledge, the N-flux model represents the
first application of general finite-element techniques to emitting cylin-
drical media. It provides a powerful tool for the analysis of plume
scattering problems of arbitrary complexity. The accuracy of the prediction
is limited only by the computational resources of the user.

The solution of the equation of radiative transfer is derived on a mono-
chromatic basis. For the application to the finite spectral intervals
associated with the use of instruments with finite resolution, spectral
averaging procedures are required. Thus, an extension of earlier band model
formalisms for regular and random arrays of spectral lines was developed
to include scattering as well as absorption in a medium in which radiative
transfer is described by the two-flux method. Representations of the
averaged transmissivity for the Elsasser model and the random model with
exponential-tailed S^{-1} line intensity distribution were derived and
numerical results were obtained for large ranges of optical depths of
absorbing and scattering media. The effects of inhomogeneities away from
the line-of-sight are accounted for by a contribution to the source
function which is calculated by a simplified six-flux technique.

A survey of available optical parameters (complex index of refraction as
a function of wavelength and temperature) was made for particles of interest.
The compilation by Aerospace was found useful as a starting base for a
number of relevant species, namely carbon, aluminum oxide, magnesium oxide
and zirconium oxide. Data for other species must yet be obtained. The
complex indices of refraction for carbon and aluminum oxide were used,
together with postulated size distributions, to calculate the volume ex-
tinction, scattering and absorption coefficients and the angular scattering
phase function by the Mie Theory for homogeneous, spherical particles in
the 1-25μm wavelength region. Based on these results, a tentative plan
was developed for the organization of the Data File and its integration into
the overall code architecture.

TABLE OF CONTENTS

1

INTRODUCTION

Validated models to predict rocket plume IR signatures must be capable of treating a wide range of propulsion and trajectory parameters as well as handling a number of sensor-related variables. While significant advances have been made in the state-of-knowledge of plume-related radiative transport phenomenologies during the last ten years, particularly in regard to advanced liquid propellants, prediction methods have not been developed to adequately treat the coupling of gas and particle radiative transfer in the plumes of solid propellant missiles. It is particularly important that models be developed to accurately treat plumes containing scattering particles while at the same time also yielding accurate results for conventional liquid propellant plumes.

The primary goals of the SIRRM program are (i) to develop an analytical methodology to treat coupled gas/particle radiative transport effects and (ii) to integrate this analytical capability together with the state-of-the-art treatments in hot gas/atmospheric radiative transport (i.e., band model methodologies, band model parameters, line-by-line methodologies, spectral line parameters) into a comprehensive, user-oriented plume radiation model.

State-of-the-art plume signature predictions require four
basic steps. First, the species concentrations and temperature
in the exit plane are calculated through a combustion/nozzle
code. Second, these exit plane parameters are input to a gas-
dynamic code which calculates the exhaust plume flow field.
Third, the flow field serves as input to a radiation code that
calculates the intrinsic plume signature. Finally, the apparent
plume signature viewed by a remote observer sensor is obtained
through attenuating the source intensity by the atmospheric
absorption. When the source radiation is correlated with the
atmospheric attenuation (radiating plume species are also present
in the atmosphere as absorbers), the last two steps are combined
into a single calculation.

The present study focuses on the third and fourth component,
i.e., the calculation of the intrinsic and apparent plume signatures.
The program is divided into four major tasks. Task I calls for
the formulation of the SIRRM code methodology. In Task II, the
code is to be developed and its capabilities demonstrated. The
validation and application of SIRRM takes place in Task III. The
documentation and code acceptance is done in Task IV.

Task I is concerned with the development of an integrated
physical model which accounts for the essential spectroscopic
and geometric effects governing single and multiple photon

interactions in a two-phase gas-particle mixture. A key
element in this task is the theoretical description of coupling
phenomena associated with the spectral and spatial redistribution
of radiation by scattering. In order to provide a correct
description, the model must account for the interaction of
emitted, absorbed, and scattered radiation from line and continuum
sources along multiple, intersecting paths, The task is divided
into two subtasks. Subtask IA deals with the development of
the coupled, multi-scattering model, while Subtask IB calls for
the formulation of the overall methodology, i.e., the integration
of the scattering model with the other parts of the code. This
document is an interim technical report describing the development
of the coupled multi-scattering model performed under Subtask IA.

Section 2 contains the description of our efforts in deve-
loping the multi-scattering model with cylindrical geometry,
using both engineering approximations (six-flux) and exact
solutions (N-flux). Diagnostic calculations with these models
and comparisons of the results with those obtained by independent
codes indicate that the required objectives have been met.

Since the present scattering model is developed for the
monochromatic case, a parallel study was begun to treat the
spectral averaging. The step forward to a band-model formulation
coupling particle scattering with spectral line absorption is
taken in Section 3, where the Elsasser and random model formulations

are developed for a two-flux scattering model and conceptual
approaches for the six-flux and N-flux models are outlined.

The fundamental inputs into any scattering models are
the optical parameters of the particles. These are discussed
in Section 4, including the Mie theory, the indices of refraction
and absorption, the scattering due to single particles and
particle size distributions, and the handling of the Data File
as it would be integrated into the overall code architecture.

2

SCATTERING MODEL

2.1 Introduction

The objective of Task IA is to formulate a scattering model that incorporates the following capabilities:

- Coupled emission, absorption and scattering treatment
- Multiple scattering with cylindrical geometry
- Three-dimensional, non-uniform, axisymmetric medium
- Arbitrary particle mixtures and size distributions
- Arbitrary angular scattering phase function
- Line-by-line and band-model treatments
- Alternate levels of engineering approximation

The approach to meet these objectives is described in this section. Our efforts included (i) the selection of physical models and solution methods for the gas/particle radiation transfer problems, (ii) the justification of selected models and methods by means of diagnostic calculations, and (iii) the final development of the selected models and methods for integration into SIRRM.

In Section 2.2, we provide the requisite technical background, beginning with the equation of radiative transfer and its implicit and explicit solution schemes.

In Section 2.3, we review and assess the combined inter-disciplinary experience of contributors in several fields (e.g., planetary and stellar atmospheric physics, radiant heat transfer, plume physics) where multiple scattering techniques have reached an advanced stage of development. Based on this assessment we select the most appropriate approach to the plume problem, and justify this selection on the basis of key physical requirements and model capabilities. The discussion presented in this section formed one of the essential elements of the Program Plan (Data Item 1).

The other essential element of the Program Plan was a set of recommendations for the final development of the scattering model to be incorporated into SIRRM. Since January 25, 1979, the recommendations were followed and the results of developing engineering approximations and the N-flux model are reported in Sections 2.4 and 2.5, respectively, together with numerical results of diagnostic and parametric calculations.

The comparisons of the computational results between the different models developed in the present program and with in-dependent model calculations are made in Section 2.6. Conclusions about the models and the results are summarized in Section 2.7.

2.2 Scattering Theory

The transfer of radiant energy through matter that emits, absorbs, and scatters radiation was first described by astro-physicists at the beginning of this century. The governing

equation was derived by specializing the Boltzmann equation of kinetic theory to the case of photons. To this day, the original formulation remains essentially unchanged. However, the range of problems amenable to exact solution is quite small, and for most cases of interest an approximate treatment is required.

The formal solution to the equation of transfer provides the essential framework for development of a coupled gas/particle radiation model. The task is to obtain a practical mathematical solution based upon reasonable physical approximations to the spectral and spatial characteristics of the medium. In this section we review the available computational methods in order to identify promising approaches for the problem at hand.

A comprehensive discussion and development of the radiant transfer equation was given by Viskanta (1964). This equation may be written in the integro-differential form

$$\frac{dN_\lambda(\vec{s})}{ds} = -n\left(\sigma_\lambda^{(a)} + \sigma_\lambda^{(s)}\right)N_\lambda(\vec{s}) + n\sigma_\lambda^{(a)}N_\lambda^O(s)$$
$$+ \frac{n\sigma_\lambda^{(s)}}{4\pi}\int_{4\pi}P_\lambda(\vec{s}',\vec{s})N_\lambda(\vec{s}')d\Omega(\vec{s}') \tag{2-1}$$

where

$$N_\lambda(\vec{s}) = \text{spectral radiance at point } s \text{ in direction } \vec{s}$$

$$P_\lambda(\vec{s}',\vec{s}) = \text{phase function for scattering from } \vec{s}' \text{ to } \vec{s}$$

$$N_\lambda^O(s) = \text{blackbody spectral radiance at point } s$$

$$\sigma_\lambda^{(a)}, \sigma_\lambda^{(s)} = \text{cross sections for absorption and scattering}$$

$$n = \text{number density}$$

2-3

The terms on the right-hand side represent, respectively, the extinction (absorption plus scattering-out) and production (emission plus scattering-in) of radiation in the direction $\vec{s}$. The phase function is normalized such that

$$\frac{1}{4\pi}\int P_\lambda(\vec{s}',\vec{s})d\Omega(\vec{s}') = 1 \qquad (2\text{-}2)$$

The absorption and scattering probabilities $(n\sigma_\lambda^{(a)}$ and $n\sigma_\lambda^{(s)})$ and the volumetric emission $(n\sigma_\lambda^{(a)}N_\lambda^O)$ are defined to include implicitly the effect of multiple gas and particle species (i) and temperatures (T_i) through the relations

$$n\sigma_\lambda^{(a)} = \sum_i n_i\sigma_{\lambda i}^{(a)}$$

$$n\sigma_\lambda^{(s)} = \sum_i n_i\sigma_{\lambda i}^{(s)}$$

$$n\sigma_\lambda^{(a)}N_\lambda^O = \sum_i n_i\sigma_{\lambda i}^{(a)}N_{\lambda i}^O$$

$$n\sigma_\lambda^{(s)}P_\lambda = \sum_i n_i\sigma_{\lambda i}^{(s)}P_{\lambda i}$$

The effect of different particle sizes is also implicitly included.

The formal solution to the equation of transfer between points s_o and s may be written in the form

$$N_\lambda(\vec{s}) = N_\lambda(\vec{s}_o)T(s_o,s) + \int_{s_o}^{s} S_\lambda(s')\frac{dT(s',s)}{ds'}\,ds' \qquad (2\text{-}3)$$

where the source function (S_λ) at point s' in the direction $\vec{s}'$ and the transmittance (T_λ) from s' to s are given by

$$S_\lambda(\vec{s}') = (1-\omega_\lambda)N_\lambda^O + \frac{\omega_\lambda}{4\pi} \int_{4\pi} P_\lambda(\vec{s}'',\vec{s}')N_\lambda(\vec{s}'')d\Omega(\vec{s}'') \qquad (2-4)$$

$$T_\lambda(s',s) = \exp\left[\tau_\lambda(s')-\tau_\lambda(s)\right] \qquad (2-5)$$

and where the optical depth for extinction and the albedo for single scattering are defined as

$$\tau_\lambda(s) = \int_0^s n(\sigma_\lambda^{(a)}+\sigma_\lambda^{(s)})ds'$$

$$\omega_\lambda = \frac{\sigma_\lambda^{(s)}}{\sigma_\lambda^{(a)}+\sigma_\lambda^{(s)}} \qquad (2-6)$$

This formal solution is not explicit in that the local radiance is seen to depend on the radiance distribution throughout the medium which is not known at the outset. Explicit solutions can be obtained only for special cases as noted below.

In the absence of scattering $(\sigma_\lambda^{(s)} = 0)$, the formal solution to the equation of transfer assumes the explicit form

$$N_\lambda(\vec{s}) = N_\lambda(\vec{s}_0)T(s_0,s) + \int_{s_0}^s N_\lambda^O(s') \frac{dT_\lambda(s's)}{ds'} ds'$$

where the transmittance between points s' and s is given by

$$T(s',s) = \exp\left[-\int_{s'}^{s} n\sigma_{\lambda}^{(a)} ds''\right]$$

The evaluation of this equation on a monochromatic or spectrally-averaged basis is the end object of numerous existing line-by-line or band model radiation codes.

The finite difference form of the formal solution to the equation of transfer may be written directly from the preceding integral equations. Thus, the radiance at position k in direction i is given by

$$N_{ik} = N_{i,k-1}T_{k-1,k} + \tfrac{1}{2}(S_{ik} + S_{i,k-1})(1-T_{k-1,k}) \tag{2-7}$$

$$(i=1,2,\ldots,I; k=1,2,\ldots K)$$

where the source function is given by

$$S_{ik} = (1-\omega_k)N_k^o + \omega_k \sum_{j=1}^{I} P_{ji}N_{jk}$$

$$(i=1,2,\ldots,I; k=1,2,\ldots K)$$

and where the transmittance and phase integral are given by

$$T_{k-1,k} = \exp\left[(\sigma_{k-1}^{(a)} + \sigma_{k-1}^{(s)})n_{k-1}s_{k-1} - (\sigma_k^{(a)} + \sigma_k^{(s)})n_k s_k\right]$$

$$(k=1,2,\ldots,K)$$

$$P_{ji} = \frac{1}{4\pi} \int_{\delta\Omega_j} P(s_j,s_i)d\Omega(s_j)$$

$$(i,j=1,2,\ldots,I)$$

In these equations, the subscripts i,j,k denote the direction $\vec{s}, \vec{s}'$ and position s, respectively, and the subscript λ has been deleted for clarity. With appropriate boundary conditions on the radiance $N_{ik}(k=0,K; i=1,2...,I)$, which include the effects of any external sources, these equations constitute a closed set.

Solution techniques may be grouped into two fundamental classes: implicit or explicit. The implicit methods solve the coupled equations for N_{ik} and S_{ik} in an iterative manner starting from an assumed initial condition. A convenient procedure is to define an initial source function equal to the known thermal emission component $N_{ik}^{(1)}$ and corrected source function $S_{ik}^{(2)}$ directly. This procedure is then repeated to convergence according to the iteration formulae

$$N_{ik}^{(n)} = N_{i,k-1}^{(n)} T_{k-1,k} + \tfrac{1}{2}(S_{ik}^{(n)} + S_{i,k-1}^{(n)}) (1-T_{k-1,k})$$

$$S_{ik}^{(n+1)} = S_{ik}^{(n)} + \omega_k \sum_{j=1}^{I} P_{ji} N_{jk}^{(n)}$$

$$\begin{cases} i=1,2,\ldots,I \\ k=1,2,\ldots,K \\ n-1,2,\ldots,N \end{cases} \quad (2-8)$$

where the superscript (n) denotes the number of iterations or, equivalently, the order of scattering.

The explicit methods solve a single matrix equation for N_{ik} obtained by direct substitution of the equation for S_{ik}. After rearrangement of terms, the equation may be written in the form

$$\sum_{j=1}^{I} \left\{ N_{jk} (2\delta_{ji} T^{-1}_{k-1,k} - \omega_k P_{ji}) - N_{j,k-1} (2\delta_{ji} + \omega_{k-1} P_{ji}) \right\} =$$

$$(i=1,2,\ldots,I; k=1,2,\ldots,K)$$

$$(1-\omega_k) N_k^0 + (1-\omega_{k-1}) N_{k-1}^0 \tag{2-9}$$

where δ_{ji} is the Kronecker delta.

Implicit and explicit methods offer different relative advantages depending upon the optical and geometric properties of the medium. These properties control the number of iteration steps (implicit methods) or the size of the inversion matrix (explicit methods) required to obtain a given level of accuracy.

2.3 Review, Assessment and Selection of Multiple Scattering Formulation

2.3.1 Review and assessment. In the presence of scattering, explicit solutions can be obtained only for suitable approximations to the radiation flux or to the

phase function. Approximations to the radiation flux include the optically thin limit (in which the medium is not dense enough to absorb or scatter radiant energy from other elements in the volume) and the optically thick limit (in which the medium is so dense that radiant energy from other elements does not penetrate). These limits are of interest only as test cases for a more general model of arbitrary optical opacity. Approximations to the phase function include the discrete-ordinate method, the moment method, and the method of expansion in orthogonal functions (Krook, 1955) from which the well-known two-stream approximations of Schuster-Schwarzschild and Milne-Eddington (Viskanta, 1964) may be derived as special cases. In addition to these explicit methods, various implicit solution techniques have been developed. These techniques typically construct a convergent solution by incremental steps in space or time.

A summary of available multiple scattering solution techniques is given in Table 2-1. These methods can be roughly grouped into four general classes: superposition, transformation, convergence, and matrix. Each of these is discussed and developed in detail in the survey papers by Hansen and Travis (1974) and Irvine (1975). The identifications are necessarily somewhat arbitrary in that some interrelated techniques are included and some distinguishable subsets are excluded. Tables 2-2 and 2-3 list selected key investigations according to solution technique and chronology, respectively. The former was compiled

TABLE 2-1. METHODS OF SOLUTION FOR MULTIPLE SCATTERING

METHOD	DESCRIPTION	BENEFIT	DAMAGE
1. Superposition Methods			
Layer addition	Superposition of layers of known transmission and reflection	Wide application for planetary atmospheres	Non-emitting medium; plane-parallel slab
Invariant imbedding	Superposition of optically thin layers	Non-homogeneous atmospheres	Long computations
Synthesis	Superposition of volume elements	Generality	Inefficient for symmetric media
2. Transformation Methods			
X and Y functions	Mathematical transformation of variant imbedding	Single angle dependence	Rayleigh scattering
Spherical harmonics	Phase integral replaced by sum of spherical harmonics	General applicability	Large matrix
Eigenfunction	Phase integral replaced by sum of orthogonal eigenfunctions	Mathematically rigorous	Numerically prohibitive
3. Convergence Methods			
Iteration	Successive downward and upward integrations to convergence	Simple concept	Low opacity
Successive orders	Superposition of solutions for different orders of scattering	Simple concept	Low opacity; non-emitting medium
Monte Carlo	Individual photon histories traced and superposed	Simple concept; general applicability	Long computations
4. Matrix Methods			
Discrete ordinate	Phase integral replaced by finite sum	General applicability	Large matrix
Finite difference	Operates on differential equation	Computational experience	Large matrix unless symmetric
Finite element	Operates on integral equation	Reduces to two-stream limit	Large matrix unless symmetric

TABLE 2-2. REFERENCES FOR MULTIPLE SCATTERING METHODS

METHOD	REFERENCES
Layer Addition	van de Hulst, et al. (1963, 1968), Twomey, et al. (1966), Hansen (1969, 1971), Hovenier (1971), Lacis and Hansen (1974), Grant and Hunt (1969, 1971), Plass, et al. (1973), Preisendorfer (1965).
Successive Orders	van de Hulst and Irvine (1962), Irvine (1964, 1965), Uesugi and Irvine (1970), Poon and Ueno (1974), Dave (1964), Hovenier (1971), Chou (1978).
Invariant Imbedding	Uesugi and Irvine (1970), Bellman, et al. (1960, 1963, 1967, 1969), Wing (1962).
Iteration	Herman, et al. (1963, 1965, 1970), Dave, et al. (1970), Crosbie and Linsenbardt (1975).
X and Y Functions	van de Hulst (1970), Sobolev (1972, 1974), Carlstedt and Mullikin (1966), Pahor and Kuscer (1966), Busbridge (1960, 1967).
Discrete Ordinate	Chandrasekhar (1950), Jefferies (1955), Chu and Churchill (1955), Lenoble (1956), Chin and Churchill (1965), Samuelson (1969), Liou (1973, 1974), Weinman and Guetter (1972), Whitney (1972, 1974), Kofink (1967), Love and Grosh (1965).
Spherical Harmonics	Canosa and Penafiel (1973), Davison (1958), Case and Zweifel (1967), Deuze, et al. (1973), Dave, et al. (1974).
Eigenfunctions	Case and Zweifel (1967), Kuscer and McCormick (1973, 1974), Kaper, et al. (1970), Mika (1961).
Monte Carlo	Plass and Kattawar (1968, 1971), Danielson, et al (1968, 1969), Sanford and Pauls (1973), Collins, et al. (1965, 1972), Van Blerkom, et al. (1971, 1974), McKee and Cox (1974), Kattawar, et al. (1971, 1973), Marchuk and Mikhailov (1967).
Diffusion	Heasley (1977), Barkstrom and Arduini (1978), Laung (1975, 1976)
Finite Difference	Barkstrom (1976).

TABLE 2-3. CHRONOLOGY OF MULTIPLE SCATTERING METHODS

YEAR	REFERENCE	PHYSICAL SITUATION	METHOD OF ANALYSIS
1955	Jefferies	Point and infinite line sources in a semi-infinite medium	Diffusion approximation
1955	Jefferies	A strip of collimated radiation incident on a semi-infinite medium	Discrete ordinates and Fourier transform
1955	Chu and Churchill	Point source outside an anisotropically scattering finite layer	Six-flux approximation
1956	Giovanelli	An infinite line source on the surface or within a semi-infinite medium and a thick finite layer	Approach of Jefferies
1958	Chandrasekhar	An infinitely narrow collimated beam incident on a semi-infinite medium	Invariance principles
1963	Bellman, Kalaba, and Ueno	An infinitely narrow collimated beam incident on a finite layer with properties varying with depth	Invariant imbedding
1963	Bellman, Kalaba, and Ueno	Collimated radiation incident on an inhomogeneous anisotropically scattering finite layer	Invariant imbedding
1964	Smith	A uniform strip of collimated radiation incident on a semi-infinite medium	Assumed cosine-varying incident radiation to reduce the two-dimensional integral equation for the source function to a one-dimensional form
1964	Malkevich, Monin, and Rozenberg	Collimated radiation incident on a finite layer with nonuniform reflection from lower surface	Horizontal variation of downward radiation neglected
1965	Chin and Churchill	An arbitrary, cylindrical source in an anisotropically scattering finite slab	Six-flux approximation
1966	Dolin	Narrow collimated beam incident on a semi-infinite anisotropically scattering medium	Small angle transport equation used for unscattered radiation, diffusion equation used for scattered radiation
1967	Weinman and Swarztrauber	Collimated radiation incident on a nonabsorbing finite layer with horizontally nonuniform scattering coefficient	Giovanelli's approximation used to solve transport equation
1967	Smith and Hunt	A uniform strip of collimated radiation incident on a semi-finite layer	Same as Smith 1964
1967	Hunt	Collimated radiation incident normally on an anisotropically scattering finite medium	Expression of scattering function as series of Legendre polynomials
1967	Bobco	An isothermal semi-infinite slab	Diffusion equation solved by iterative technique
1967	Drobyshevich	Collimated radiation incident on an anisotropically scattering finite layer with nonuniform reflection from lower surface	Horizontal variation of downward radiation neglected
1968	Romanova	An infinitely narrow collimated beam normally incident on a semi-infinite anisotropically scattering medium	Three-dimensional moments used to solve the transport equation for large depths
1968	Romanova	An infinitely narrow collimated beam normally incident on an anisotropically scattering finite layer	Small angle approximation to the transport equation solved using spatial moments

TABLE 2-3. (CONTINUED)

YEAR	REFERENCE	PHYSICAL SITUATION	METHOD OF ANALYSIS
1968	Funk	Collimated point source normally incident on an anisotropically scattering finite layer	Monte Carlo technique
1968	Hunt	Collimated Bessel function varying radiation incident on a finite layer	Integral equation for the source function formulated using Green's function
1969	Stockham and Love	An isothermal finite cylindrical medium; both isotropic and anisotropic scattering	Monte Carlo technique
1969	Hunt	Collimated radiation normally incident on a finite layer	Integral equation for source function transformed into singular equation for the resolvent kernel using properties of a Green's function
1969	Bravo-Zhivotovskiy, Dolin, Luchinin, and Savel'yev	Narrow collimated beam normally incident on a semi-infinite anisotropically scattering medium	Uses solution to transport equation found in Dolin 1966
1969	Golubitskiy and Tantoshev	An infinitely narrow collimated beam at the center of an anisotropically scattering spherical medium	Monte Carlo technique
1970	Love and Turner	An isothermal semi-infinite slab	Monte Carlo technique
1970	Scofield and Love	A strip of diffuse radiation incident on an emitting semi-infinite medium; both isotropic and anisotropic scattering	Monte Carlo technique
1971	Rybicki	An infinitely narrow collimated beam incident on a finite layer and semi-infinite medium	Fourier transform and invariance techniques
1971	Romanova	An infinitely narrow collimated beam normally incident on a non-absorbing finite layer	Three-dimensional invariance principles used to obtain equations for spatial moments of intensity
1971	Romanova	An infinitely narrow collimated beam normally incident on an anisotropically scattering finite layer	Spatial moments used to solve small angle approximation to the transport equation
1971	Kochetkov	An infinitely narrow collimated beam normally incident on an anisotropically scattering finite layer	Method of spherical harmonics
1972	Dushmakova, Zege, and Katsev	Diffuse and unidirectional sources inside an anisotropically scattering finite layer and semi-infinite medium	Hankel transformation used to solve diffusion equation
1973	Romanova	An infinitely narrow collimated beam normally incident on a finite layer with weak absorption	Intensity represented by transverse moments and invariance principles used
1973	Funk	A narrow collimated beam and noncollimated source in an infinite anisotropically scattering medium	Monte Carlo technique
1973	Gordon and Knittel	An infinitely narrow collimated beam normally incident on an anisotropically scattering finite layer	Iterative ray tracing, no return backscattering and small angle approximations used
1974	Crosbie and Koewing	A step and finite strip of collimated and diffuse radiation incident on a finite layer	Assumption of cosine varying incident radiation reduces problem to one-dimensional problem; Ambarzumian's method
1974	Beckett, Foster, Hutson and Moss	A collimated cylindrical beam normally incident on a finite layer	Hunt's integral equations solved by iteration

2-13

from previous review papers together with our own review;
the latter was taken directly from Crosbie and Linsenbardt
(1976). Neither list is comprehensive, but both serve to
illustrate the depth and scope of previous work. Most of
these studies applied to non-emitting plane-parallel atmospheres.
Only a limited number of the studies included the effects of
thermal emission, inhomogeneous media, non-isotropic scattering,
and non-planar geometry which are important in the present
application. None of the studies treated all these effects
simultaneously. Despite these deficiencies, this previous work
provides a firm base for the selection and development of a
multiple scattering model for two-phase plumes.

Existing rocket plume radiation codes which treat particle
radiation were also reviewed and are presented in Table 2.4.
The early codes of Fontenot (1965), Gulrajani (1964), Hunt (1966)
and the Aeronutronic group (Carson, 1965) were all developed to
predict base heating. The more recent plume codes of Wilson
(1973), Rieger (1974), Vanderbilt and Slack (1976), and the ARAP
group (Fishburne, 1977) were developed to predict plume IR signatures.
These codes approximate particle radiation effects by either of
two methods: Pseudo-gas or one-dimensional beam. The pseudo-gas
approximation includes particle emission/absorption effects but neglects

TABLE 2-4. EXISTING ROCKET PLUME RADIATION CODES INCLUDING PARTICLES

PLUME CODES	METHOD	COMMENTS
Fontenot (1965)	Inverse wavelength method	Simplistic approach; single particle size neglects scattering. Estimates base-heating for constant radial properties.
Gulrajani (1964) Hunt (1966)	Neutron-scattering analogy method	Based on Morizumi and Carpenters (64) analysis. Five particle sizes. Includes 1-D multiple scattering. Neglects anisotropic scattering effects. Assumes $Q_t \to 2$. Base-heating estimates.
Aeronutronic (Carlson, 1965)	One-dimensional beam approximation	Plume codes to analyze Saturn ullage retro and strap-on exhaust plumes. 1-D anisotropic scattering approximation.
Wilson and Hahn (1973)	One-dimensional beam approximation	Uncoupled gas and particles. Adds separately computed particle radiation and gas radiation. Narrow inband resolution. Treats 5 particle sizes.
Rieger (1974)	Pseudo-gas approximation	Computes coupled particle and gas emission and absorption.
Vanderbilt & Slack (1976)	One-dimensional beam approximation	Couples multiple scattering and gaseous emission/absorption along beams. Spectral resolution 5 cm^{-1}. Treats 5 particle sizes. Treats gases as non-scattering particles yet retains correct solution of radiative transfer equation for gases alone and particles alone. Spectral and inband output coupled to LOWTRAN codes. Dave code for Q_s, Q_a
ROCRD Code (ARAP)	Pseudo-gas approximation	Includes particle emission, but neglects scattering. Assumes Beer's law.

scattering. The one-dimensional-beam approximation includes particle scattering effects along the beam but neglects scattering into the beam from other directions. Of the two methods, the one-dimensional beam provides a better physical description of particle radiation effects with no appreciable penalty in computational complexity. Wilson used the one-dimensional beam approximation to compute the particulate radiation field in an uncoupled manner for subsequent addition to the gaseous radiation field; the validity of this procedure is restricted to low optical depths. Vanderbilt and Slack used the one-dimensional beam approximation to compute the coupled particulate and gaseous radiation fields, thereby allowing the gas to absorb the particulate continuum and the particles to scatter and absorb the gaseous radiation. The code developed by Vanderbilt and Slack is the best of the existing codes for predicting spectral IR signatures from missile plumes. However, the lack of coupling between adjacent 1-D beams means that it does not meet the SIRRM code requirements, in general.

One dimensional beam methods have received extensive application and limited verification in the area of radiative heat transfer but only limited application and no verification in the area of radiative signatures. This distinction is important because of a fundamental difference between the two phenomena. On the one hand, the radiative heat transfer to an adjacent point is the sum of contributions from non-parallel beams. On the other hand, the radiative signature to a remote point is the sum of contributions from parallel beams. The

latter effect is much more sensitive to errors in the directional properties of the radiation field. Thus, the SIRRM code must include a three-dimensional scattering model in order to achieve the required directional accuracies.

2.3.2 Selection and justification. As noted previously, the SIRRM scattering model for two-phase plumes must include the following key physical effects: thermal emission, inhomogeneous media, non-isotropic scattering, and non-planar geometry. In addition, the SIRRM scattering model must possess the following computational attributes: accuracy, efficiency, and generality. These general attributes have rather specific meanings for the present application as noted below:

Accuracy The chosen technique should incorporate sufficient spatial resolution to yield an accurate mathematical solution. The technique should demonstrate adequate agreement with the predictions of alternative methods for suitable test cases.

Generality The chosen technique should incorporate sufficient spatial dimensions to represent the real physical problem. The technique should treat all ranges and variations of optical depth, scattering albedo, and phase function such that no limit is imposed on the nature of gas or particle properties, plume properties, or observation geometry.

Efficiency   The chosen technique should yield computed

results in machine times which are comparable to current

gaseous emission codes for an equivalent number of aspect

angles.   Approximate techniques which incorporate physically

acceptable assumptions should be evaluated in order to

determine the most efficient technique for different classes

of problems.

The available methods were screened according to these criteria.

The dual requirement for engineering efficiency and scien-

tific accuracy, together with the need for computational gen-

erality, and flexibiltiy, led to the selection of straight-

forward, finite difference procedures of variable spatial and

angular resolution applied to locally cylindrical plume geometries.

Two basic approaches (herein identified as "6-flux" and "N-flux")

were distinguished and various alternatives were developed within

each classification.   The semantic distinction refers to the

associated subdivision of angular space (6 orthogonal coordinates

versus N non-orthogonal coordinates in azimuth and elevation).

However, the fundamental distinction lies with the generality

of the N-flux model versus the computational simplicity of the

6-flux model.

Within the 6-flux model class, two independent sub-class

models were developed.   The first model employs suitable approxi-

mations for the axial and tangential radiances in order to

reduce the solution to a one-dimensional radial integration
similar to existing two-stream models (Vanderbilt-Slack, 1976).
The second model employs a transformation of the multiple-
scattering source function in order to reduce the solution to
a coupled set of radial, tangential, and axial integrations, each
of which is functionally similar to existing two-stream models.
The two six-flux models are described and compared in Section
2.4.

The N-flux model class includes a generalized set of
optional finite-element grid geometries including independent
specification of the angular resolution in the azimuth and
elevation planes. The model solves the coupled three-dimensional
equations of transport using a generalized matrix network
to describe the radiance distribution and source function at each
grid point. The model can be exercised as either an engineering
or scientific tool by simple variations in the spatial and angular
grid network to achieve low or high resolution. Analytical
details are presented in Section 2.5.

Each of the models was exercised parametrically over the
full physical range to illustrate the effect of optical depth,
scattering albedo, and phase function on the local and integrated
target signature characteristics. These calculations provided
independent tests of the physical credibility and computational
efficiency of the separate models as well as comparative tests
of the accuracy and self-consistency of the composite model set.

Additional verification was accomplished by performing independent calculations with the NASA plane-parallel slab code (Barkstrom, 1976) modified to include self-emission and with the Grumman Monte Carlo code. Results of these calculations are summarized in Section 2.6.

2.4   Six-Flux Engineering Approaches

The basis for the engineering approaches developed under Task IA is the approximation of the multiple-scattering source function by a six-element orthogonal angular quadrature. In this approximation, the general differential equation of transport

$$\frac{dN(\tau,\Omega)}{d\tau} = -N(\tau,\Omega) + \left|1-\omega(\tau)\right| N^O(\tau) + \frac{\omega(\tau)}{4\pi} \int_{4\pi} P(\tau,\Omega,\Omega')N(\tau,\Omega')d\Omega' \quad (2\text{-}10)$$

is written for each orthogonal direction (i = 1,2,3) in the specific form

$$\pm \frac{dN_i^{\pm}}{d\tau_i} = -N_i^{\pm} + (1-\omega)N^O + \omega\left[fN_i^{\pm} + bN_i^{\mp} + s\sum_{i'\neq i}(N_{i'}^{+} + N_{i'}^{-})\right] \quad (2\text{-}11)$$

where the terms on the right-hand side represent the respective contributions of extinction, emission, and multiple scattering to the radiance gradient and where the terms f,b,s represent the forward, backward, and sideward components of the phase function (f+b+4s=1). This quadrature provides the minimum angular

resolution necessary to account for three-dimensional multiple-scattering effects. For comparison to previous approaches, the standard two-element, one-dimensional approximation is obtained as a special case (s=0).

The orthogonal coordinates are chosen to coincide with the natural cylindrical coordinates (r, θ, z) of the axisymmetric plume. Figure 2-1 illustrates the grid network formed by the intersections of these coordinates with the boundaries of the finite elements (radial and axial). The six-flux equations are solved as a coupled set along these mutually-perpendicular integration paths. Radiances for oblique lines-of-sight are computed in a subsequent step based upon the known six-flux solution.

Within the six-flux model class, two different levels of engineering approximation were employed. The first method yields an approximate explicit solution based upon elimination of the tangential (θ) equations of transport in favor of simple closure relations. The second method yields an exact implicit solution based upon iteration or inversion of the fully-coupled multi-dimensional equation set. Both methods were originally developed for infinite cylindrical geometries (negligible axial gradients). The second method was subsequently extended to finite cylindrical geometries in order to assess the influence of plume axial gradients on the radiance at side aspect. The following paragraphs provide analytical details.
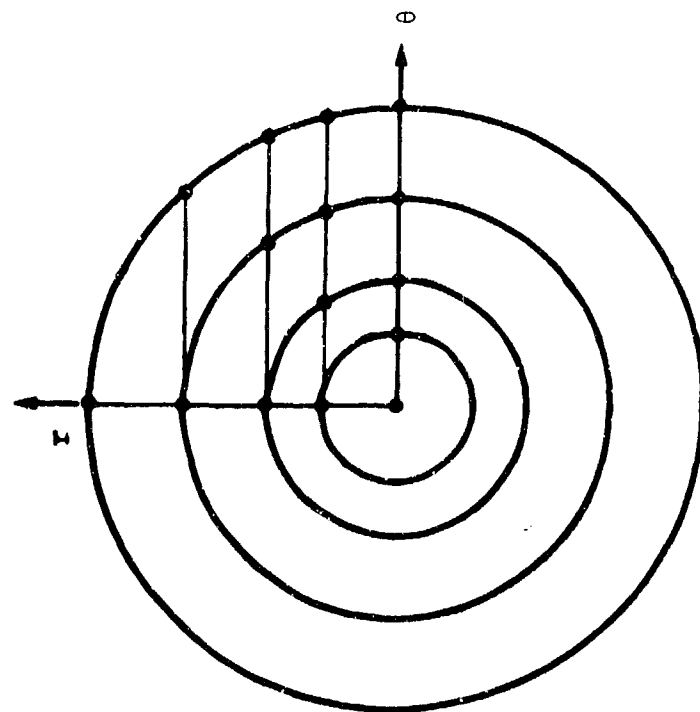
Side View

End View
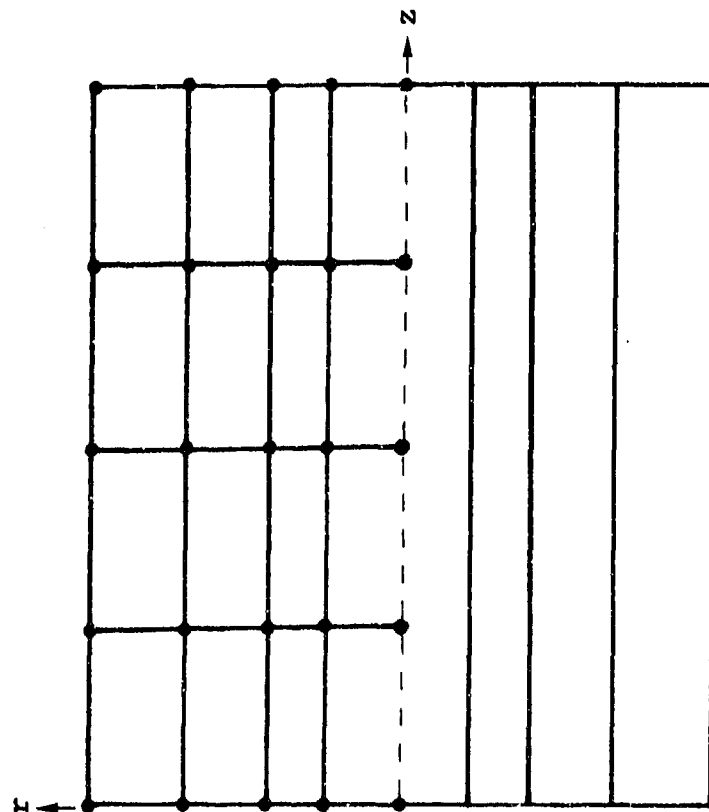
Figure 2-1.   Six-Flux Model Coordinate System.

2.4.1 Method I.   This method is based upon a transformation
of the three-dimensional equations of radiative transport to equi-
valent one-dimensional form for infinite planar or cylindrical media.
The resulting equation is integrated along a piecewise-uniform
path perpendicular to the surface to yield an explicit solution
for the normal and tangential radiances throughout the medium.
Radiances at intermediate angles are determined by analytical
interpolation.   No restriction is placed upon the range of
physical properties considered (e.g. optical depth, scattering
albedo, phase function) or upon the variation of those properties
within the medium.

The ability to treat planar and cylindrical geometries in a
self-consistent manner provides an important connection between
the available literature (mostly planar) and the plume problem
(nearly cylindrical).   As a result of this connection, the utility
of existing plane parallel codes (e.g., Barkstrom, 1976) for
defining baseline parametric trends is greatly enhanced.   In
addition, solutions for planar media which are infinite in one
or two directions (i.e., ribbon or slab, respectively) provide
convenient bounds on the emitted radiation from equivalent
cylindrical media.

In the rectangular r, θ, z coordinate system of Figure 2-1, the
equation of transfer reduces to the six simultaneous equations

2-23

$$\pm \frac{dN_r^{\pm}}{d\tau_r} = -N_r^{\pm} + (1-\omega)N^O + \omega\left[fN_r^{\pm} + bN_r^{\mp} + s(N_\theta^+ + N_\theta^- + N_z^+ + N_z^-)\right]$$

$$\pm \frac{dN_\theta^{\pm}}{d\tau_\theta} \approx -N_\theta^{\pm} + (1-\omega)N^O + \omega\left[fN_\theta^{\pm} + bN_\theta^{\mp} + s(N_r^+ + N_r^- + N_z^+ + N_z^-)\right] \Biggr\} \quad (2\text{-}12)$$

$$\pm \frac{dN_z^{\pm}}{d\tau_z} = -N_z^{\pm} + (1-\omega)N^O + \omega\left[fN_z^{\pm} + bN_z^{\mp} + s(N_r^+ + N_r^- + N_\theta^+ + N_\theta^-)\right]$$

These six equations are further reduced to two (±r) by means of suitable analytical approximations for the perpendicular radiances (±θ,±z). The z-equation is simplified through the assumption of negligible axial gradients

$$\left|\frac{dN_z^{\pm}}{d\tau_z}\right| \ll N_z^{\pm}$$

which reduces the equation to simple algebraic form. The θ-equation is eliminated through the assumption of approximate proportionality factors

$$N_\theta^{\pm} \approx \Phi_p N_z^{\pm} \qquad \text{(plane)}$$

$$N_\theta^{\pm} \approx \Phi_c \tfrac{1}{2}(N_r^+ + N_r^-) \quad \text{(cylinder)}$$

which are piecewise-constant over a radial integration step. The range $0 < \Phi_p < 1$ defines the limits of thin and thick optical paths in the θ-direction. In general, the factor Φ is approximated

by the corresponding radiance ratio for a non-scattering medium. For a uniform medium, this ratio is given simply by the emissivity ratio

$$\Phi_p = 1 - \exp(-\tau_\theta)$$

$$\Phi_c = \left[1 - \exp(-\tau_\theta)\right] / \left[1 - \exp(-\tau)\right]$$

where τ is the total optical depth for a cylinder of diameter 2R and τ_θ is the half optical depth measured perpendicular to the line-of-sight. For a uniform cylinder $\tau_\theta = \tau[1 - (r/R)^2]^{\frac{1}{2}}$. Substitution of these approximations into the axial equation of transport yields the explicit formulae

$$N_z^{\pm} = \left[(1-\omega)N^O + \omega s(N_r^+ + N_r^-)\right]\left[1 - \omega(f + b + 2\Phi_p s)\right]^{-1} \quad \text{(planar)}$$

$$N_z^{\pm} = \left[(1-\omega)N^O + \omega s(1 + \Phi_c)(N_r^+ + N_r^-)\right]\left[1 - \omega(f + b)\right]^{-1} \quad \text{(cylindrical)}$$

$$\left.\right\} (2\text{-}13)$$

With these approximations, the six-flux radial equation of transport may be written in the functional form of the two-flux equation with modified coefficients. That is,

$$\pm \frac{dN_r^{\pm}}{d\tau_r} = -\alpha N_r^{\pm} + \beta N_r^{\mp} + \gamma N^O \qquad (2\text{-}14)$$

where the piecewise-constant coefficients are given by

planar	cylindrical

$$\alpha = 1-\omega(f+s\chi)$$ $$\alpha = 1-\omega\{f+s[\chi+\Phi_c(1+\chi)]\}$$

$$\beta = \omega(b+s\chi)$$ $$\beta = \omega\{b+s[\chi+\Phi_c(1+\chi)]\}$$

$$\gamma = (1+\chi)(1-\omega)$$ $$\gamma = (1+\chi)(1-\omega)$$

$$\chi \equiv 2s\omega(1+\Phi_p)[1-\omega(f+b+2\Phi_p s)]^{-1}$$ $$\chi = 2s\omega[1-\omega(f+b)]^{-1}$$

Integration over the uniform region from station (k-1) to k yields explicit expressions for the outward and inward radiance components at the outer and inner surfaces, respectively.

$$
\begin{aligned}
N_k^+ &= \rho_k N_k^- + t_k N_{k-1}^+ + \varepsilon_k N_k^O \\[2mm]
N_{k-1}^- &= t_k N_k^- + \rho_k N_{k-1}^+ + \varepsilon_k N_k^O
\end{aligned}
\Bigg\} \qquad (2\text{-}15)
$$

where the subscript r has been deleted for clarity.
These equations contain the boundary conditions (N_k^- and N_{k-1}^+), the local source function (N^O), and the local transport coefficients (reflectivity, transmissivity, and emissivity) defined by the relations

$$\rho = \frac{1-\xi^2}{1-\xi^2\eta^2}\,\eta \qquad\qquad \xi = \frac{\beta}{\alpha+\lambda}$$

$$t = \frac{1-\eta^2}{1-\xi^2\eta^2}\,\xi \qquad\qquad \eta = \exp\left[-\lambda(\tau_k-\tau_{k-1})\right]$$

$$\varepsilon = \frac{\gamma}{\alpha-\beta}(1-t-\rho) \qquad\qquad \lambda = \left[(\alpha+\beta)(\alpha-\beta)\right]^{\frac{1}{2}}$$

The axial radiances at the outer and inner surfaces then follow directly.

The formulation for a uniform planar medium is complete at this point. For a non-uniform or cylindrical medium, the formulation is completed by superposition of elemental solutions for K piecewise-uniform subregions (k=1,2,...,K) subject to the overall boundary conditions

$$N_K^- = 0 \qquad \text{(no external sources)}$$

$$N_o^+ = N_o^- \qquad \text{(axial symmetry)}$$

The radiance emerging from the K-th (outer) element is determined from Eq. 2-15 by successive Gaussian elimination beginning at the center (k = 0). The general recursion relation (developed by induction) is given by

$$N_k^+ = A_k N_k^- + B_k$$

where

$$A_k = \rho_k + t_k C_k A_{k-1} \qquad ; \qquad A_o = 1$$

$$B_k = D_k N_k^o + C_k B_{k-1} \qquad ; \qquad B_o = 0$$

$$C_k = t_k (1 - \rho_k A_{k-1})^{-1}$$

$$D_k = \epsilon_k (1 + C_k A_{k-1})$$

The surface radiance ($N_K^+ = B_K$) is determined explicitly from the sequential summation.

The preceding analysis yields the normal and tangential radiance components for planar and cylindrical media. Between these limits, the variation of radiance with elevation angle (ϕ) or azimuth angle (θ) (standard spherical coordinates) must be determined by a subsequent calculation. The following paragraphs describe a simple approximate procedure based on analytical interpolation. An alternative exact procedure based on the known six-flux source function distribution is described under Method II.

The approximate interpolation formulae are based on weighted sums of the local-to-normal and local-to-tangential radiance ratios for a non-scattering medium. From Figure 2-2

$$N(\theta,\phi) \quad \approx \quad \left[\frac{N(\theta,\phi)}{N(\pi/2,\pi/2)}\right]_{\omega=0} N(\pi/2,\pi/2)\sin^2\phi$$

$$+ \left[\frac{N(\theta,\phi)}{N(\pi/2,0)}\right]_{\omega=0} N(\pi/2,0)\cos^2\phi$$

where $N(\pi/2,\pi/2)$ and $N(\pi/2,0)$ are the normal and tangential radiances predicted by the six-flux model. The θ and ϕ variations are conveniently separated by rewriting $N(\theta,\phi)$ as the product

2-28
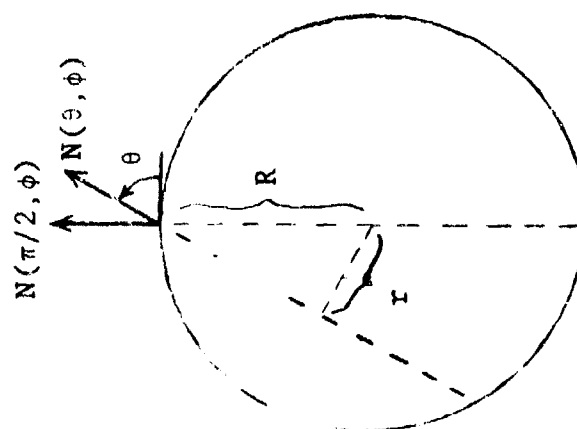
SIDE VIEW
(Elevation Plane)

END VIEW
(Azimuth Plane)
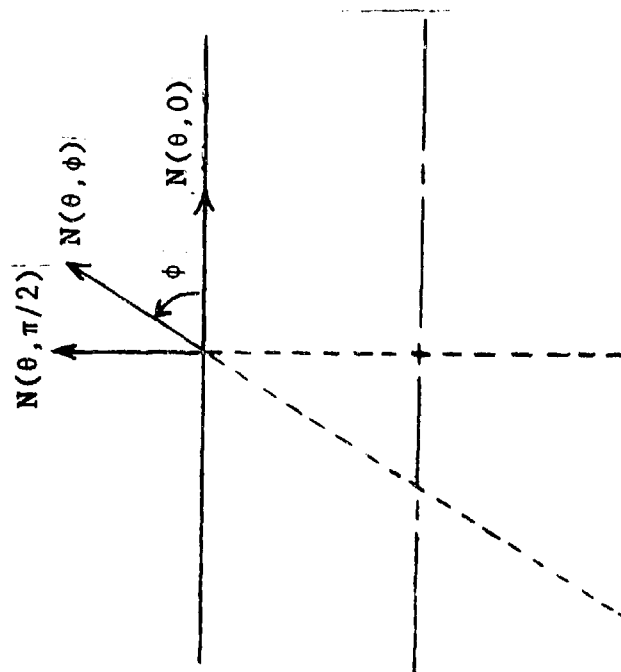
Figure 2-2. Estimation of Three-Dimensional Radiance Distribution from Computed Radiances at Normal and Tangent Aspect.

$$N(\theta,\phi) = \left[\frac{N(\theta,\phi)}{(N(\pi/2,\phi)}\right]_{\omega=0} \cdot \left\{\left[\frac{N(\pi/2,\phi)}{N(\pi/2,\pi/2)}\right]_{\omega=0} N(\pi/2,\pi/2)\sin^2\phi\right.$$

$$\left. +\left[\frac{N(\pi/2,\phi)}{N(\pi/2,0)}\right]_{\omega=0} N(\pi/2,0)\cos^2\phi\right\}$$

This separation facilitates the integration over θ to obtain the local station radiation.

$$J'(\phi) = 2\sin\phi\int_0^r N(\theta,\phi)dr$$

$$= 2R\sin\phi\int_0^\theta N(\theta,\phi)\cos\theta d\theta$$

$$= 2R\sin\phi N(\pi/2,\phi)\int_0^\theta \left[\frac{N(\theta,\phi)}{N(\pi/2,\phi)}\right]_{\omega=0}\cos\theta d\theta$$

For uniform media the radiances for $\omega=0$ are simply proportional to the corresponding emissivities; i.e.,

$$N(\theta,\phi) \sim \epsilon\ (\tau\sin\theta/\sin\phi)$$

where τ is the optical depth based on the cylinder diameter. In this case, the radiance is given by the simplified formula

$$N(\theta,\phi) = \epsilon(\tau\sin\theta/\sin\phi)\left|N(\pi/2,\pi/2)\sin^2\theta/\epsilon(\tau)\right.$$

$$\left. + N(\pi/2,0)\cos^2\phi\right|$$

and the station radiation is well-approximated by the empirical formula (see Figure 2-3)

$$J'(\phi) = 2R\sin\phi\varepsilon(\tau/\sin\phi)[N(\pi/2,\pi/2)\sin^2\phi/\varepsilon(\tau)+N(\pi/2,0)\cos^2\phi] \cdot$$

$$\varepsilon(.546\tau/\sin\phi)/\varepsilon(.695\tau/\sin\phi)$$

The non-dimensional ratio $J'(\phi)/2R\sin\phi N(\pi/2,\phi)$ is observed to approach $\pi/4$ or 1 in the optically thin or thick limits, respectively. These interpolation formulae suffice to define the entire radiation field at a given axial station in terms of the computed normal and tangential radiances.
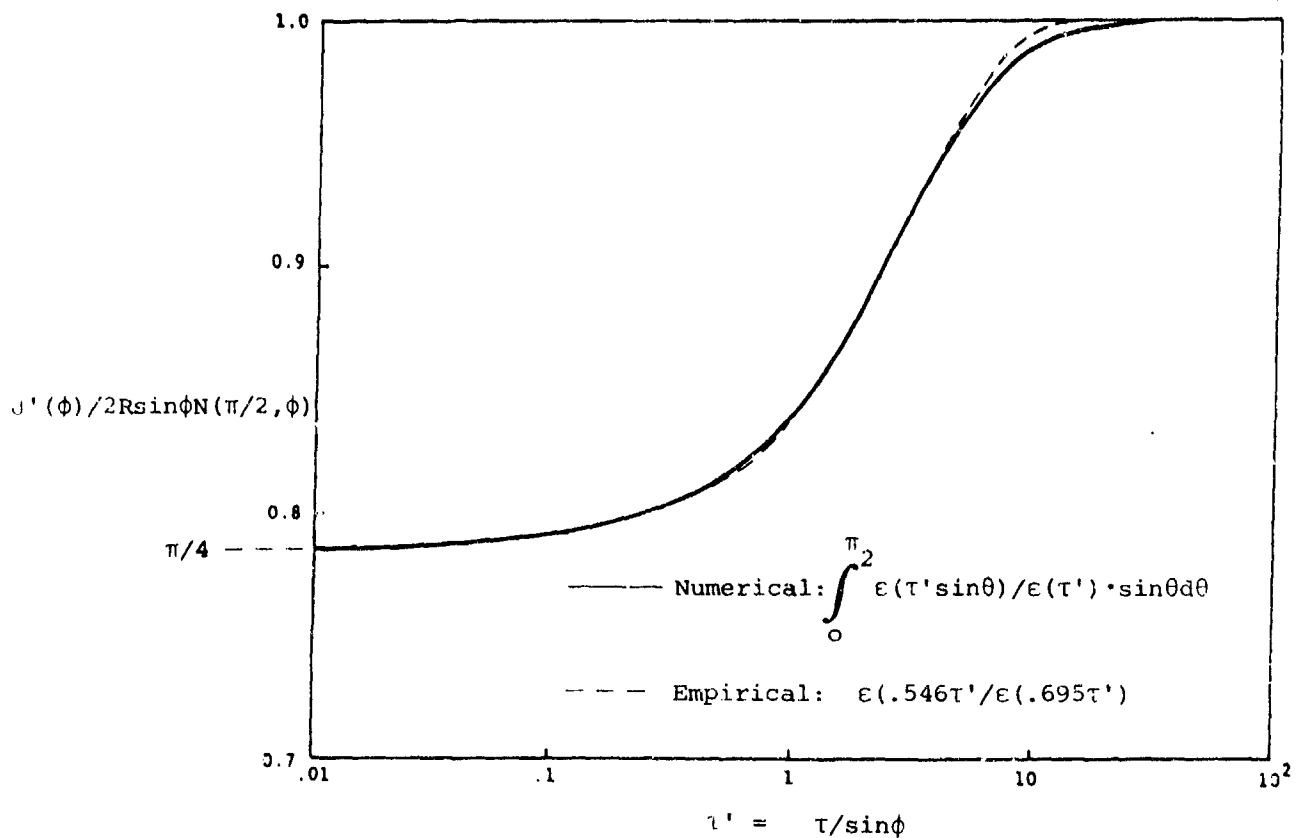
Figure 2-3. Estimation of Station Radiation for Uniform Cylinder from Computer Centerline Radiance.

2.4.2 Method II.   This method is based upon a transformation
of the three-dimensional equations of transport tc equivalent iso-
tropic form for infinite and finite cylindrical media. The resulting
equations are integrated along and perpendicular to the radial direc-
tion to yield an implicit solution for the isotropic (scalar) source
function distribution. Numerical results are obtained by iteration
using the method of successive scatterings. Solutions for arbitrary
aspect are then computed directly in terms of the known source func-
tion by means of a two-stream integration along the observer line-
of-sight. As for Method I, no restriction is placed upon the range
or variation of physical properties within the medium.

The general six-flux equation of transport (see Eq. 2-11)

$$\pm \frac{dN_i^{\pm}}{d\tau_i} = -N_i^{\pm} + (1-\omega)N^O + \omega\left[fN_i^{\pm} + bN_i^{\mp} + s\sum_{i'\neq i}(N_{i'}^{+} + N_{i'}^{-})\right] \quad (i=1,2,3)$$

is transformed by simple rearrangement of terms to equivalent
isotropic form

$$\pm \frac{dN_i^{\pm}}{d\tau_i} = -\alpha N_i^{+} + \beta N_i^{\mp} + \gamma(N^O+N') \quad (i=1,2,3) \tag{2-16}$$

where the piecewise-constant coefficients are given by

$$\alpha = 1-\omega(f-s)$$

$$\beta = \omega(b-s)$$

$$\gamma = (1-\omega)$$

and where the source function for multiple scattering is given by

2-32

$$N' = \frac{\omega s}{(1-\omega)} \sum_{i'=1}^{3} (N_i^+ + N_i^-)$$

The key feature of the transformed equation set is that the source function now contains only the side-scattering component of the phase function such that N' is a scalar quantity. This important simplification is obtained for any arbitrary phase function which can be approximated by a six-angle orthogonal quadrature.

For a known source function N' (as from a previous iteration) the transformed equation of transport is functionally equivalent to Method I and can be integrated as before to yield

$$\left. \begin{aligned} N_{ik}^+ &= \rho_{ik} N_{ik}^- + t_{ik} N_{ik-1}^+ + \varepsilon_{ik}(N^O{}_k + N'{}_k) \\ N_{ik-1}^- &= t_{ik} N_{ik}^- + \rho_{ik} N_{ik-1}^+ + \varepsilon_{ik}(N^O{}_k + N'{}_k) \end{aligned} \right\} \quad \begin{aligned} (i=1,2,3) \end{aligned} \quad (2\text{-}17)$$

where ρ_{ik}, t_{ik}, ε_{ik} are the reflectivity, transmissivity, and emissivity of the element k in the direction i and $N_{ik}^{\pm}$, $N_{ik-1}^{\pm}$ are the surface radiances. The coefficients ρ, t, ε are evaluated as before (see Method I) in terms of the coefficients α, β, γ, where the latter have new definitions as given above. The requisite geometrical relations are given in Section 2.5. For an array of K elements (k=1, 2,...K), the boundary conditions are

$$N_{io}^+ = N_{io}^- \quad \text{(axial symmetry)}$$
$$\quad (i=1,2,3)$$
$$N_{iK}^- = 0 \quad \text{(no external sources)}$$

In the direction of integration, these equations form a system of 2K equations for the 2K radiances $N_k^{\pm}$ defined over

2-33

a K-point linear mesh. An additional 2K equations of similar form are required for each perpendicular direction in order to define the source function at each grid point k. For each path, the transport equation yields a one-dimensional solution matrix which is a diagonal sub-block of the full three-dimensional solution matrix. The individual paths are coupled through the scalar source function at intersecting points such that the complete ensemble of paths is required to obtain closure. The complete matrix is solved by iteration using the single-scattering solution (multiple-scattering source function equal to zero) as the initial guess. For the cases investigated to date (see Section 2.6), two to eight iterations (depending on the product $\omega \cdot \tau$) were sufficient to achieve source function convergence within two percent.

The importance of the isotropic source function transformation can be appreciated by reference to the tangential (θ) integration paths in Figure 2-1. Except for the s-axis, the intersections of these paths with the cylindrical shells are observed to occur at oblique angles which do not coincide with the six-angle quadrature of the phase function. This situation presents no difficulty when the source function is isotropic. However, a non-uniform angular quadrature would be required to represent non-isotropic scattering into the line-of-sight. Such an approach is somewhat more complex than the present method, but offers the potential for greater accuracy through higher resolution. This capability is provided by the multiple-flux model described in the following section.

2.5 Multiple-Flux Exact Approach

The basis for the exact approach developed under Task IA is the approximation of the multiple-scattering source function by an angular quadrature of arbitrary resolution. The accuracy of the predicted radiation field increases as the resolution of the angular quadrature increases. Exact solutions are obtained by increasing the resolution in successive calculations until convergence is achieved.

The arbitrary angular resolution of the multiple-flux (henceforth called "N-flux") model affords considerable flexibility in the analysis of multiple-scattering problems. The resolution in the elevation and azimuth planes is independently specified so that individual optima can be established. An important feature of the formulation is the introduction of non-uniform azimuthal resolution which increases as the radius increases in order to achieve uniform accuracy from the isotropic center to the anisotropic edge. An alternative formulation based on uniform azimuthal resolution was considered early in the model development effort, but was abandoned due to its greater complexity and lesser accuracy compared to the present approach.

Figure 2-4 shows end-view and side-view projections of representative lines-of-sight through an assembly of infinite cylindrical shells in which the source function for multiple scattering is assumed constant. In the present development,

2-35

ELEVATION PLANE
(Illustrated for x = 0)

AZIMUTH PLANE
(Projection for Arbitrary φ)
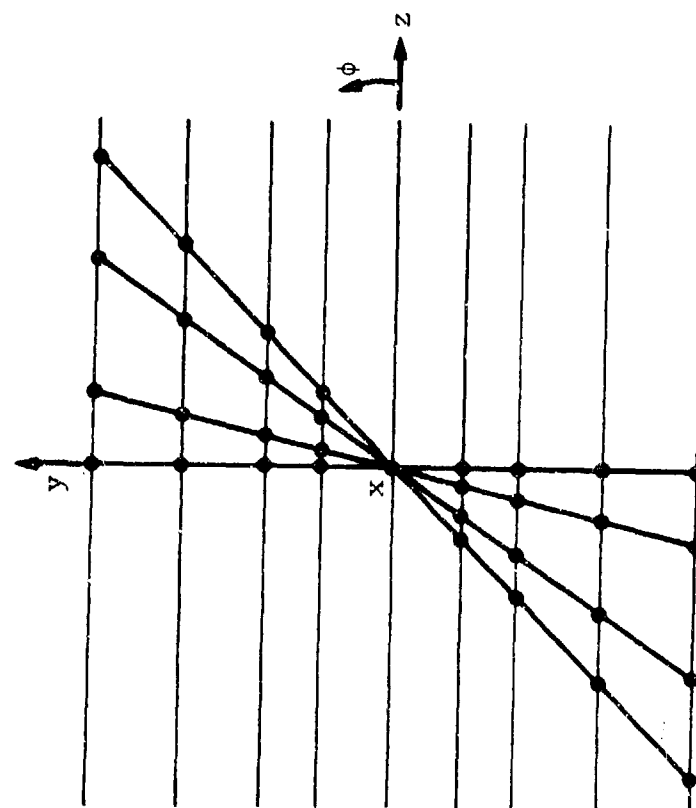
Figure 2-4. Cylindrical Shells and Lines of Sight

the source function for emission is also assumed constant over
the same region, but this is not a general requirement. The
unknowns are the radiances at the intersections of the cylindrical
shells with the parallel lines-of-sight. The constraints are the
transport equations for the intervening paths together with the
boundary conditions for each line of sight. Together they consti-
tute a determinate linear set. In the figure, the rectangular
z, y, x coordinates denote the plume axis, the line-of-sight
direction, and the line-of-sight spacing, respectively. The
spherical r, Θ, ϕ coordinates denote the radius, azimuth, and
elevation of the local radiance vectors. The integration paths
are determined by prescribed values of x and ϕ where the x's are
chosen to correspond to the radii of the cylindrical shells.
The integrations are performed over half of the azimuth plane
($-\pi/2 < \Theta < \pi/2$) and half the elevation plane ($0 < \phi < \pi/2$) or one-
fourth of the radiating volume (π steradians). The remaining
volume is described by symmetry relations through simple
reflections in Θ and ϕ.

Figure 2-5 shows the relationship between the radiances and
the source functions at different radial stations which provides
the coupling mechanism for multiple lines-of-sight. This relation-
ship is based on the assumption of infinite axial symmetry such
that the properties of the medium vary only with radius. Positive
or negative radiance vectors are constructed from line-of-sight rad-
iances directed outward or inward, respectively. In the elevation

SOURCE FUNCTION

RADIANCE

a) Elevation Plane
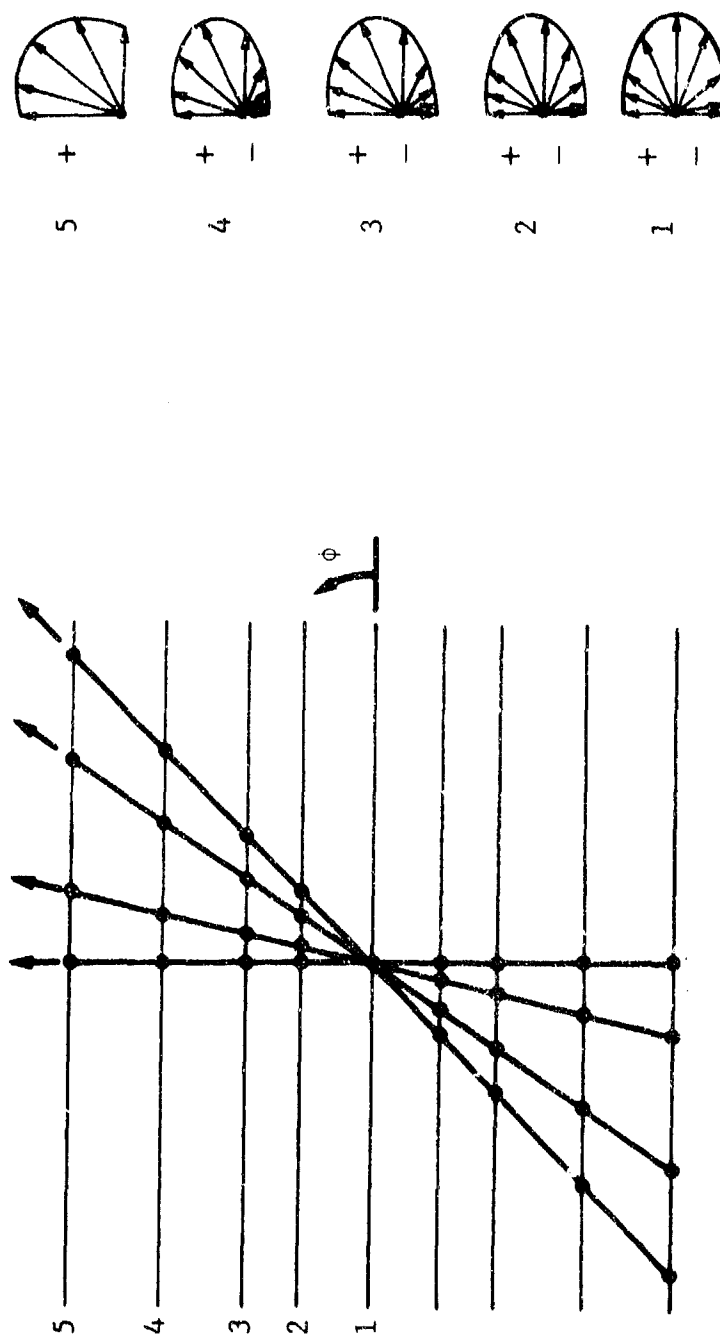
Figure 2-5a. Radiances and Source Functions

2-38

b) Azimuth Plane

SOURCE FUNCTION
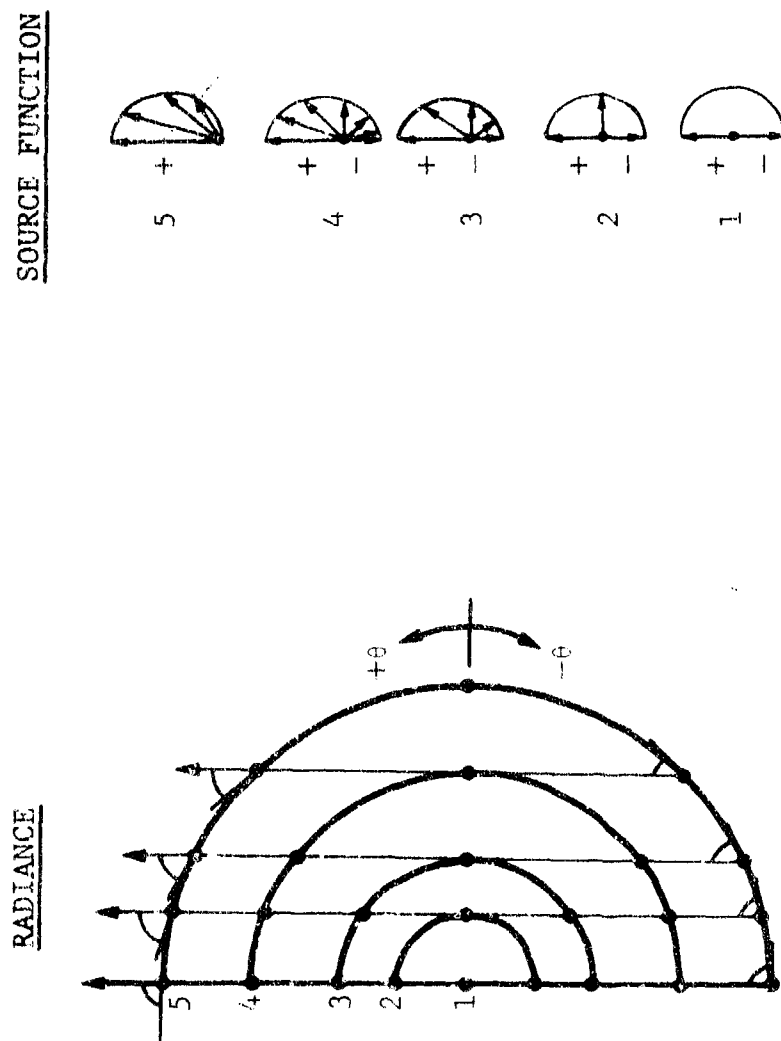
RADIANCE

Figure 2-5b. Radiances and Source Functions

plane, the source function is approximated by an angular quadrature of fixed resolution given by the prescribed values of aspect angle. In the azimuth plane, the source function is approximated by an angular quadrature of variable resolution which increases in proportion to the prescribed number of cylindrical shells. The resolution increases from the center (where the radiation field is isotropic by symmetry) to the edge (where the radiation field is most anisotropic) such that the accuracy of the quadrature is maintained independent of radius.

Figure 2-6 shows the indexing system for the matrix elements in the azimuth plane. The indices i and k designate the spacing (x) of the line-of-sight and the radius (r) of the cylindrical shell. The index j (which does not affect the azimuth plane projection) designates the elevation angle (ϕ) of the line-of-sight relative to the cylinder axis. The i,k matrix elements form an asymmetric square array in which the ordering of the subscripts indicates the direction of the path (outward or inward).

Figure 2-7 shows the geometric relations for each matrix element in the azimuth plane. The inclination of the radiance vector relative to the radial direction is given by the complement of the angle θ_{ik} or θ_{ki} where

$$\theta_{ik} = -\theta_{ki} = \cos^{-1}\left(\frac{r_i}{r_k}\right) \quad ; \quad \theta_{ik} = \pi/2 \quad .$$

The line-of-sight distance s_{ijk} or s_{kji} measured from the mid-point (x-axis) to the point k is given by
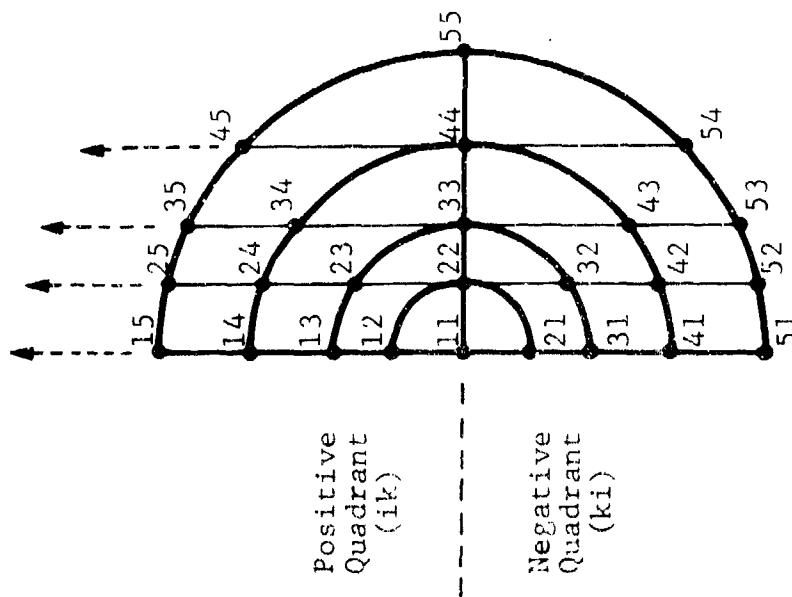
2-40

MATHEMATICAL SPACE

+ = positive quadrant
— = negative quadrant
0 = boundary

PHYSICAL SPACE

Figure 2-6. Matrix Element Indexing in Azimuth Plane

2-41
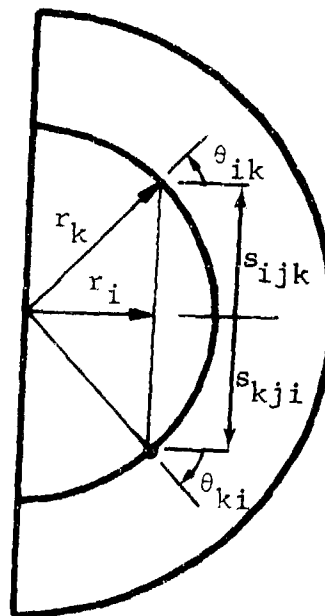
Figure 2-7. Geometrical Relations
in Azimuth Plane

$$s_{ijk} = -s_{kji} = r_k \frac{\sin \theta_{ik}}{\sin \phi_j} \quad .$$

For uniform properties (ρ_k, κ_k) between points k and k + 1, the transmission is given by

$$T_{ijk} = \exp\left[-\rho_k \kappa_k \left(s_{ijk+1} - s_{ijk}\right)\right] \quad .$$

With these definitions, the equation of transport between points k and k + 1 in the lower quadrant and points k - 1 and k in the upper quadrant may be written as

$$
\left.
\begin{aligned}
N_{kji} &= N_{k+1ji} T_{ijk} + \left[\left(1 - \omega_k\right)N_k{}^0 + \frac{\omega_k}{2}\left(S_{kji}\right.\right. \\
&\quad \left.\left. + S_{k+1ji}\right)\right]\left(1 - T_{ijk}\right) \\
N_{ijk} &= N_{ijk-1} T_{ijk-1} + \left[\left(1 - \omega_{k-1}\right)N_{k-1}{}^0\right. \\
&\quad \left. + \frac{\omega_{k-1}}{2}\left(S_{kji} + S_{k-1ji}\right)\right]\left(1 - T_{ijk-1}\right)
\end{aligned}
\right\} \quad (2\text{-}18)
$$

where ω_k and ρ_k are uniform between points k and k + 1. The source function S accounts for multiple scattering from all directions into the line of sight.

$$
\left.
\begin{aligned}
S_{ijk} &= \sum_{i'=1}^{k} \sum_{j'=1}^{J} \left(P_{ii'kjj'} N_{i'j'k} + P_{iki'jj'} N_{kj'i'}\right) \Omega_{i'j'k} + P_{oj} N_{ok} \Omega_o \\
S_{kji} &= \sum_{i'=1}^{k} \sum_{j'=1}^{J} P_{i'kij'j} N_{i'j'k} + P_{ki'ij'j} N_{kj'i'} \; \Omega_{i'j'k} + P_{oj} N_{ok} \Omega_o
\end{aligned}
\right\} \quad (2\text{-}19)
$$

where

$\qquad$ k = number of discrete azimuth angles at radius r_k

J = total number of discrete elevation angles

$P_{ii'kj'j}$ = phase function for scattering from direction $\theta_{i'k}$, $\phi_{j'}$, and its symmetric counterparts into direction θ_{ik}, ϕ_j

Ω_{ijk} = solid angle for radiance vector N_{ijk} or N_{kji}

o = subscript for axial component ($\phi_o = 0$).

The axial component of the source function (subscript zero) is excluded from the double sum for reasons of symmetry. Symmetry with respect to z yields the following expression for axial radiance

$$N_{ok} = \left(1 - \omega_k\right)N_k^{\,o} + \omega_k S_{ck}$$

Symmetry with respect to θ yields the following expression for axial source function

$$S_{ok} = \sum_{j=1}^{J} P_{jo} \sum_{i=1}^{k} \left(N_{ijk} + N_{kji}\right)\Omega_{ijk} + P_{oo}N_{ok}\Omega_o$$

Substitution of S_{ok} into N_{ok} and N_{ok} into N_{ijk} and N_{kji} eliminates N_{ok} from the radiance matrix. These values are computed independently subsequent to solution of the matrix.

The solid angles are evaluated in terms of the discrete spherical coordinates θ_{ik}, ϕ_j shown in Figure 2-8. The solid angle boundaries are assumed to bisect the angular region between adjacent radiance vectors such that, for an interior element,

$$\Omega_{ijk} = -\left(\frac{\theta_{i+1,k} - \theta_{i-1,k}}{2}\right)\left[\cos\left(\frac{\phi_j + \phi_{j-1}}{2}\right) - \cos\left(\frac{\phi_j + \phi_{j+1}}{2}\right)\right] \qquad (i \neq 1,k \; ; \; j \neq J)$$
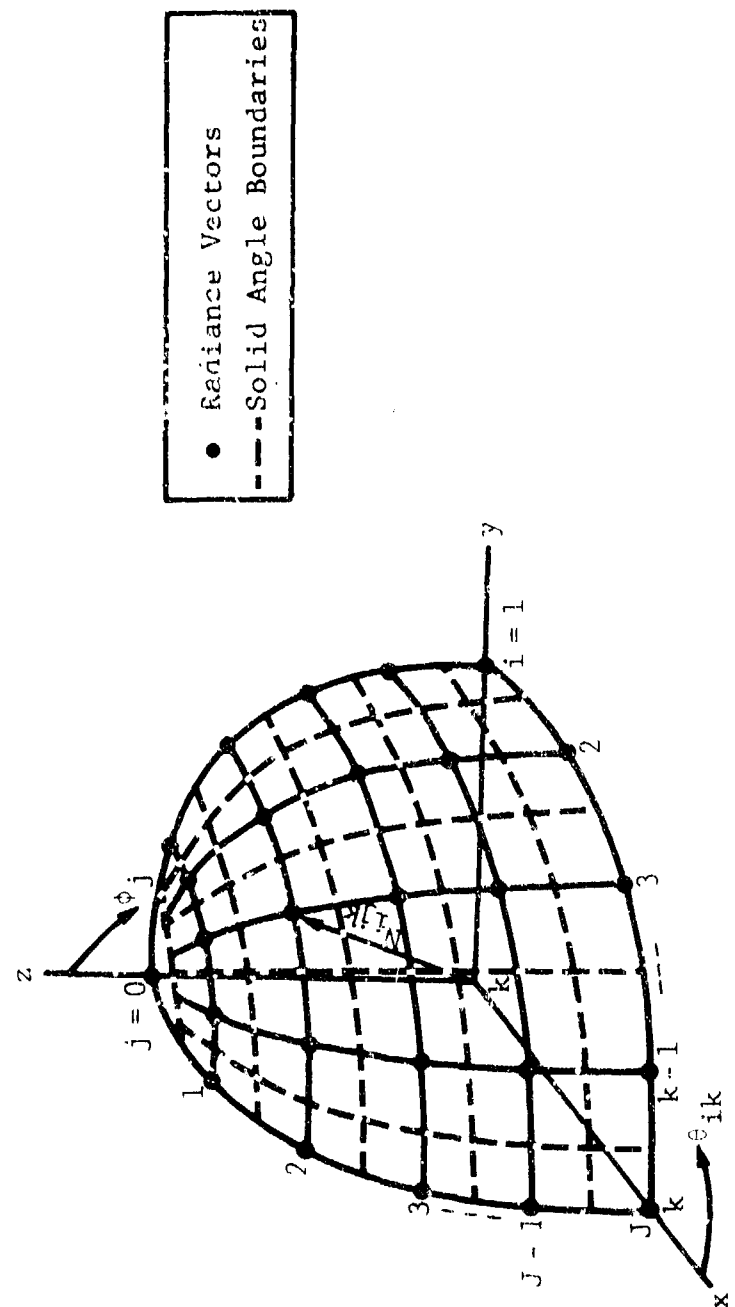
Figure 2-8. Radiance Vectors and Solid Angles

For an exterior element, the solid angle is one-half (edge) or one-fourth (corner) the value given by the above formula; i.e.,

$$\Omega_{1jk} = -\left(\frac{\theta_{2k} - \theta_{1k}}{2}\right)\left[\cos\left(\frac{\phi_j + \phi_{j-1}}{2}\right) - \cos\left(\frac{\phi_j + \phi_{j+1}}{2}\right)\right]$$

$$i = 1 \; ; \; j \neq J \; \text{(edge)}$$

$$\Omega_{kjk} = -\left(\frac{\theta_{kk} - \theta_{k-1,k}}{2}\right)\left[\cos\left(\frac{\phi_j + \phi_{j-1}}{2}\right) - \cos\left(\frac{\phi_j + \phi_{j+1}}{2}\right)\right]$$

$$i = k \; ; \; j \neq J \; \text{(edge)}$$

$$\Omega_{iJk} = -\left(\frac{\theta_{i+1,k} - \theta_{i-1k,k}}{2}\right)\left[\cos\left(\frac{\phi_J + \phi_{J-1}}{2}\right) - \cos \phi_J\right]$$

$$j = J \; ; \; i \neq 1,k \; \text{(edge)}$$

$$\Omega_{1Jk} = -\left(\frac{\theta_{2k} - \theta_{1k}}{2}\right)\left[\cos\left(\frac{\phi_J + \phi_{J-1}}{2}\right) - \cos \phi_J\right]$$

$$i = 1 \; ; \; j = J \; \text{(corner)}$$

$$\Omega_{kJk} = -\left(\frac{\theta_{kk} - \theta_{k-1,k}}{2}\right)\left[\cos\left(\frac{\phi_J + \phi_{J-1}}{2}\right) - \cos \phi_J\right]$$

$$i = k \; ; \; j = J \; \text{(corner)}$$

For the axial component, the solid angle is given by

$$\Omega_o = \pi\left(1 - \cos \frac{\phi_1}{2}\right) .$$

The phase function is evaluated in terms of the angle β formed between the given radiance vector and the line-of-sight.

This angle is readily evaluated from the vector dot product of the corresponding unit vectors $\hat{r}_{i'j'k}$ and $\hat{r}_{ijk}$ where

$$\hat{r}_{ijk} = \hat{x} \sin \phi_j \cos \theta_{ik} + \hat{y} \sin \phi_j \sin \theta_{ik} + \hat{z} \cos \phi_j \quad .$$

Thus,

$$\hat{r}_{i'j'k} \cdot \hat{r}_{ijk} = \sin \phi_{j'} \sin \phi_j \left[\cos \left(\theta_{i'k} - \theta_{ik} \right) \right]$$

$$+ \cos \phi_{j'} \cos \phi_j$$

$$= \cos \beta_{i'j'kij} \quad .$$

The phase function is defined to include scattering not only from the direction $\theta_{i'k}, \phi_{j'}$ but also from the symmetric directions $\pi - \theta_{i'k}$ and $\pi - \phi_{j'}$ such that

$$P_{1i'kjj'} = P\left[\beta\left(\theta_{i'k}, \phi_{j'}, \theta_{ik}, \phi_j \right) \right]$$

$$+ P\left[\beta\left(\pi - \theta_{i'k}, \phi_{j'}, \theta_{ik}, \phi_j \right) \right]$$

$$+ P\left[\beta\left(\theta_{i'k}, \pi - \phi_{j'}, \theta_{ik}, \phi_j \right) \right]$$

$$+ P\left[\beta\left(\pi - \theta_{i'k}, \pi - \phi_{j'}, \theta_{ik}, \phi_j \right) \right] \quad .$$

For the axial component, the phase function is given by

$$P'_{jo} = 2\left[P\left(\phi_j \right) + P\left(\pi - \phi_j \right) \right] \quad .$$

In this manner, the computed radiation field for π-steradians is made to account for scattering from 4π-steradians.

The preceding equations may be solved by either iterative or inversion methods. In the iterative approach, the equations are suitable for programming without further manipulation. At

2-47

each iteration, the radiances N_{ok}, N_{ijk}, and N_{kji} are computed based on assumed values for S_{ok}, S_{ijk}, and S_{kji} from the preceding iteration subject to the boundary condition $N_{kji} = 0$ for all i,j (no external sources); the assumed values for the first iteration are taken equal to zero (i.e., single scattering). In the inversion approach, the equations are manipulated to eliminate the source functions S in favor of the radiances N which are subsequently determined by matrix inversion.

The manipulations required for the inversion method are summarized below. Elimination of S_{ok} in favor of N_{ok} yields

$$
N_{ok}\left(1 - \omega_k P_{oo}\Omega_o\right) = \left(1 - \omega_k\right)N_k{}^o + \omega_k \sum_{i=1}^{k} \sum_{j=1}^{J} P_{jo}\left(N_{ijk} + N_{kji}\right)\Omega_{ijk} \quad .
$$

Substitution of the N_{ok} into S_{ijk} yields

$$
S_{ijk} = \sum_{i'=1}^{k} \sum_{j'=1}^{J} \left\{ \left[P_{ii'kjj'} + x_{jk}\omega_k P_{jo}\right]N_{i'j'k} \right.
$$
$$
\left. + \left[P_{iki'jj'} + x_{jk}\omega_k P_{jo}\right]N_{kj'i'} \right\}\Omega_{i'j'k}
$$
$$
+ x_{jk}\left(1 - \omega_k\right)N_k{}^o
$$

where

$$
x_{jk} \equiv \frac{P_{jo}\Omega_o}{1 - \omega_k P_{oo}\Omega_o} \quad .
$$

Elimination of S_{ijk} and S_{kji} in favor of N_{ijk} and N_{kji} yields a $KJ(K-1)$ dimensional linear equation set, with $KJ(K-1)/2$ equations for each quadrant.

Positive Quadrant:

$$\sum_{i'=1}^{k} \sum_{j'=1}^{J} \left[\left(\delta_{i'j'ij} - \psi_{ijk-1} a_{ii'kjj'} \right) N_{i'j'k} \right.$$

$$\left. - \psi_{ijk-1} a_{iki'jj'} N_{kj'i'} \right] - \sum_{i'=1}^{k-1} \sum_{j'=1}^{J} \left[\left(\delta_{i'j'ij} T_{ijk-1} \right. \right.$$

$$\left. \left. + \psi_{ijk-1} a_{ii'k-1jj'} \right) N_{i'j'k-1} + \psi_{ijk-1} a_{iki'jj'} N_{k-1j'i'} \right]$$

$$= \psi_{ijk-1} x_{jk} \left(1 - \omega_k \right) N_k^{\,o} + \left(1 - T_{ijk-1} + \psi_{ijk-1} x_{jk-1} \right) \left(1 \right.$$

$$\left. - \omega_{k-1} \right) N_{k-1}^{\,o} \qquad \begin{cases} i = 1,k \\ j = 1,J \\ k = 2,K \end{cases}$$

Negative Quadrant:

$$\sum_{i'=1}^{k} \sum_{j'=1}^{J} \left[\left(\delta_{i'j'ij} - \psi_{ijk} a_{ki'ij'j} \right) N_{kj'i'} \right.$$

$$\left. - \psi_{ijk} a_{i'kij'j} N_{i'j'k} \right] - \sum_{i'=1}^{k+1} \sum_{j'=1}^{J} \left[\left(\delta_{i'j'ij} T_{ijk} \right. \right.$$

$$\left. \left. + \psi_{ijk} a_{k+1i'ij'j} \right) N_{k+1j'i'} + \psi_{ijk} a_{i'k+1ij'j} N_{i'j'k+1} \right]$$

$$= \psi_{ijk} x_{jk+1} \left(1 - \omega_{k+1} \right) N_{k+1}^{\,o} + \left(1 - T_{ijk} + \psi_{ijk} x_{jk} \right) \left(1 - \omega_k \right) N_k^{\,o}$$

$$\begin{cases} i = 1,k \\ j = 1,J \\ k = 1,K-1 \end{cases}$$

where

$$\psi_{ijk} \equiv \frac{\omega_k}{2}\left(1 - T_{ijk}\right)$$

$$a_{ii'kjj'} \equiv \left(P_{ii'kjj'} + x_{jk}\omega_k P_{jo}\right)\Omega_{i'j'k} \quad .$$

The above equations are subject to KJ boundary conditions

$$N_{Kji} = 0 \qquad\qquad \{i = 1,K \; ; \; j = 1,J\} \quad .$$

The above relations suffice to determine the entire $K^2 J$ dimen-
sional set of radiances for the cylinder. Repeated application
at successive axial stations yields the complete radiation field
for the plume.

2.6 Computed Results

Extensive parametric calculations were undertaken
in order to validate and compare the six-flux and N-flux
scattering approaches. The calculations included comparisons
with the predictions of other codes: the NASA finite-difference
code for plane-parallel geometries and the GAC Monte-Carlo
code for arbitrary geometries. The calculations were per-
formed for specified values of the monochromatic scattering
parameters (optical depth, scattering albedo, phase function)
rather than for a specified spectral region or particle size/
density distribution. This procedure enabled the scattering
codes to be exercised over the full range of optical environ-
ments without the attendant complexities of a complete system

simulation. The evaluation of the optical parameters in terms
of the physical properties of a specific gas/particle medium is
considered elsewhere in this report.

2.6.1 Planar media. The relative simplicity and general
availability of solutions for planar media make such solutions
ideal for the preliminary test of physical models and parametric
effects. This section summarizes results obtained for uniform
one- and two-dimensional planar media using an explicit six-flux
model (Method I; Figures 2-9 through 2-12) and a standard finite-
element program (NASA code; Figures 2-13 through 2-15) modified
to include thermal emission.

Figure 2-9 shows the transmissivity, reflectivity, and emis-
sivity of a uniform planar medium of unit optical depth at normal
aspect for various phase functions (isotropic, fore and aft,
forward only). In addition, isotropic scattering solutions are
compared for one- and two-dimensional planar media (slab vs.
ribbon) in order to bound the possible range of values for
cylindrical media. In all cases, scattering is observed to
reduce the emitted component and to increase the transmitted-
plus-reflected component of the radiation signature. Comparisons
among the slab solution for different phase functions show the
effects of backscattering (b>0) and side-scattering (s>0) on
the reflected and emitted components. Comparisons between the
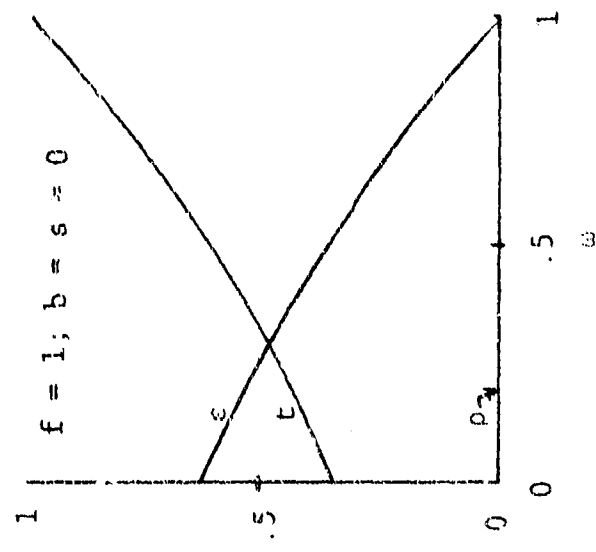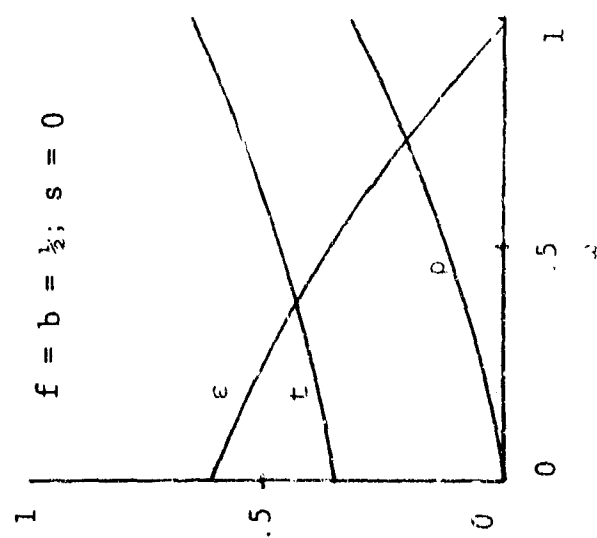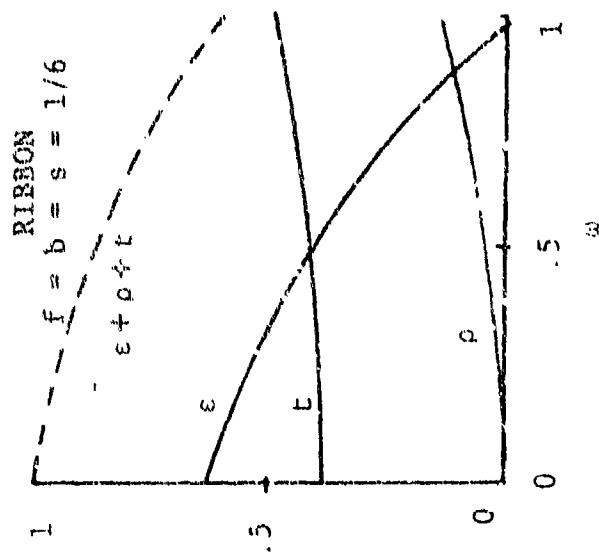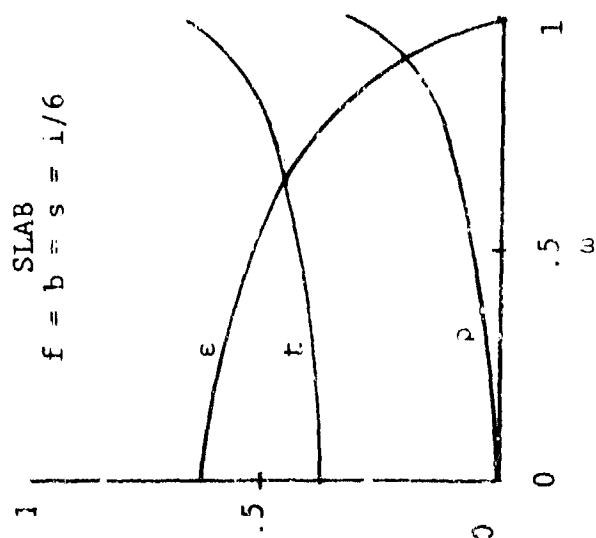
Figure 2-9. Transmissivity, Reflectivity, and Emissivity of Uniform Planar Medium at Normal Aspect ($\tau = 1$).

slab and ribbon solutions for isotropic scattering (f=b=s)
reveal essential differences between conservative ($\varepsilon + \tau + \rho = 1$)
and non-conservative ($\varepsilon + \tau + \rho < 1$) radiation fields which would
not be predicted by a two-flux model (s=0).

Figure 2-10 shows the transmissivity, reflectivity, and emis-
sivity of a uniform slab at tangent aspect for the same range
of parameters as in Figure 2-9. In this case, the incident ra-
diation is assumed to be perpendicular to the surface while the
observed radiation is parallel. Thus, the transmitted radiation
component undergoes a change in direction from the incident side
to the emergent side which accounts for $\tau \to 0$ as $\omega \to 0$. The
emitted component parallel to the slab is black (infinite optical
depth) only in the limit $\omega \to 0$; for finite ω, the emissivity is
reduced due to losses through the slab boundaries. Note that
this coupling between the normal and tangential radiance components
does not occur for the two-flux models.

Figure 2-11 shows the radiance of a uniform emitting planar
medium at normal aspect over a range of optical depths in the
absence of external radiation sources. The values are normalized
by the non-scattering solution for $\omega = 0$ and are therefore
equivalent to normalized emissivities. The range of scattering
parameters and geometries is the same as in Figures 2-9 and
2-10. In all cases, increased scattering (ω) is observed to
reduce the observed radiance for constant τ due to equal but

2-53
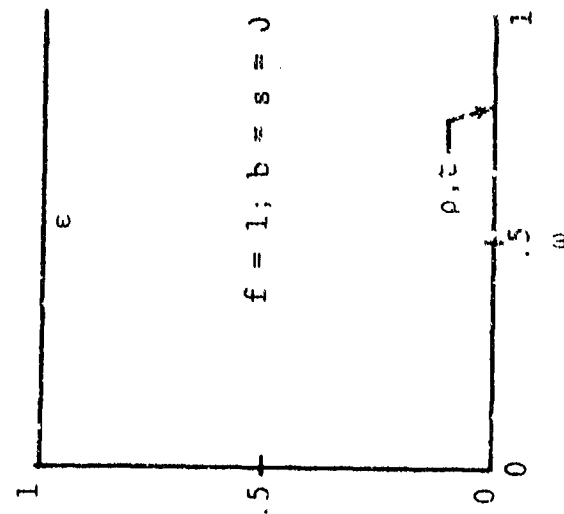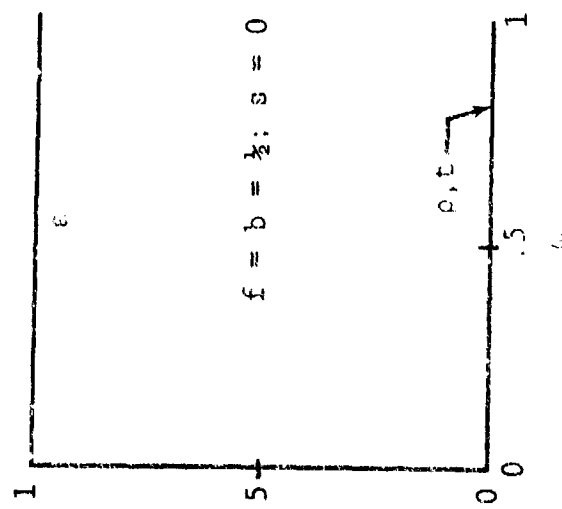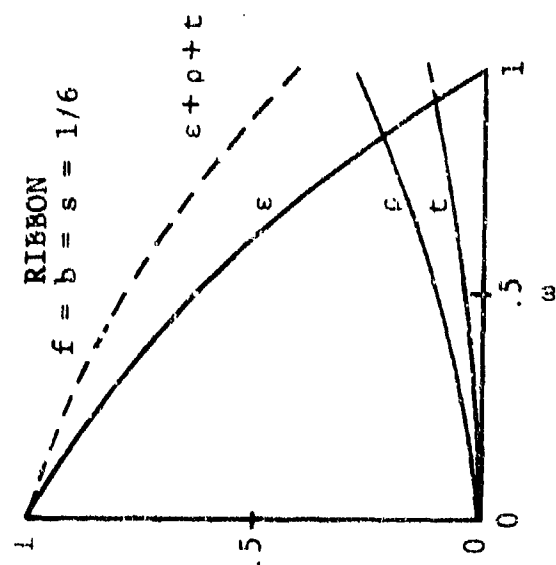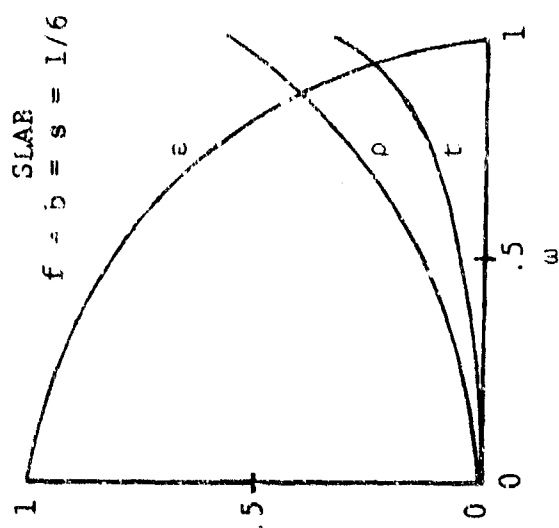
Figure 2-10. Transmissivity, Reflectivity, and Emissivity of Uniform Planar Medium at Tangent Aspect ($r=1$).
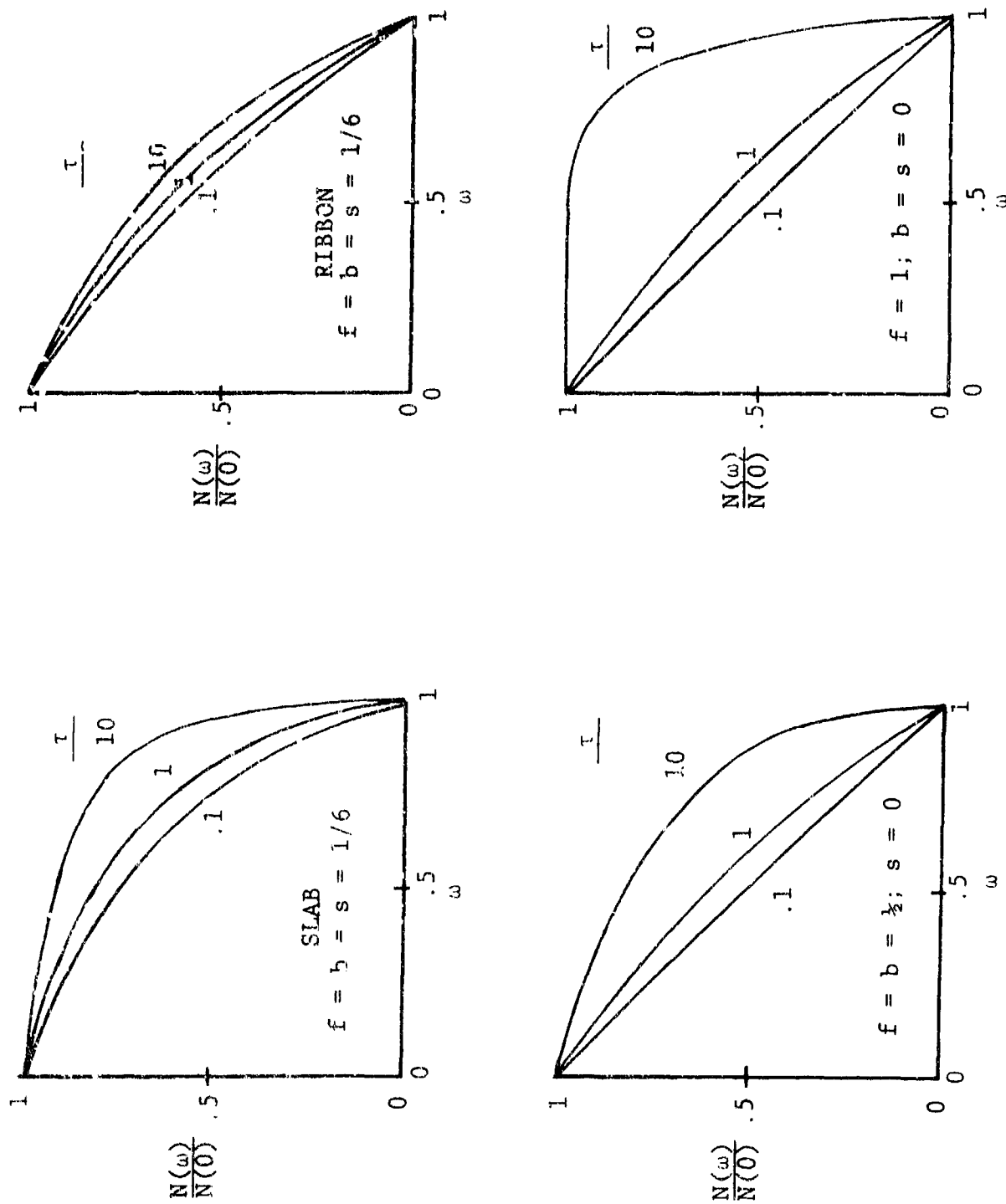
Figure 2-11. Normal Radiance versus Albedo for Uniform Planar Medium

opposite variations in the optical depths for absorption and
scattering. The effect of side-scattering is observed to
increase the radiance from the slab relative to the ribbon
and from the six-flux relative to the two-flux (f=b in both cases)
but to decrease the radiance at large optical depths relative
to the forward-scattering case (f=1).

Although not shown, the normalized axial radiance component
$[N_z(\omega)/N_z(0)]$ exhibited close similarity to the normalized
radial component $[N_r(\omega)/N_r(0)]$ for isotropic scattering but
maintained constant value $[N_z(\omega)/N_z(0) = 1]$ for two-stream
scattering. The normalizing values $N_r(0)$ and $N_z(0)$ are simply
the given black body function (N^0) times the apparent emissivity
$(1-e^{-\tau_r}$ or unity, respectively). Thus, the six-stream approxi-
mation accounts for the redistribution of radiance (from axial
to radial) due to scattering whereas the two-stream approxi-
mation does not.

Figure 2-12 shows analogous results to Figure 2-11 except
that the optical depth parameter is based on the absorption
component rather than the total extinction (absorption + scatter-
ing). In this case, the emitted radiation remains constant as
ω increases rather than decreasing, as before, in proportion to
$(1-\omega)$. As a result, the curves lie above those in Figure 2-11
by an amount which increases with increasing ω. In the case of
forward scattering, the radiance remains finite in the limit
$\omega \to 1$.
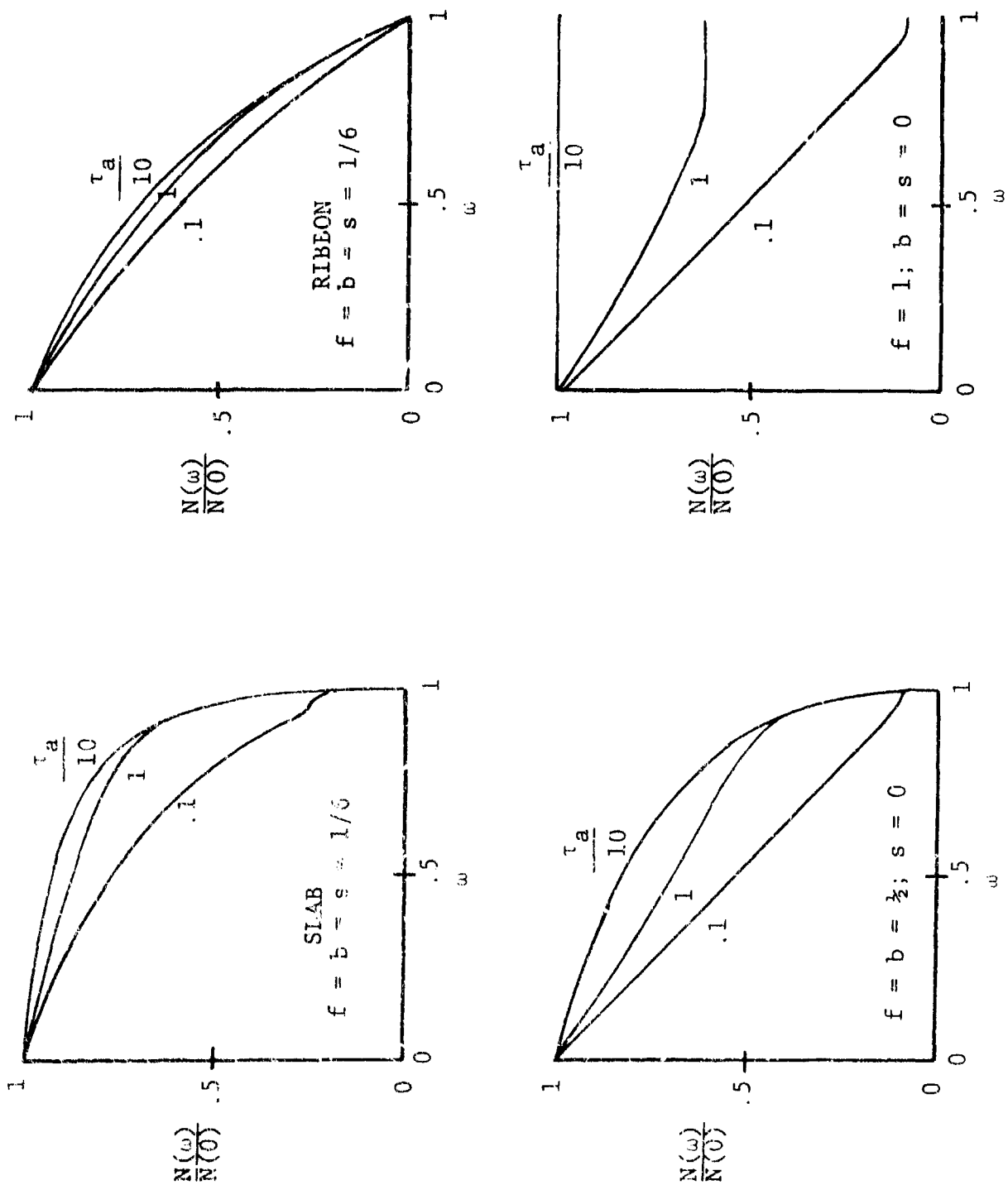
Figure 2-12. Normal Radiance versus Albedo for Uniform Planar Medium $[\tau = \tau_a/(1-\omega)]$

Figure 2-13 shows a comparison between the predictions of
the two-flux and six-flux models and the NASA finite-element
code for the normalized radiance at normal aspect from an iso-
tropically-scattering uniform slab of specified optical depth.
For small optical depth ($\tau = .1$), the NASA code is in close agree-
ment with the two-flux model ($f = b = \frac{1}{2}$). For large optical depth
($\tau = 10$), the NASA code is in close agreement with the six-flux
model ($f = b = s = 1/6$). For intermediate optical depth (based on a
single NASA code calculation), the NASA code prediction is inter-
mediate between the other two. Taking the NASA code as the
standard, this comparison provides physical insight into the
sources of error which can result from coarse angular quadrature.
In short, the two- and six-flux quadratures, respectively, under-
predict and over-predict the effective emissivity of the medium.
However, from the comparative results of Figures 2-9 to 2-13 for
slabs and ribbons, the error in the six-flux approximation at
small optical depths should be appreciably reduced for cylindrical
geometries (i.e. plumes).

Figures 2-14 and 2-15 show further comparisons between
predictions of the six-flux model and the NASA code for
an isotropically scattering uniform slab. These figures show
the variation with aspect angle of the radiance and radiant
intensity (radiance times projected area) normalized to their
respective values at normal aspect. The predictions of the six-
flux model (Method I) represent interpolations between the values
actually computed for normal and tangent aspect and, therefore,
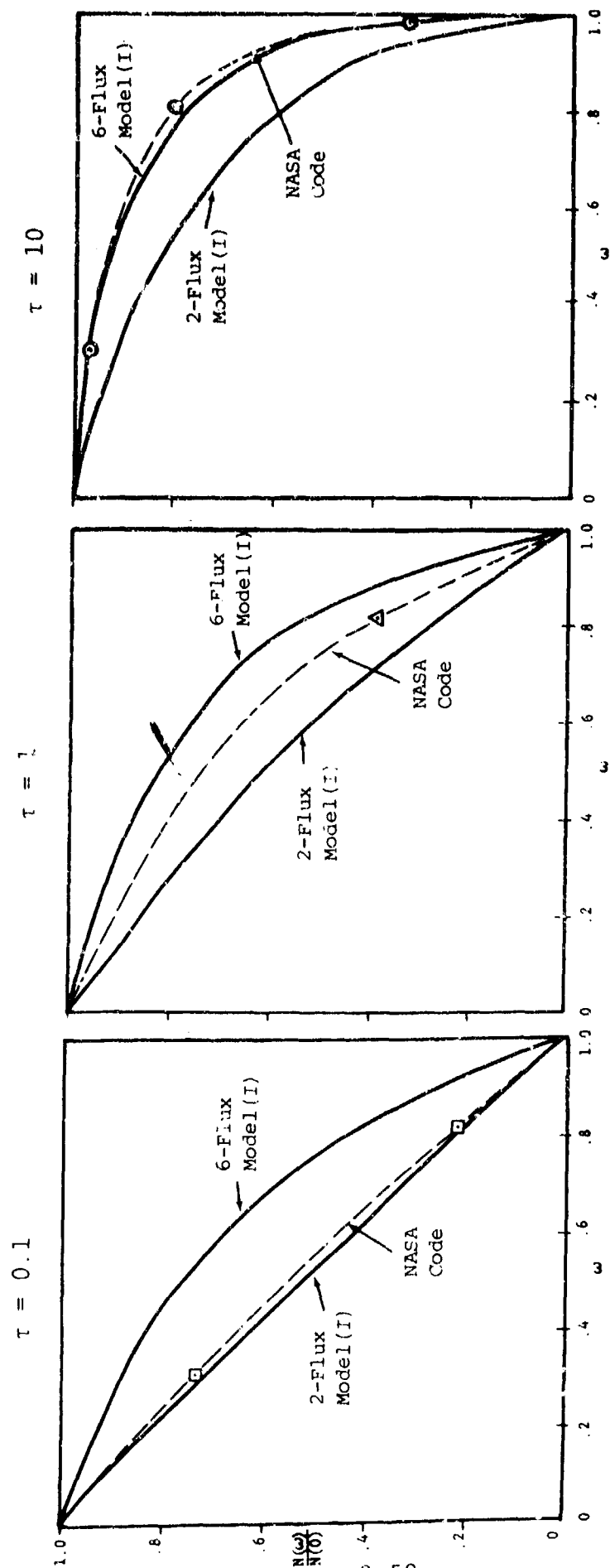
Figure 2-13. Normal Radiance versus Albedo for
Uniform Planar Medium (Isotropic Scattering).

2-59
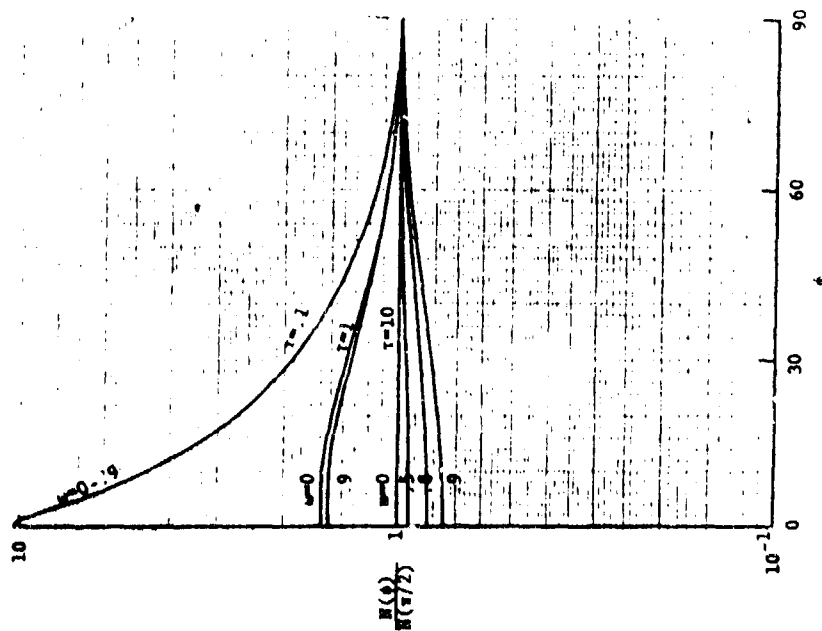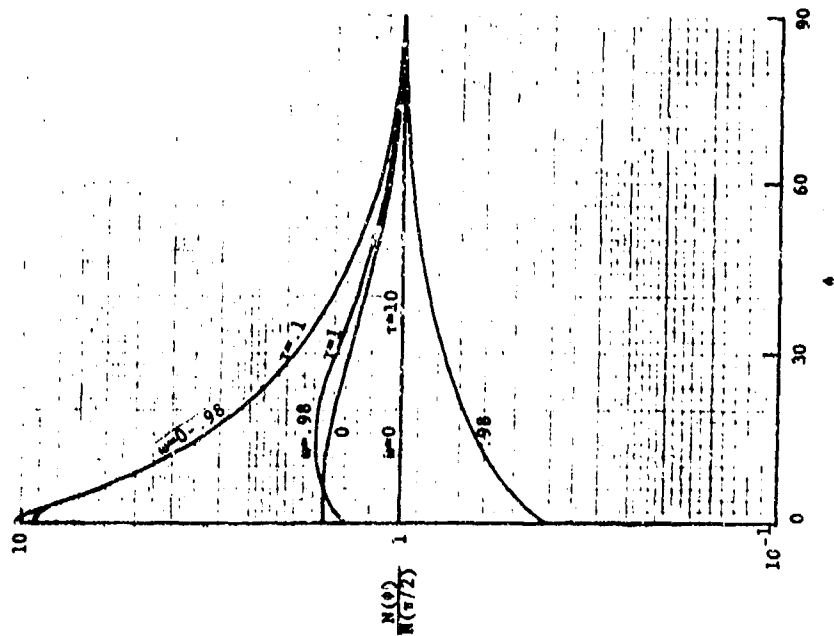
Figure 2-14. Radiance versus Aspect for Uniform Planar Medium
(Isotropic Scattering)
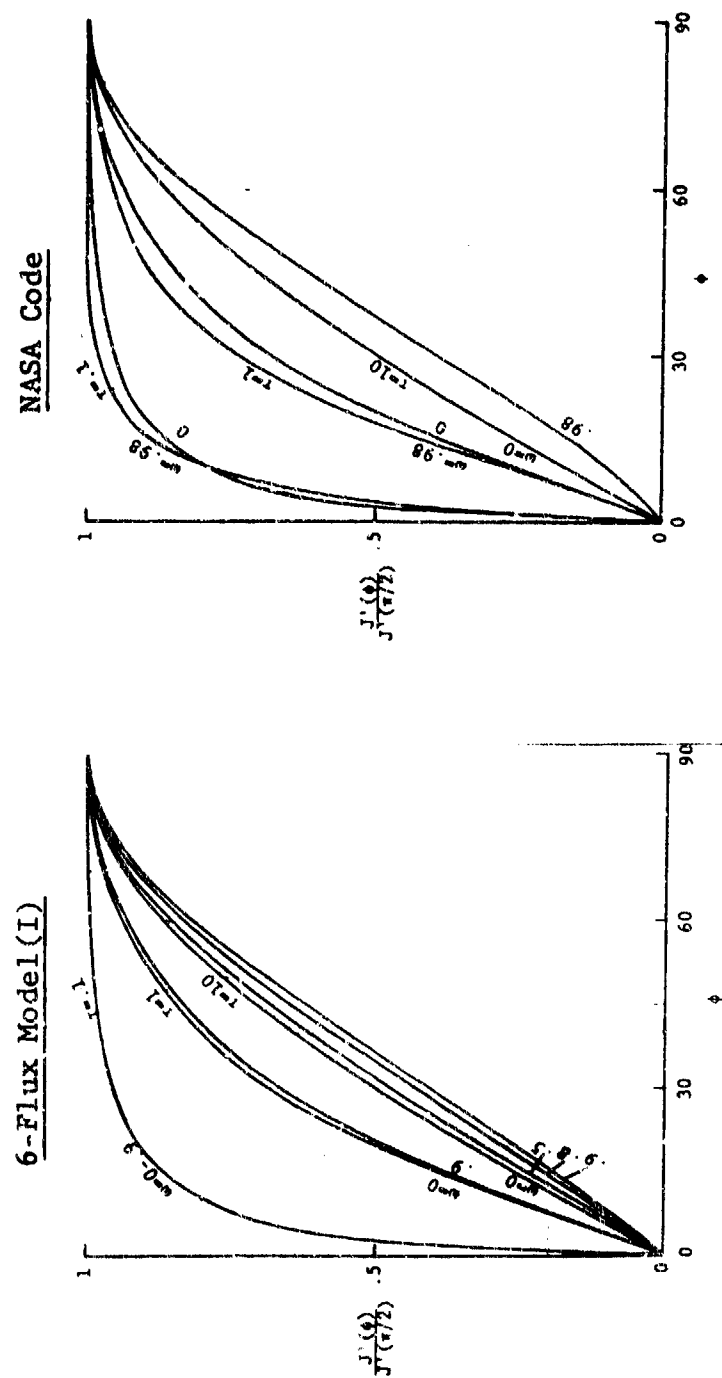
Figure 2-15. Radiant Intensity versus Aspect for Uniform Planar Medium (Isotropic Scattering)

have limited quantitative accuracy between those limits. However, the predictions and comparisons are useful to illustrate trends. In particular, both models predict the same qualitative variation of radiance with aspect (Figure 2-14) which is strongly dependent on optical depth. For small optical depths and low scattering albedos, the radiance increases toward tangent aspect due to the increased length of the optical path. However, for large optical depths and high scattering albedos, the radiance decreases toward tangent aspect due to side-scattering losses not predicted by two-flux models. The aspect dependence of the radiant intensity (Figure 2-15) includes the variation in projected area (proportional to $\sin \phi$) and, consequently, shows a monotonic decrease from normal to tangent aspect. In both Figures, the six-flux model predicts lower levels of radiation for higher scattering albedos, with greater sensitivity for larger optical depths. The opposite behavior of the NASA predictions for low optical depth does not lead to larger absolute differences.

2.6.2 Cylindrical media. Compared to the vast literature on multiple-scattering solutions for planar media, relatively little work has been published for cylindrical media. Accounting for this essential geometric effect was a central feature of the SIRRM model development. Hence, the logical first test of a new solution for cylindrical media is a comparison with previous solutions for planar media.

Figure 2-16 shows the normal radiance of a uniform infinite cylinder (centered line-of-sight) and of a uniform slab of equal optical depth. The predictions are based on the six-flux model (Method I or II) and on the GAC Monte Carlo code. Except in the non-scattering limit ($\omega=0$), the radiances are observed to be lower for the cylinder than for the slab due to side-scattering losses (not predicted by two-flux models). The six-flux and Monte Carlo results are shown to be in essential agreement for both isotropic and forward scattering phase functions. The forward scattering result is only slightly greater than the isotropic scattering result due to the assumption of uniform properties; larger sensitivities would be expected for the non-uniform conditions of actual plumes.

Figure 2-17 shows the normal radiance for isotropic scattering of a uniform infinite cylinder (centered line-of-sight) and of a uniform slab and ribbon of equal optical depth. The predictions are based on the 6-flux model (Method I or II) with comparative calculations from the N-flux model and the Monte Carlo code. The variation of radiance with optical depth (upper left plot) is qualitatively consistent with previous predictions for planar media (Figure 2-11). Specific comparisons for equal optical depths (remaining plots) show a uniform progression of the cylinder radiances from the ribbon values at small optical depths to the slab values at large optical depths. This behavior is the result of side-scattering losses from the cylinder which increase with decreasing optical depth. These losses

2-63
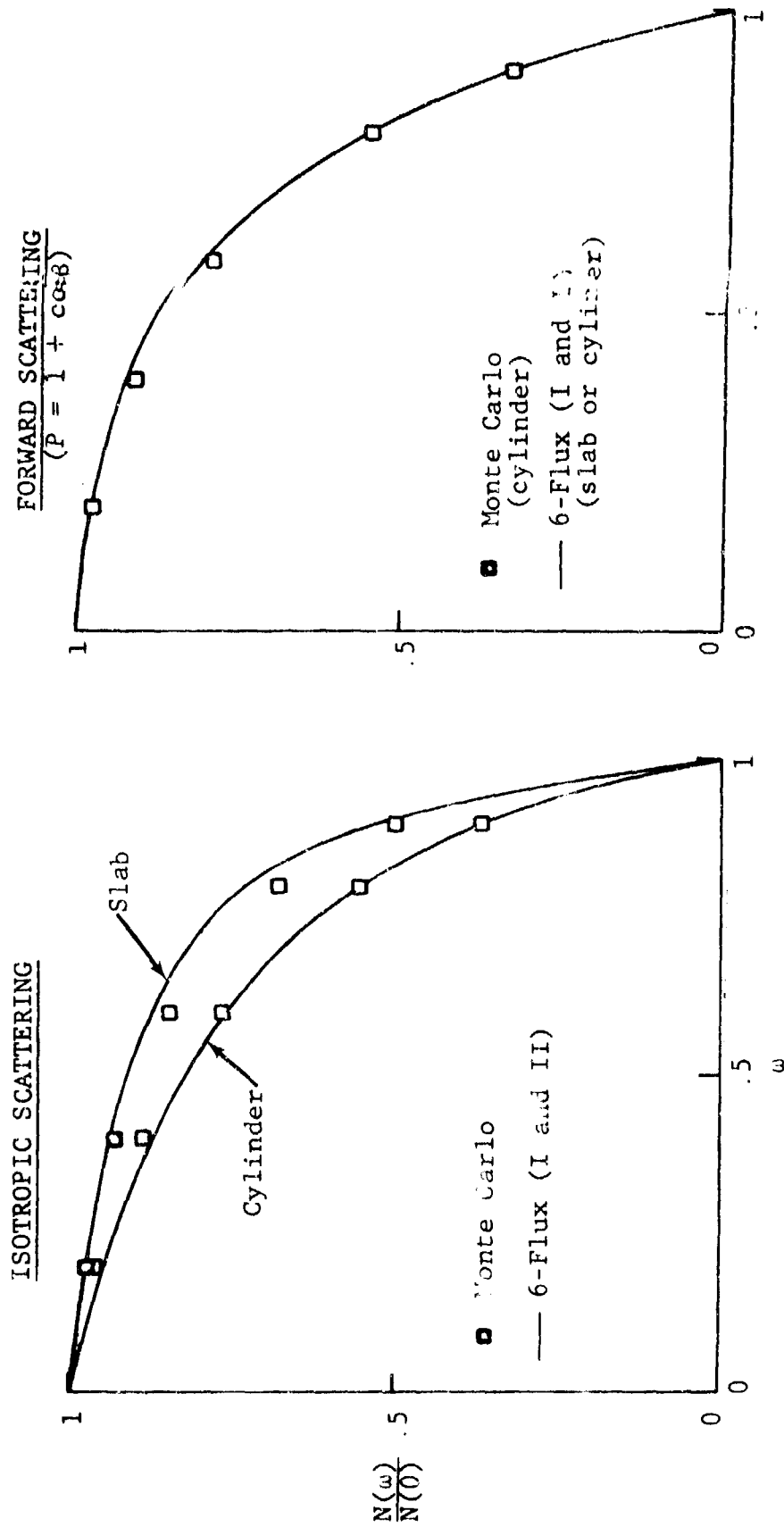
Figure 2-16. Normal Radiance versus Albedo for Uniform Media (4.0)
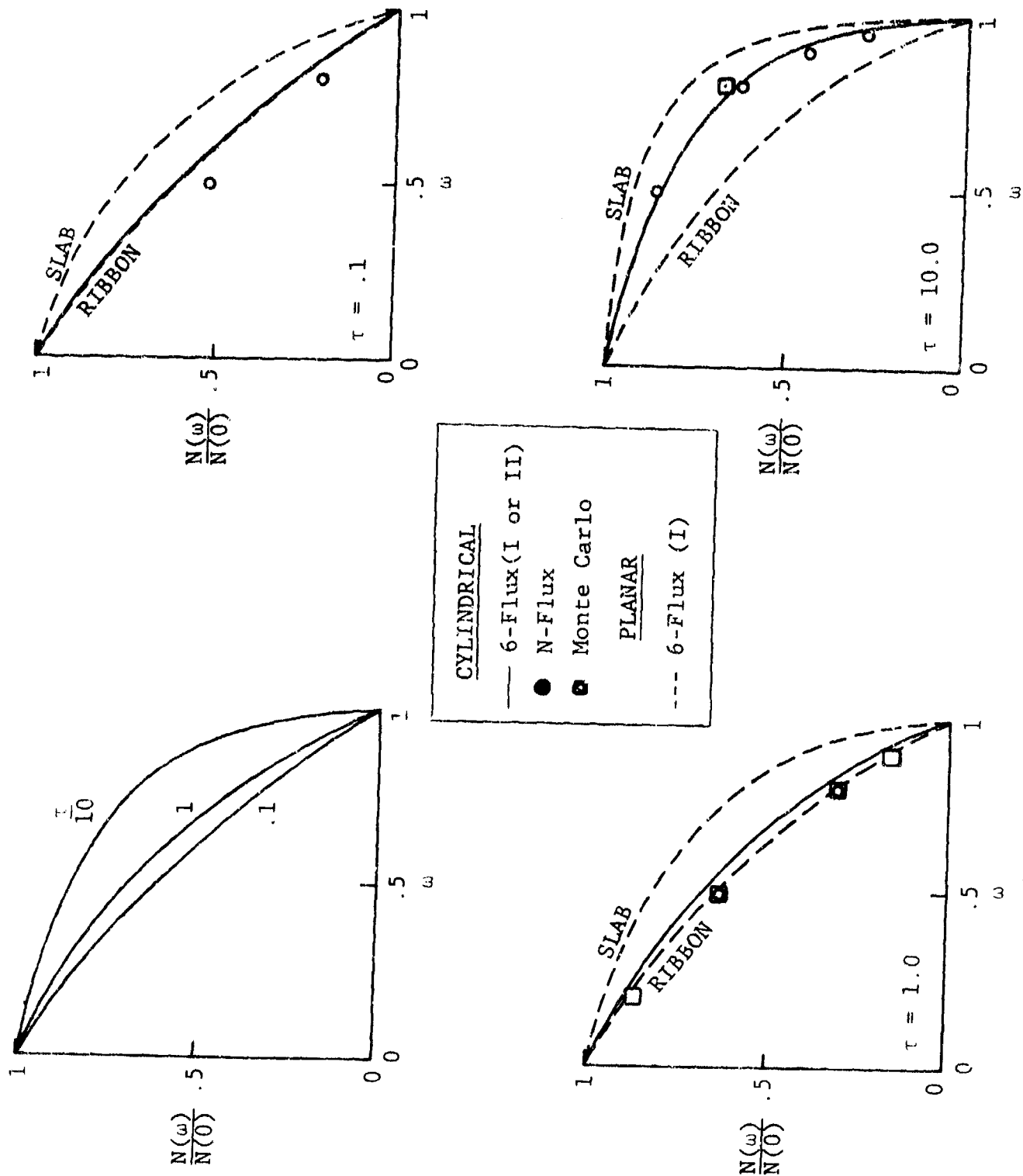
Figure 2-17. Normal Radiance versus Albedo for Uniform Media (isotropic scattering)

result in improved predictive accuracy for the six-flux model
at small optical depths. Comparison of the six-flux model pre-
dictions with the more exact predictions of the N-flux model and
Monte Carlo codes reveals a residual over-prediction for small
optical depths but substantial improvement relative to similar
predictions for a slab (compare Figure 2-13). Comparison of the
N-flux and Monte Carlo predictions for unit optical depth revels
excellent agreement. The comparison is close but less exact at
an optical depth of ten.

Figure 2-18 shows the tangent radiances (i.e., aspect = 0
or 180 degrees) for the same conditions as the normal radiances
in Figure 2-17. As before, the curves are shown normalized by
their values for a non-scattering medium, i.e., the local Planck
function $\left[N_z(\omega=0)=N^o\right]$. The curves reveal the same qualitative
trends as the normal radiances in Figure 2-17 except for a reduced
sensitivity to optical depth due to cylindrical curvature. As a
result, the tangent radiances remain close to the ribbon values
for all optical depths. This effect is confirmed by the more
exact predictions of the N-flux model and Monte Carlo code.

Figure 2-19 shows the aspect dependence of the emissivity
of a uniform infinite cylinder (centered line-of-sight) as
predicted for a given albedo by two-flux and six-flux model
approximations (Method II). The curves are qualitatively consis-
tent (but quantitatively different) for small optical depths near
normal aspect. However, for large optical depths near tangent
aspect, the two approximations predict opposite trends due to
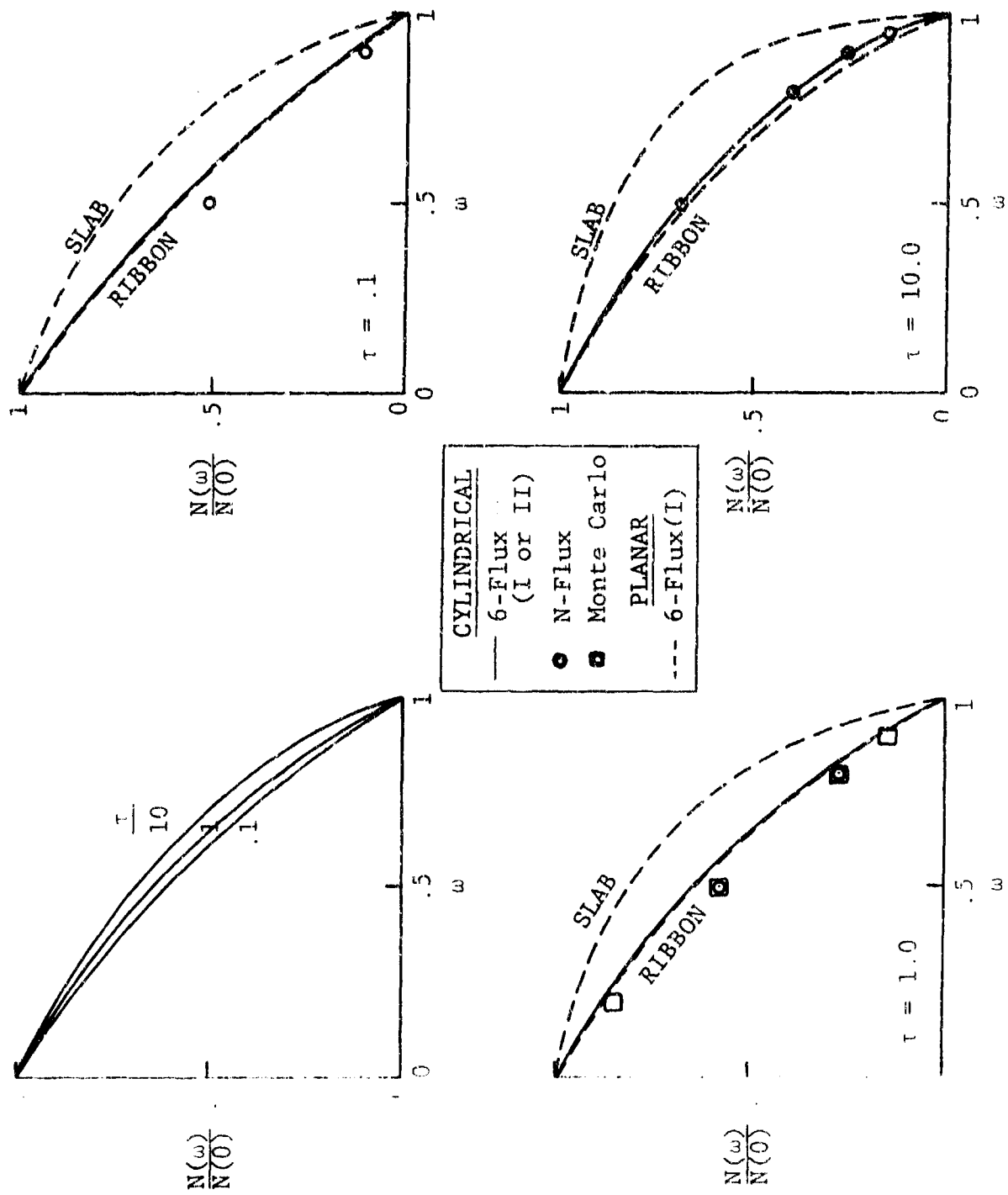
Figure 2-18. Tangent Radiance versus Albedo for Uniform Media (Isotropic Scattering)
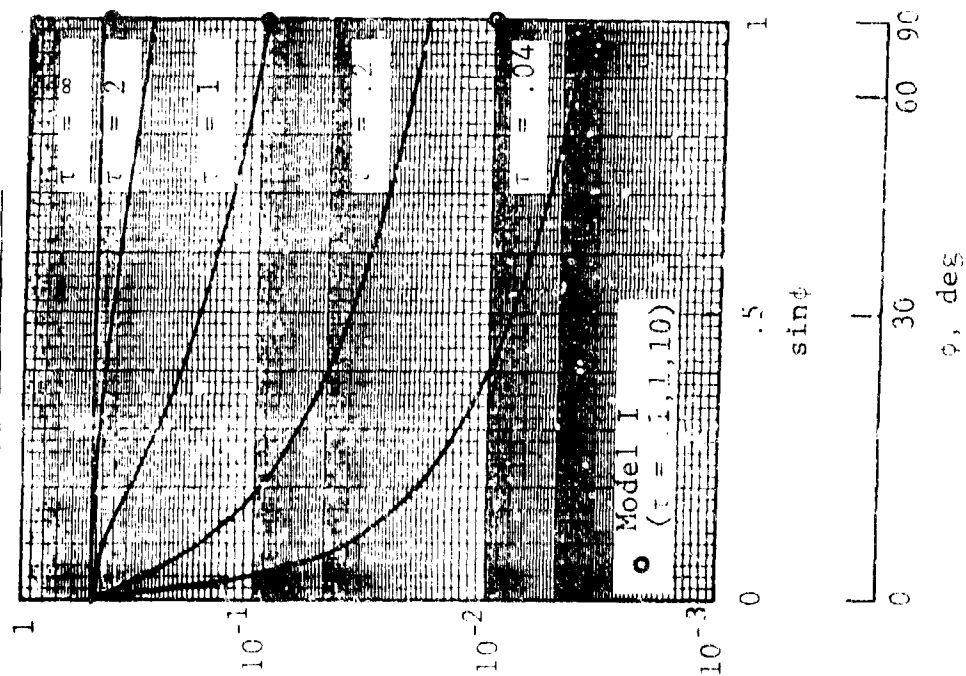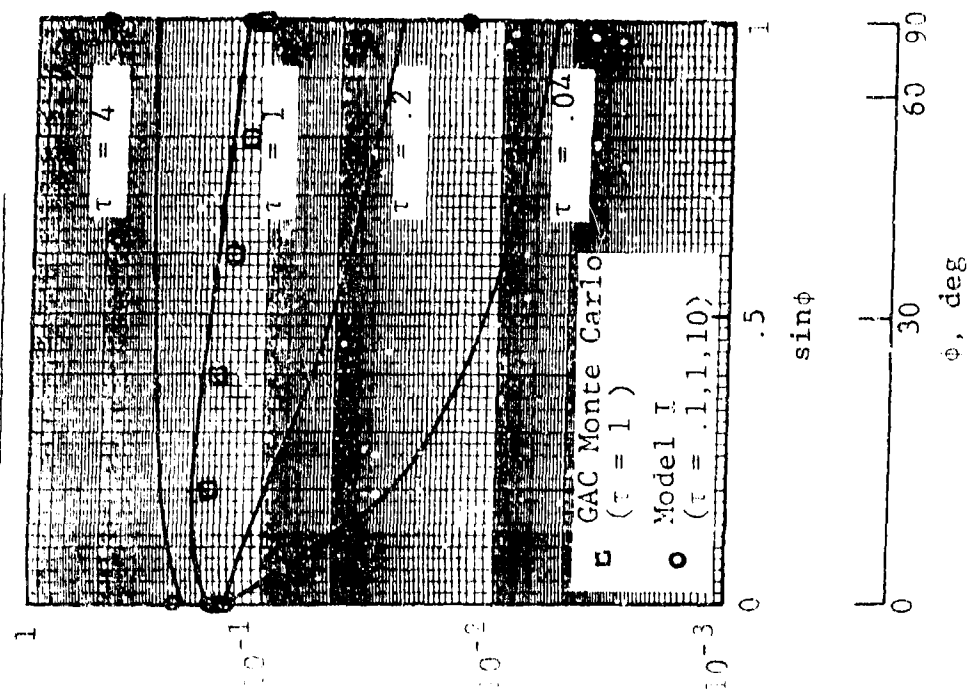
Fig. 2-19. Emissivity versus Aspect for Uniform Cylinder (ω=0.9, Isotropic Scattering)

the effect of side-scattering losses near grazing incidence. This behavior is consistent with previous predictions of radiance vs. aspect for a planar slab (Figure 2-14) and may have significant negative impact on the detectability of plumes from nose aspect. Comparison of the predictions of Method I and II for normal and tangent aspect reveals good agreement for both phase function approximations at comparable optical depths. Comparison of the predictions of Method II and the Monte Carlo code for isotropic scattering at unit optical depth reveals agreement within 20 percent for all aspect angles.

Figure 2-20 shows a comparison between the six-flux (Method I) and N-flux models for the normalized radiance from an isotropically scattering uniform infinite cylinder (centered line-of-sight) over the full range of albedo and optical depth. These curves are equivalent to normalized emissivities from Figure 2-19. As in Figure 2-14 (slab), the present six-flux predictions represent interpolations between the values actually computed for normal and tangent aspect and, therefore, have limited quantitative accuracy between those limits. In particular, the Method I interpolation formulae are observed to under-predict relative to the N-flux model but to yield valid qualitative trends. Both models yield comparable predictions at normal and tangent aspects. Comparison of N-flux and Monte Carlo predictions are in excellent agreement and appear to confirm the 6-flux Method II predictions in Figure 2-19.
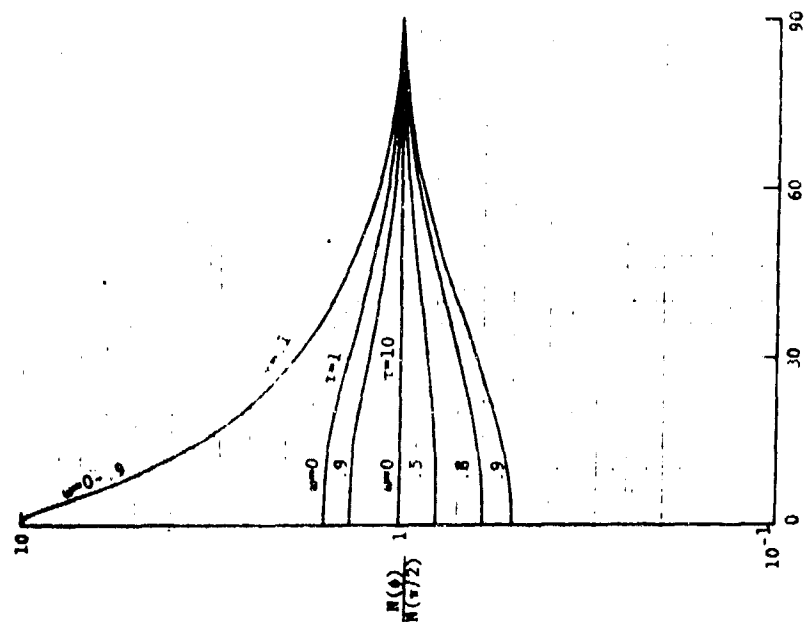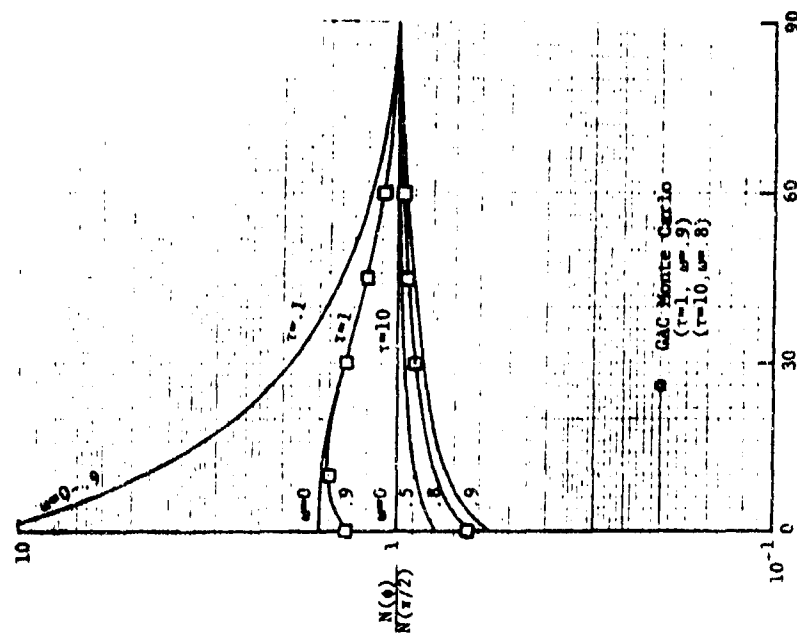
Figure 2-20. Centerline Radiance versus Aspect for Uniform Cylinder (Isotropic Scattering)

Figure 2-21 shows the N-flux model prediction for the variation of normal radiance with distance from the cylinder axis for the same conditions as Figure 2-20. Integration under these curves would yield the normalized station radiation at side aspect. The effect of scattering is to reduce the radiance from the off-axis regions, with greater sensitivity for larger optical depths. The assumption of the six-flux model I that the radiance profile is independent of albedo is, therefore, seen to be in error for large optical depth. This assumption is not made by six-flux model II.

Figure 2-22 shows a comparison between the six-flux (Method I) and N-flux model predictions for station radiation as a function of aspect angle for the same conditions as Figure 2-20. Both models predict the same qualitative effect of increasing albedo, namely, decreased radiation relative to side aspect with greater sensitivity for large optical depth. This behavior is consistent with previous 6-flux model predictions for a planar slab (compare Figure 2-15) except that the sensitivity to albedo is greater in the present case. However, the six-flux model (Method I) interpolation formulae appear to over-predict the sensitivity as predicted by the N-flux model and as confirmed by additional predictions with the GAC Monte Carlo code. The latter two predictions are shown to be in excellent agreement.
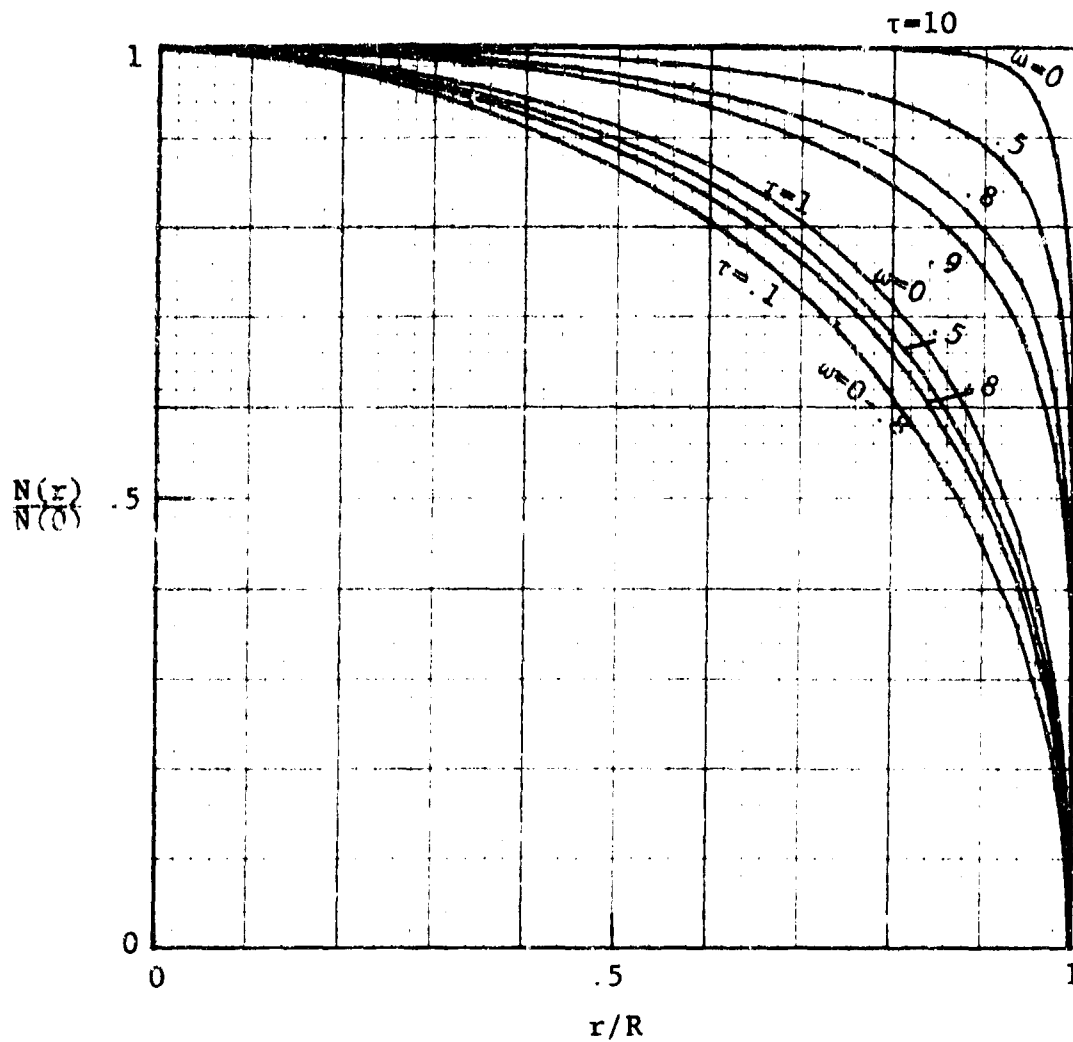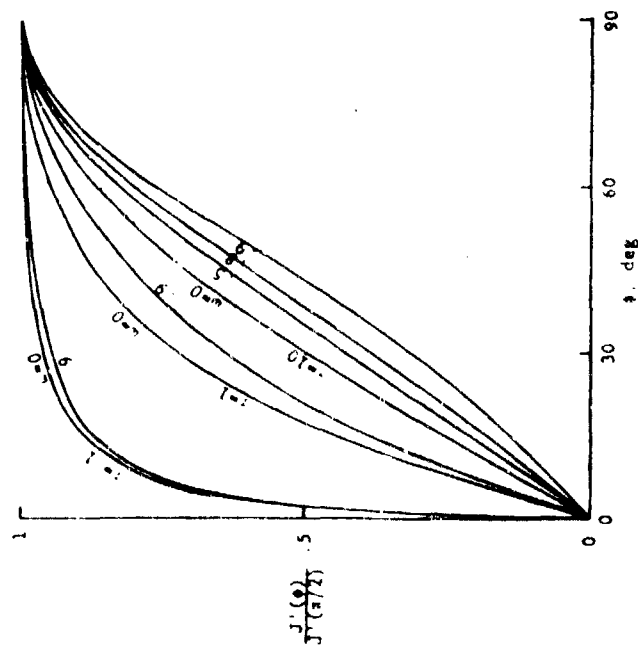
Figure 2-21. Normal Radiance versus Distance
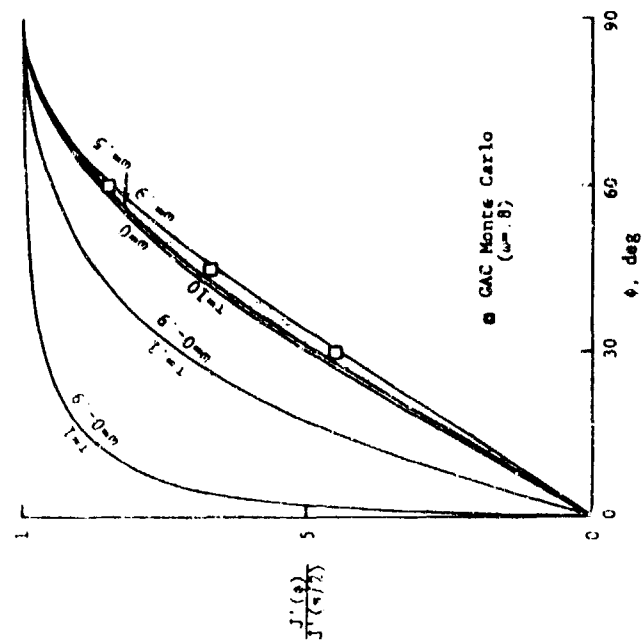from Centerline (Isotropic Scattering)

Figure 2-22. Radiant Intensity versus Aspect for
Cylinder (Isotropic Scattering)

The preceding results for infinite cylindrical media represent valid solutions for rocket plumes provided that the variation in axial radiance is negligible over a distance of one optical depth (i.e., $dN_z/d\tau_z << N_z$). This criterion is satisfied throughout most of the plume mixing region but may not be satisfied in local regions of the plume inviscid core when strong shocks are present. In order to assess the impact of shock-induced gradients on the coupled gas/particle radiation field, the six-flux model (Method II) was extended to finite cylindrical media with arbitrary end-wall boundary conditions. Numerical experiments were recently initiated to assess the impact of a strong external radiation source parallel to the axis on the radiation scattered to side aspect. A key objective of this assessment is the determination of the axial region of influence beyond which the infinte cylinder model becomes a valid approximation.

Figure 2-23 shows the result of a preliminary test calculation with the extended six-flux model. In this case, the cylinder is assumed uniform with no external radiation source such that the computed radiation field is symmetric about the cylinder mid-point. The radial and axial emissivities are observed to decrease from the mid-points toward the corners as a result of three-dimensional radiation-coupling effects. For the given optical depths, the mid-point radial emissivity is nearly equal to the emissivity of an infinite cylinder; i.e., the mid-point
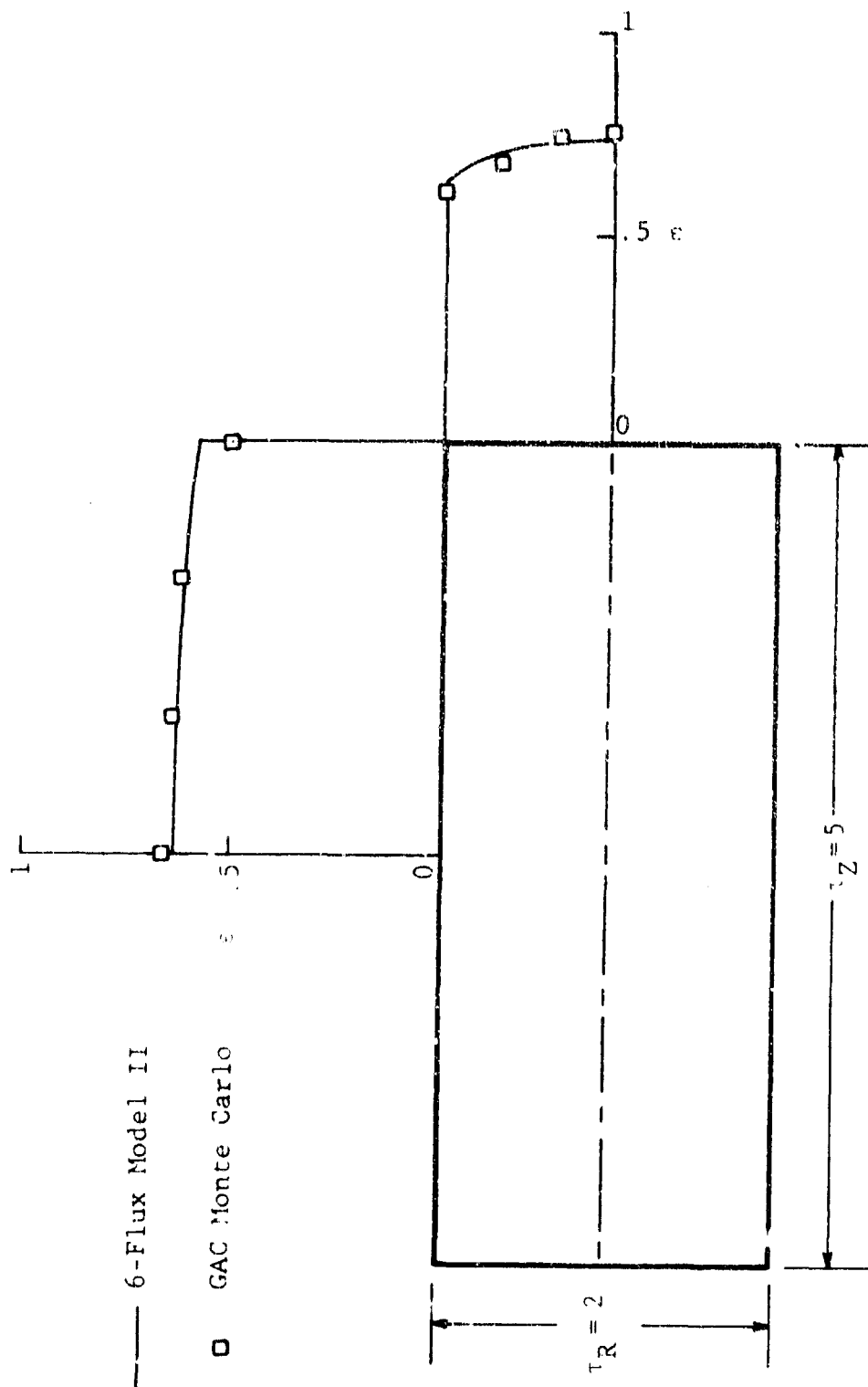
Figure 2-23. Axial and Radial Emissivities for Finite Cylinder (Isotropic Scattering; ω=.5)

values are nearly independent of end-wall boundary conditions.
Thus, the axial region of influence is contained within the finite
cylinder considered. Comparative Monte Carlo predictions appear
to validate the six-flux model result.

As a last test case, a condition of practical significance
was chosen. It involves an occulted emitting core and a non-
emitting scattering envelope, simulating a nose aspect signature
(see Figure 2-24). This is a stringent test case because the
nose aspect signature is due entirely to scattering and because
the core is a localized source leading to a highly anisotropic
radiation field. A comparison between the forward scattered
radiance predicted by the 6-flux model (Method II) and the Monte
Carlo method showed agreement within 20%.
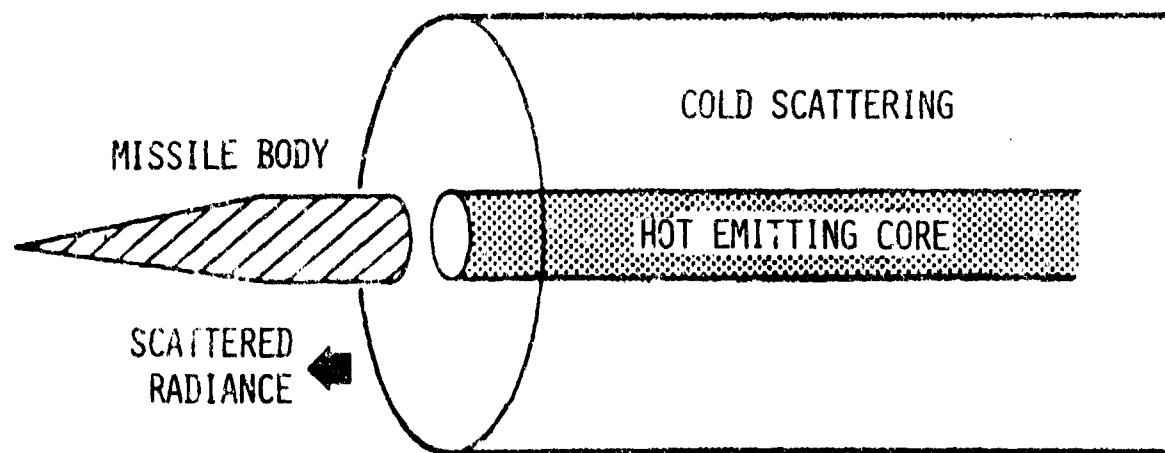
Figure 2-24. Core/Envelope Structure for
Nose Aspect Test Case.

2.7 Summary of Models and Results

The results discussed in Section 2.6 include calculations
for planar and cylindrical media using 6-flux, finite-difference,
and Monte Carlo solution techniques. The calculations include
the full range of optical parameters [albedo (0 to 1), optical
depth (.1 to 10), phase function (isotropic to delta function)]
and observables (transmissivity, reflectivity, emissivity;
radiance and station radiation versus position and aspect). The
results demonstrate the importance of three-dimensional multiple-
scattering effects and the relative ability of different
physical models to provide an accurate simulation.

Three new models were developed and verified in this phase
of the effort. The first was an explicit six-flux model which
is exact (for six-flux phase functions) for planar media and
approximate for cylindrical media. The second was an implicit
six-flux model which is exact (for six-flux phase functions) for
cylindrical media. The third was an implicit multiple-flux
("N-flux") model which is exact (for arbitrary phase functions)
for cylindrical media. The six-flux models provide the minimum
angular resolution necessary to account for three-dimensional
scattering effects. As such, they constitute valid engineering
approximations which are highly efficient for production calcu-
lations. The N-flux model provides complete flexibility in the
selection of angular resolution (elevation and azimuth). As a
result, alternate levels of resolution can be tested and compared
with respect to accuracy and efficiency.

2-77

The six-flux models are distinguished principally by the degree of rigor in treating side-scattering effects. That is, Method I approximates these effects via simple closure relations whereas Method II computes these effects via exact coupling equations. Both methods solve initially for the normal and tangential radiances and subsequently for the radiance at arbitrary aspect (if required). The fundamental difference is associated with the initial solution step.

To the authors' knowledge, the N-flux model represents the first application of general finite-element techniques to emitting cylindrical media. Previous application of this technique was to non-emitting planar media (Barkstrom, 1976). The information content of the calculation is considerable. For each radial station, the model predicts the complete three-dimensional radiance distribution in spherical coordinates. Typical results for two uniform isotropically scattering cylinders of different optical depth are illustrated in Figure 2-25. The figure shows polar plots in azimuth and elevation of the local radiance distribution at a series of radial stations from the center of each cylinder to the edge. In each case, the radiance are normalized by the edge value for a centered line-of-sight at side aspect ($\Theta=\phi=\pi/2$). In the azimuth plane, the radiance distribution is observed to be isotropic at the center and to evolve toward a forward lobe at the edge. In the elevation plane, the radiance distribution is roughly eliptic at the center.
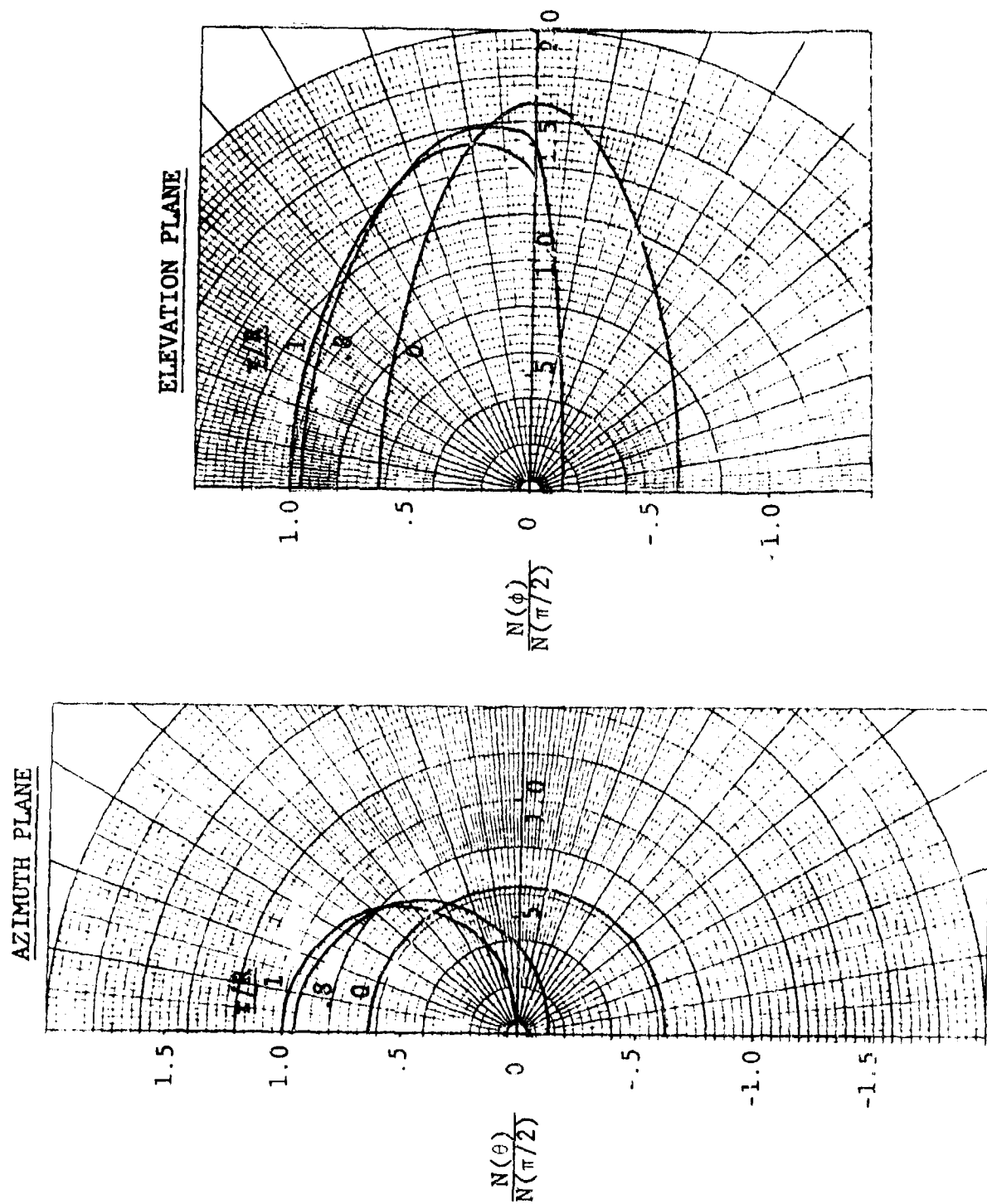
ELEVATION PLANE

$$\frac{N(\phi)}{N(\pi/2)}$$

AZIMUTH PLANE

$$\frac{N(\theta)}{N(\pi/2)}$$

Figure 2-25a. Radiance Distributions in Azimuth and Elevation (N-Flux Model; Isotropic Scattering; $\tau=1.0$, $\omega=0.8$)

2-79

ELEVATION PLANE
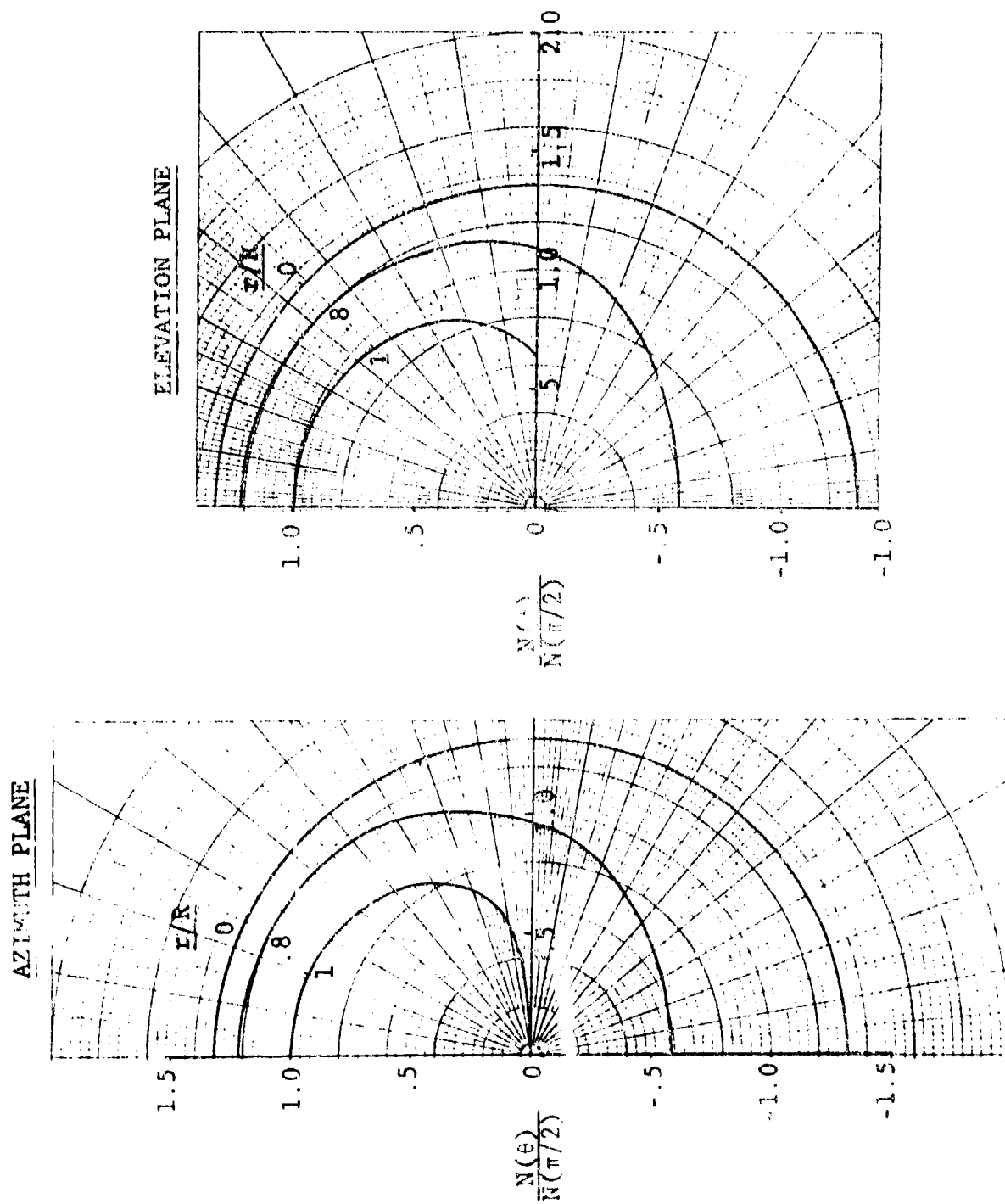
$\frac{r/R}{1.0}$ .8 1 .5 1.0 1.5 2.0 .5 1.0 -1.0

$\frac{N()}{N(\pi/2)}$

AZIMUTH PLANE

$\frac{r/R}{0}$ .8 1 .5 1.0 1.5 1.0 .5 -1.0 -1.5

$\frac{N(\theta)}{N(\pi/2)}$

Figure 2-25b.   diance Distributions in Azimuth and Elevation
-Flux Model: isotropic Scattering: τ=10.; ω=0.8)

(approaching isotropic for large optical depths) and evolves toward a composite forward/side lobe at the edge. The radiances are observed to increase or decrease from the center to the edge for small or large optical depths, respectively, with the maximum rate of change occuring near the surface. This result may be compared to a non-scattering medium in which the radiance always increases monotonically outward.

The N-flux model provides a powerful tool for the analysis of plume scattering problems of arbitrary complexity. The accuracy of the prediction is limited only by the computational resources of the user. Because of the significant cost implications of repetitive calculations for multiple spectral points, an important aspect of the continuing effort is the optimization of the mathematical procedures and the grid selection (spatial and angular). Mathematical optimization includes the selection of iterative or inversion procedures for small or large scattering optical depth ($\omega\tau$) and the use of a different (finer) radial grid for evaluation of the emission/extinction terms. Grid optimization involves the correlation of accuracy and efficiency with both the number of elements (radius and aspect) and the positions of their boundaries.

A rough preliminary indication of the degree of resolution required for a given accuracy is shown in Figure 2-26. This figure is representative of the limited computational experience
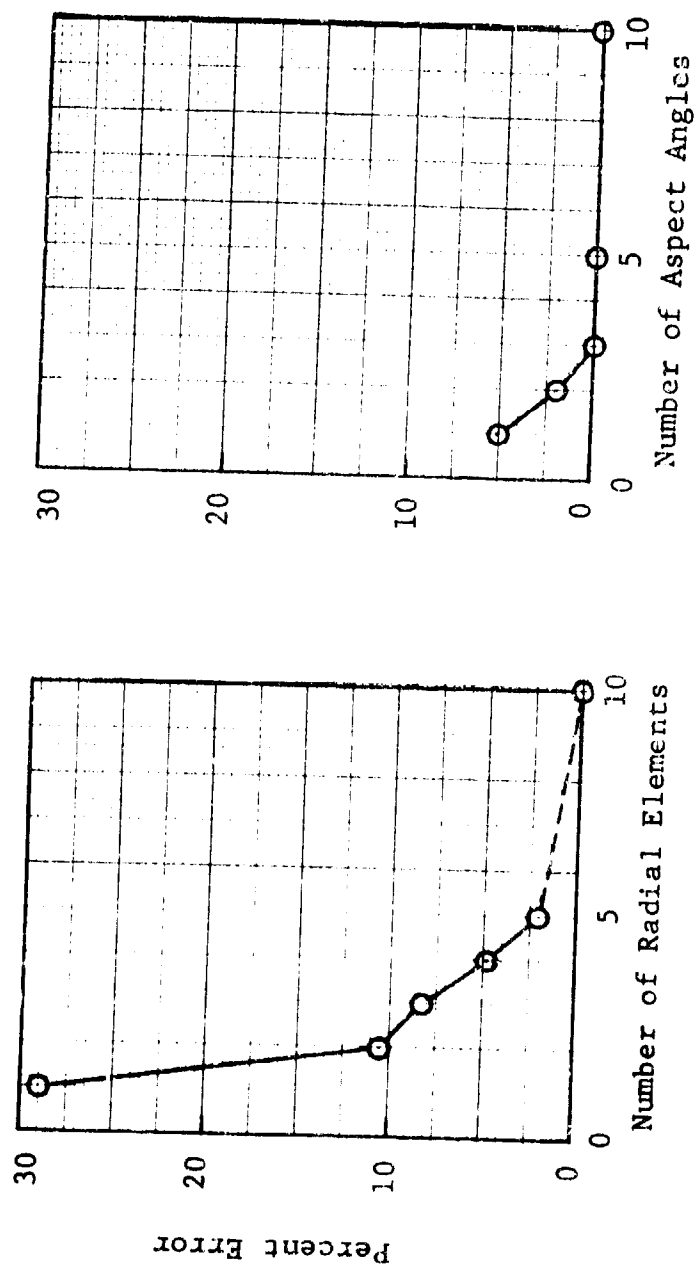
Figure 2-26. Accuracy versus Resolution for N-Flux Model ($\tau=10$; $\omega=.8$)

acquired to date but does not necessarily possess broader quan-
titative applicability. The results shown are for an optically
thick uniform cylinder with isotropic scattering (τ=10, ω=.8).
No particular effort was made to optimize the grid selection for
a given number of points. The accuracy is observed to be much
more sensitive to the number of radial elements than to the
number of aspect angles.

By far the largest portion of the computing time is in the
calculation of the source functions. As a result, CPU time is
roughly proportional to the square of the number of aspect
angles ($\phi_j \phi_j$') and to the cube of the number of radial segments
(r_k, Θ_i, Θ_i'). Thus, doubling both the number of aspect angles and
the number of radial segments results in a computing time increase
of about a factor of 30. Optimization of the selection of these
numbers is, therefore, of considerable importance for production
calculations.

Figure 2-27 summarizes the parametric and comparative cal-
culations performed to date as reported in Sections 2.6 and 2.7.
This summary illustrates the interrelationships among the various
techniques and the scope of physical problems considered. The
emphasis in this phase of the study was on model development
and verification. Additional work is required in the areas of
model optimization and application. In particular, final quan-
titative assessment of the relative accuracy and efficiency of
the different calculation methods in different physical situa-
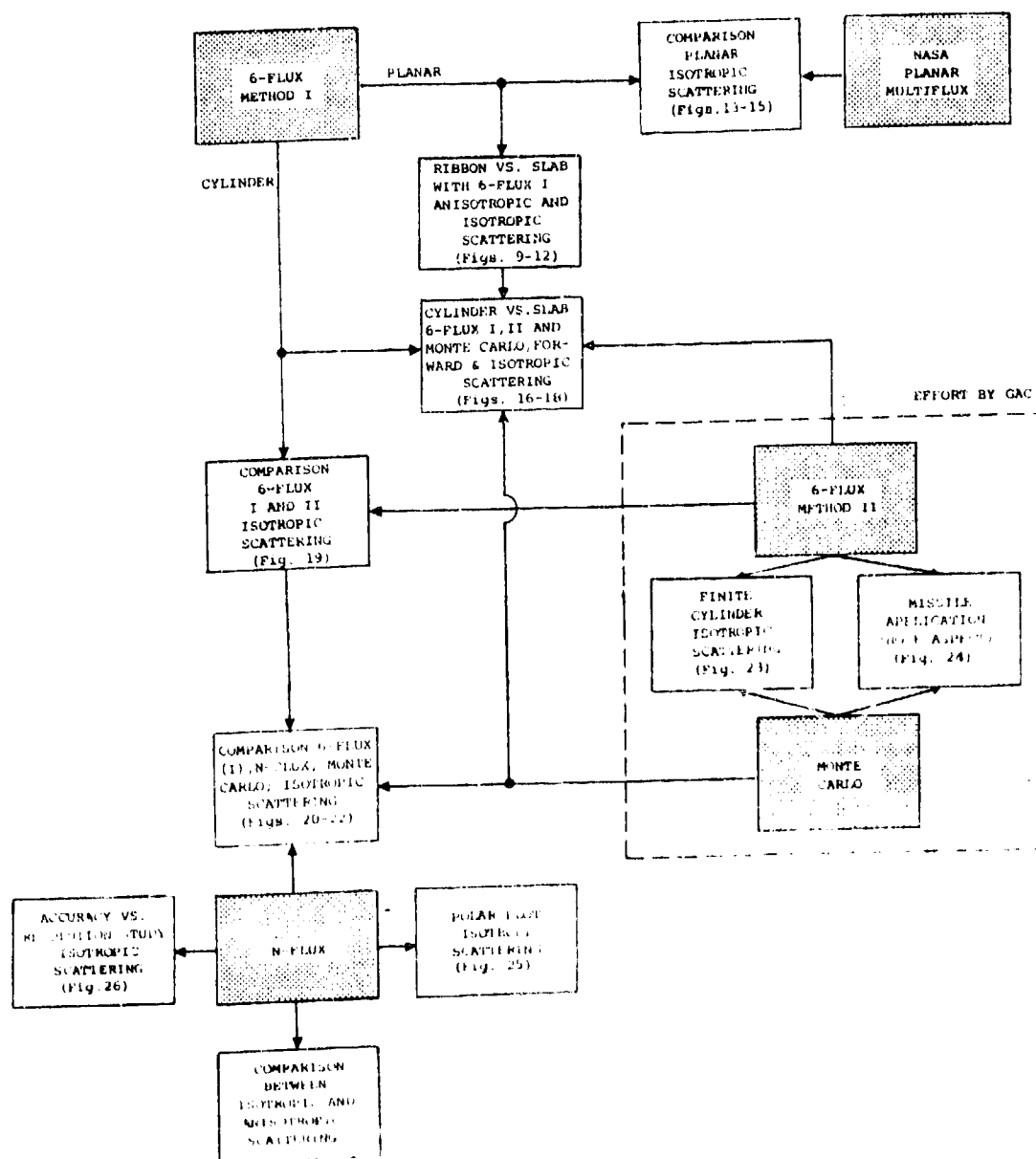tions must necessarily await further model refinements and

Figure 2-27. Overview of Parametric and Comparative
Calculations Presented in Subsections
2.6 and 2.7.

additional parametric predictions. These efforts are currently underway. However, based on the parametric and comparative calculations performed to date, certain general conclusions can be drawn:

1)   The six-flux angular quadrature (Method I or II) yields quantitatively accurate predictions for normal and tangent aspect in the cases of intermediate-to-large optical depth or anisotropic scattering. The standards for comparison are the NASA finite-element code for slabs and the N-Flux and Monte-Carlo codes for cylinders.

2)   The six-flux angular quadrature (Method I or II) tends to overpredict the normal and tangent radiation for isotropic scattering at small optical depths. The error is greatest for slabs and least for ribbons due to the corrective effect of side-scattering losses. For cylindrical plume geometries, the error appears to be acceptable (less than 20 percent).

3)   The aspect dependence predicted by the six-flux methods is based on prior solution for normal and tangent aspect. For intermediate aspect angles, simple interpolation (Method I) gave the correct qualitative behavior, but overestimated the sensitivity to albedo by comparison to the N-flux model. Line-of-sight integration (Method II) gave the correct quantitative behavior by comparison to limited Monte Carlo calculations for intermediate optical depth.

4)   The N-Flux and Monte Carlo calculations demonstrated uniformly excellent agreement for all cases investigated.

3

BAND MODEL APPROACHES

3.1 Introduction

The equation of radiative transfer, which is rigorous on a monochromatic basis, is only approximate when applied over a finite spectral interval. The spectral averaging procedures required for the calculation of radiant transfer in a multiple scattering medium must be considered.

The integral form of the equation of transfer for a finite spectral interval $\Delta\lambda$ may be written

$$\bar{N}_\lambda(\vec{s}) = \int_{s_o}^{s} \left[N_\lambda^o(s') \left(\overline{\frac{dT_\lambda(s',s)}{ds'}} - \omega_\lambda \overline{\frac{dT_\lambda(s',s)}{ds'}} \right) \right.$$

$$\left. + \frac{1}{4\pi} \int_{4\pi} P_\lambda(\vec{s}'',\vec{s}') \overline{\omega_\lambda N_\lambda(\vec{s}'') \frac{dT_\lambda(s',s)}{ds'}} \, d\Omega(\vec{s}'') \right] \cdot ds'$$

where a spectrally averaged quantity $\bar{x}$ is defined as

$$\bar{x}_\lambda \equiv \frac{1}{\Delta\lambda} \int_{\Delta\lambda} x_\lambda d\lambda$$

and where the relatively small spectral variations of N_λ^o and P_λ within $\Delta\lambda$ are neglected. The integrand contains three spectrally-averaged terms involving the transmittance derivative and its

product with the albedo and radiance. Of these terms, only the transmittance derivative is amenable to simple averaging through superposition of the individual species averages. Evaluation of the product terms requires additional approximations which are investigated in this section. The goal of this investigation is to develop as comprehensive a band model theory of combined scattering and gaseous absorption as possible and to determine the functional dependence of the mean transmissivity and emissivity on the gaseous band model and particle scattering parameters as a guide to their most reasonable combination in the more general three-dimensional numerical solutions of the radiative transfer equation.

In developing a combined absorption-scattering band model formalism, the approach has been used which is analogous to that of the classical gaseous band-model theory, namely, from a monochromatic solution of the radiative transfer equation, to perform a spectral integration over a defined gaseous absorption band, making approximations as required to obtain a closed form solution (and studying the limitations on the accuracy of the solution imposed by the required approximations).

3.2. Band Model Formulation For One-Dimensional Scattering

A starting point has been selected to be the "one-dimensional" (i.e., two-flux) scattering formalism of Vanderbilt and Slack (1976), which has the advantage of having been developed to the state in which various closed-form solutions exist which are explicit in certain limiting cases.

It is important to note that the two-flux and six-flux ap-
proaches to the problem of radiation from a plane-parallel slab
yield similar functional forms, differing only in the definitions
of the effective backward and forward scattering cross sections.
Thus, the so-called "one-dimensional" scattering solution is
capable of reproducing the effects of three-dimensional scattering
in this particular case.

It is noted also that the condition of completely anisotropic
scattering which is sometimes evoked as justification for applica-
tion of the one-dimensional formalism is a sufficient condition,
but by no means a necessary condition for its applicability.
Because of its relative mathematical simplicity (in addition to
the fact that the previously mentioned sufficient condition for
its validity, i.e., the assumption of complete anisotropy, is
very closely approached in many real scattering problems),
this formalism will always be of great value in a large number
of practical situations.

We start with one approximate solution of the two-flux
scattering equation, which is exact in a limiting case and which
provides an iterative solution under more general conditions
(Vanderbilt and Slack, 1976):

$$I^-(0) = \chi_0^{\frac{1}{2}} \frac{(\chi_m^{\frac{1}{2}}+1)e^{W_m}\int_0^{W_m}\frac{2B}{\chi^{\frac{1}{2}}}e^{-W'}dW' - (\chi_m^{\frac{1}{2}}-1)e^{-W_m}\int_0^{W_m}\frac{2B}{\chi^{\frac{1}{2}}}e^{W'}dW'}{(\chi_m^{\frac{1}{2}}+1)(\chi_0^{\frac{1}{2}}+1)e^{W_m} - (\chi_m^{\frac{1}{2}}-1)(\chi_0^{\frac{1}{2}}-1)e^{-W_m}} \quad (3-1)$$

where

$$W = \int_0^s N\sigma_a \chi^{\frac{1}{2}} ds' \qquad (3\text{-}2)$$

and

$$\chi^{\frac{1}{2}} = \left\{1 + \frac{2\sigma_{sb}}{\sigma_a}\right\}^{\frac{1}{2}} = \left\{1 + \frac{2\beta\omega}{1-\omega}\right\}^{\frac{1}{2}} \qquad (3\text{-}3)$$

In these equations, N is the particle density, σ_a the absorption cross section and σ_{sb} the backscattering cross section, and β is the ratio of backscattering to total scattering. For simplicity, the absorption and scattering cross sections are referenced to a single particle density; however, for mixtures of particles or particles plus gases, the expressions are readily generalized.

For the case of constant χ, an exact solution is provided for an otherwise inhomogeneous path, i.e.,

$$I^-(0) = \frac{\frac{2}{\chi^{\frac{1}{2}}+1}\left[\int_0^{W_m} Be^{-W'} dW' - \frac{\chi^{\frac{1}{2}}-1}{\chi^{\frac{1}{2}}+1} e^{-2W_m}\int_0^{W_m} Be^{W'} dW'\right]}{1 - \left(\frac{\chi^{\frac{1}{2}}-1}{\chi^{\frac{1}{2}}+1}\right)^2 e^{-2W_m}} \qquad (3\text{-}4)$$

where

$$W_m = \chi^{\frac{1}{2}}\tau_a \ . \qquad (3\text{-}5)$$

The absorption optical depth is denoted by τ_a, which may represent the sum of contributions from a number of gaseous and particulate species.

For the isothermal case, direct integration provides (on division by the Planck blackbody function) the known expression for emissivity:

$$\varepsilon = \frac{I^-(0)}{B} = \frac{\dfrac{2}{\chi^{\frac{1}{2}}+1}\left[\left(1-e^{-\chi^{\frac{1}{2}}\tau_a}\right) - \dfrac{\chi^{\frac{1}{2}}-1}{\chi^{\frac{1}{2}}+1}\left(e^{-\chi^{\frac{1}{2}}\tau_a} - e^{-2\chi^{\frac{1}{2}}\tau_a}\right)\right]}{1-\left(\dfrac{\chi^{\frac{1}{2}}-1}{\chi^{\frac{1}{2}}+1}\right)^2 e^{-2\chi^{\frac{1}{2}}\tau_a}} \qquad (3\text{-}6)$$

On factoring and rearranging into a form more suitable for our purposes, we obtain

$$\varepsilon = \frac{1-e^{-\chi^{\frac{1}{2}}\tau_a}}{1 + \dfrac{1}{2}\left(\chi^{\frac{1}{2}}-1\right)\left(1+e^{-\chi^{\frac{1}{2}}\tau_a}\right)} \qquad (3\text{-}7)$$

Briefly considering the limit of small $\beta\omega$ ($\chi \approx 1$), we obtain a somewhat more transparent form

$$\varepsilon \approx \frac{1-e^{-\tau_s-\tau_a}}{1+\dfrac{1}{2}\dfrac{\beta\omega}{1-\omega}\left(1+e^{-\tau_s-\tau_a}\right)} \qquad (3\text{-}8)$$

Because of the relatively small variation of the denominator from unity, the mean value over a spectral interval can be written as

3-5

$$\bar{\epsilon} \;=\; \frac{1}{\Delta\omega}\int_{\Delta\omega}\epsilon\,d\omega \;\approx\; \frac{1-e^{-\tau_s}e^{-f(\bar{\tau}_a)}}{1+\frac{1}{2}\left(\frac{\overline{\beta\omega}}{1-\omega}\right)\left(1+e^{-\tau_s}e^{-f(\bar{\tau}_a)}\right)} \tag{3-9}$$

where

$$f(\bar{\tau}_a) \;=\; -\ell n\left\{\frac{1}{\Delta\omega}\int_{\Delta\omega}e^{-\tau_a}d\omega\right\} \tag{3-10}$$

represents the band-model curve-of-growth for the gas plus par-
ticle absorption component (that is, a known function). Equation
(3-9) explicitly shows the modifications resulting from the
simultaneous presence of scattering.

For χ significantly greater than unity, it still appears rea-
sonable to consider the preponderant effect of spectral variation
to occur in the numerator (which varies from unity to zero).
The percentage error introduced by this assumption will be in-
vestigated in the numerical studies in Subtask II. We write

$$\bar{\epsilon} \;\approx\; \frac{1-e^{-f(\bar{\tau}_a,\tau_s)}}{1+\frac{1}{2}\left[(\bar{\chi})^{\frac{1}{2}}-1\right]\left(1+e^{-f(\bar{\tau}_a,\tau_s)}\right)} \tag{3-11}$$

where

$$f(\bar{\tau}_a,\tau_s) \;=\; -\ell n\left\{\frac{1}{\Delta\omega}\int_{\Delta\omega}e^{-(\tau_a^2+2\tau_a\tau_s)^{\frac{1}{2}}}d\omega\right\} \tag{3-12}$$

represents a band model curve of growth including scattering.
We designate the numerator of Eq.(3-11) as 1-t' (since it

3-6

corresponds to the emissivity = 1-transmissivity in the

non-scattering limit)

3.2.1 Elsasser model. We examine the behavior of the function $\bar{t}'$ when the absorption results from one gaseous component represented by the Elsasser model (for which case the effects of the gaseous spectral structure will be the greatest):

$$\tau_a = \bar{\tau}_a \frac{\sinh \beta}{\cosh\beta - \cos x} \qquad (3\text{-}13)$$

where

$$\bar{\tau}_a = \bar{k}u = Su/d \qquad (3\text{-}14)$$
(mean absorption optical depth)

$$\beta = 2\pi \gamma/d \qquad (3\text{-}15)$$
(fine-structure parameter)

and

$$x = 2\pi(\omega-\omega_o)/d . \qquad (3\text{-}16)$$

Thus

$$\bar{t}' = \frac{1}{\pi} \int_0^{\pi} \exp\left[-\left(\bar{\tau}_a^2 \frac{\tanh^2\beta}{(1-\cos x/\cosh\beta)^2}\right. \right.$$

$$\left. \left. + 2\bar{\tau}_a\tau_s \frac{\tanh\beta}{(1-\cos x/\cosh\beta)}\right)^{\frac{1}{2}}\right]dx \qquad (3\text{-}17)$$

The properties of this integral will be examined in detail for the limiting cases of small β and large β.

For large values of the parameter β (i.e., for significant overlapping of the spectral lines), the function $\bar{t}'$ becomes (on expansion of the terms in $1-\cos x/\cosh\beta$),

$$\bar{t}' = \exp\left[-(\bar{\tau}_a{}^2\tanh^2\beta+2\bar{\tau}_a\tau_s\tanh\beta)^{\frac{1}{2}}\right]$$
$$\times I_0\left[(\bar{\tau}_a{}^2\tanh^2\beta+2\bar{\tau}_a\tau_s\tanh\beta)^{\frac{1}{2}}\left(\frac{\bar{\tau}_a\tanh\beta+\tau_s}{\bar{\tau}_a\tanh\beta+2\tau_s}\right)/\cosh\beta\right]$$

(3-18)

where I_0 is the modified Bessel function of the first kind. Since $\exp(-x)\approx 1-x$ for small x, and $I_0(y)\approx 1+\frac{1}{4}y^2$ for small y (and $y \ll x$), the I_0 term provides a higher-order correction to the exponential term. Thus a useful approximation is

$$\bar{t}' = \exp\left[-(\bar{\tau}_a{}^2\tanh^2\beta+2\bar{\tau}_a\tau_s\tanh)^{\frac{1}{2}}\right]$$

(3-19)

Note that for no scattering ($\tau_s \equiv 0$), we have

$$\bar{t} = 1-\bar{\epsilon} = \bar{t}' = \exp(-\bar{\tau}_a\tanh\beta),$$

(3-20)

the classical Elsasser model result.

For the more interesting case of β small (little over-lapping of spectral lines), we have (using $\cosh\beta \approx 1$)

3-8

$$\left(\bar{\tau}_a^2 + 2\bar{\tau}_a\tau_s\right)^{\frac{1}{2}} = \bar{\tau}_a\left(\frac{\sinh^2\beta}{(1-\cos x)^2} + \frac{2\tau_s}{\bar{\tau}_a}\frac{\sinh\beta}{(1-\cos x)}\right)^{\frac{1}{2}}$$

$$= \left(\bar{\tau}_a^2\frac{\sinh^2\beta}{4\sin^4 x/2} + \bar{\tau}_a\tau_s\frac{\sinh\beta}{\sin^2 x/2}\right)^{\frac{1}{2}} \tag{3-21}$$

$$= \left(\frac{b}{\sin^4 y} + \frac{a}{\sin^2 y}\right)^{\frac{1}{2}}$$

where

$$a = \bar{\tau}_a\tau_s\sinh\beta \tag{3-22}$$

$$b = \frac{1}{4}\bar{\tau}_a^2\sinh^2\beta \tag{3-23}$$

and

$$y = \frac{1}{2}x$$

By making the substitution

$$(a+b)^{\frac{1}{2}}z = \left(\frac{a}{\sin^2 y} + \frac{b}{\sin^4 y}\right)^{\frac{1}{2}}$$

to transform to a more standard form (e.g., that of a Laplace transform), the function

$$\bar{t}' = \frac{2}{\pi}\int_0^{\pi/2}\exp\left[-\left(\frac{a}{\sin^2 y} + \frac{b}{\sin^4 y}\right)^{\frac{1}{2}}\right]dy \tag{3-24}$$

becomes

$$\bar{t}' = -\frac{2}{\pi} \int_1^\infty \exp\left[-(a+b)^{\frac{1}{2}}z\right]\left\{\frac{z}{\left[z^2 - \dfrac{a+(a^2+4b(a+b)z^2)^{\frac{1}{2}}}{2(a+b)}\right]^{\frac{1}{2}}}\right\}$$

$$\left\{\left[2(a+b)\right|^{\frac{1}{2}} b\left[a+(a^2+4b(a+b)z^2)^{\frac{1}{2}}\right]^{-\frac{1}{2}}(a^2+4b(a+b)z^2)^{-\frac{1}{2}}\right\} \quad (3\text{-}25)$$

$$- \frac{1}{\left|2(a+b)\right|^{\frac{1}{2}}z^2}\left|a+(a^2+4b(a+b)z^2)^{\frac{1}{2}}\right|^{\frac{1}{2}}\right\}dz \quad .$$

This form is somewhat unwieldy, and does not appear to be immediately integrable. For the limiting case $a = 0$ (no scattering), the expression above reduces to

$$\bar{t}' = \frac{1}{\pi} \int_1^\infty \exp(-\sqrt{b}z)\, \frac{1}{z(z-1)^{\frac{1}{2}}}\, dz \quad (3\text{-}26)$$

$$= \operatorname{erfc}(b^{\frac{1}{4}}) = \operatorname{erfc}\left|(\bar{\tau}_a\beta/2)^{\frac{1}{2}}\right| \quad , \quad (3\text{-}27)$$

the usual Elsasser model result for small β .

In the other limiting case of $b = 0$ (more strictly speaking, $b/a \to 0$) the integral for $\bar{t}'$ reduces to

$$\bar{t}' = \frac{2}{\pi} \int_1^\infty \exp(-a^{\frac{1}{2}}z)\, \frac{1}{z(z^2-1)^{\frac{1}{2}}}\, dz \quad . \quad (3\text{-}28)$$

This expression may be converted to a known Laplace transform, yielding

$$\bar{t}' = 1 - \frac{2}{\pi} \int_{0}^{a^{\frac{1}{2}}} K_0(x)\,dx \qquad (3\text{-}29)$$

where

$$a^{\frac{1}{2}} = (\bar{\tau}_a \tau_s \sinh\beta)^{\frac{1}{2}},$$

as before, and $K_0(x)$ is the modified Bessel function of the second kind. Such functions (of integral order) appear to be the least tractable of the Bessel functions. However, since $K_0(x)$ is only weakly (logarithmically) divergent at the origin, series expressions may be used and integrated over the finite interval indicated.

Because of the mathematical intractability of this Bessel function, a numerical study was made of $\bar{t}'$. From the power series definition of K_0, and a term-by-term integration of Equation (3-29) we obtain

$$\int_{0}^{z} K_0(x)\,dx = \sum_{k=0}^{\infty} \left[-b_k \left(\ell n(\tfrac{1}{2}z) + \gamma \right) + c_k \right] \left(\frac{2}{2k+1} \right) (\tfrac{1}{2}z)^{2k+1} \qquad (3\text{-}30)$$

where $\gamma = .5772156649...,$ (Euler's constant)

$$b_k = \frac{1}{(k!)^2} ,$$

$$a_k = \frac{1}{(k!)^2} \sum_{i=1}^{k} \left(\frac{1}{i}\right) ,$$

$$c_k = a_k + \frac{1}{2k+1} b_k .$$

$$\left. \right\} (3\text{-}31)$$

By use of recursion relations between the coefficients, the series is readily programmable, with high accuracy, even on a pocket calculator, for values of z as large as 12. However, for z greater than about 8, higher accuracy may be achieved by an asymptotic series. By expanding the exponential in a power series and integrating, the following expressions are obtained

$$\bar{t}' = \sqrt{\frac{2}{\pi}} \exp(-a^{\frac{1}{2}}) \sum_{j=o}^{\infty} (-1)^j d_j a^{-\frac{1}{2}(j+\frac{1}{2})} , \qquad (3\text{-}32)$$

where

$$d_j = \sum_{i=o}^{j} \left(\frac{1 \cdot 3 \cdot 5 \cdot \ldots (2i-1)}{i! \, 2^{2i}}\right) \left(1 \cdot \frac{1}{2} \cdot \frac{3}{2} \cdot \ldots \frac{2j-1}{2}\right) . \qquad (3\text{-}33)$$

This series is "semi-convergent" and must be truncated when the magnitude of the terms no longer decreases. For $a^{\frac{1}{2}}$ greater than about 8, it is capable of providing 3-place accuracy for $\bar{t}'$ deteriorates; for $a \approx 1$, it is effectively worthless.

The function $t' = 1 - \frac{2}{\pi} \int_{0}^{a^{\frac{1}{2}}} K_o(x)\,dx$ is plotted in Figure 3-1 in Cartesian coordinates and the curve-of-growth $-\ln \bar{t}'$ is plotted versus $a^{\frac{1}{2}}$ (log-log scale) over a much wider range of values of $a^{\frac{1}{2}}$ in Figure 3-2.
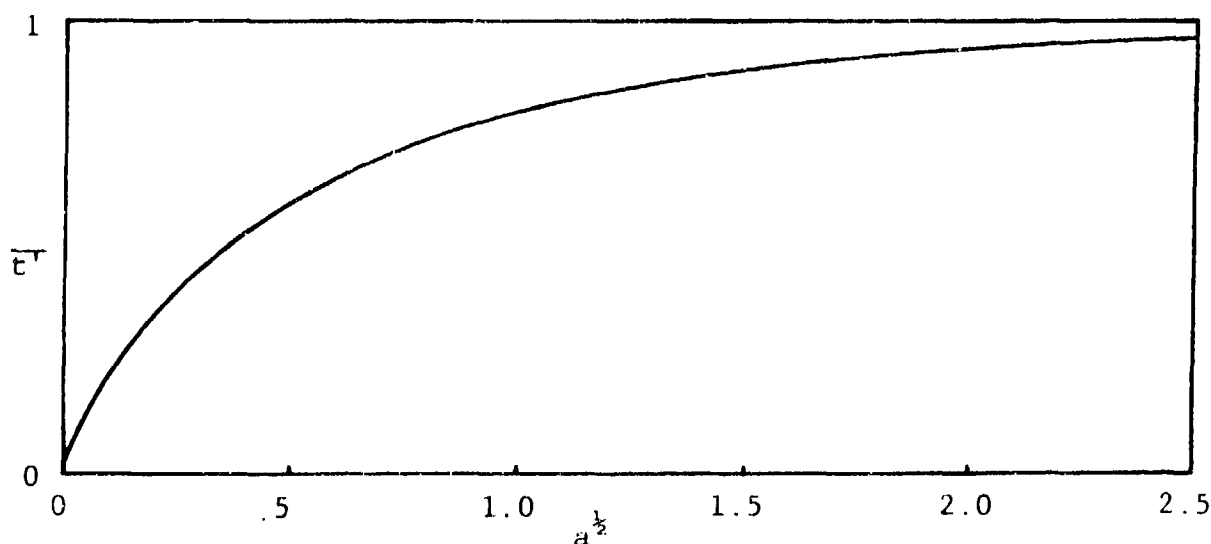
Figure 3-1. Function $\bar{t}' = 1 - \frac{2}{\pi} \int_{0}^{a^{\frac{1}{2}}} K_o(x)\,dx$ vs. $a^{\frac{1}{2}}$.
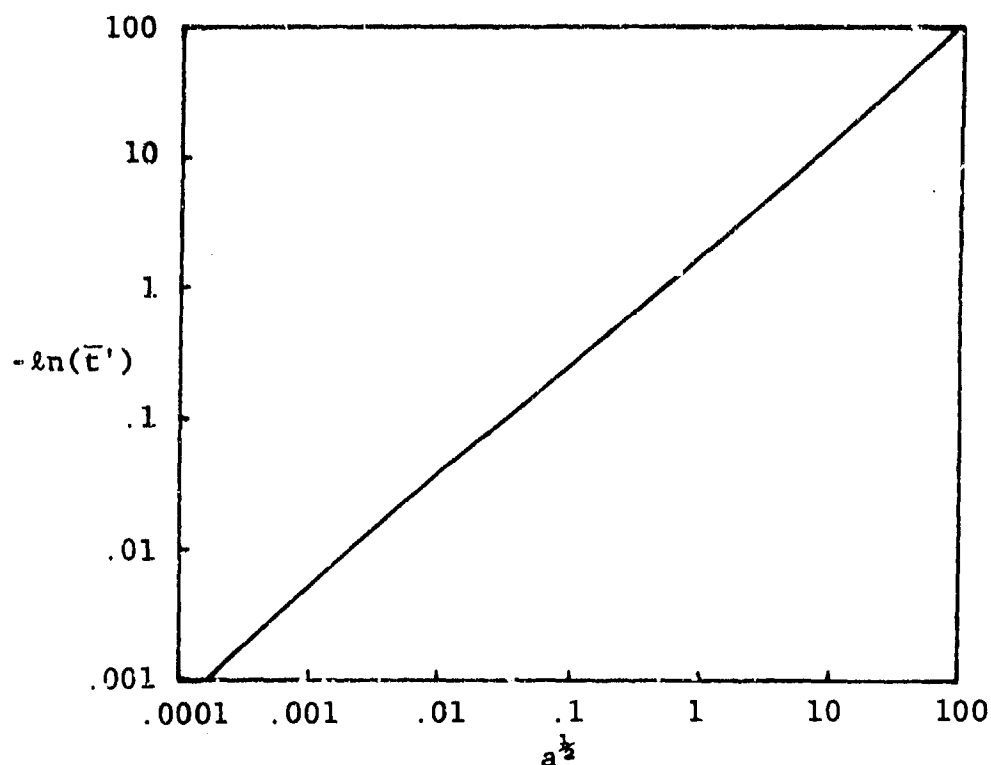
Figure 3-2. Curve-of-Growth $-\ln(\bar{t}')$ versus $a^{\frac{1}{2}}$ for

$$\bar{t}' = 1 - \frac{2}{\pi} \int_{0}^{a^{\frac{1}{2}}} K_{0}(x) \, dx .$$

3.2.2 Random band models: The mean trasnmissivity for a given band model may be written alternatively

$$\bar{t} \left[= \frac{1}{\Delta\omega} \int_{\Delta\omega} t\,(k(\omega))\,d\omega \right] = \int_{0}^{\infty} f(k)\,t\,(k)\,dk, \qquad (3\text{-}34)$$

in which $f(k)$ is the probability density function of the absorption coefficient k . Because the properties of random band models without scattering are relatively simply derivable from those of single lines, explicit expressions for such probability densities have not been required for study of the

3-14

gaseous band models. However, because of the exponential form of the monochromatic transmissivity, the probability density function in the expression

$$\bar{t}(u) = \int_0^\infty f(k)e^{-ku} \, dk \qquad (3-35)$$

can be seen to be the inverse Laplace transform of the mean transmissivity function. A study of the inverse Laplace transforms of known transmissivity functions has been made by Domoto (1974), who has found that for the exponential-tailed S^{-1} model a relatively simple functional form exists, namely,

$$f(k) = \left[\frac{\bar{k} \, a}{\pi \, k^3}\right]^{\frac{1}{2}} \exp\left[a\left(2 - \frac{k}{\bar{k}} - \frac{\bar{k}}{k}\right)\right] \qquad , \qquad (3-36)$$

corresponding to the transmissivity function

$$\bar{t}(u) = \exp\left\{- 2a\left[\left(1 + \frac{\bar{k} \, u}{a}\right)^{\frac{1}{2}} - 1\right]\right\} \qquad . \qquad (3-37)$$

We consider here the case of no particulate absorption, for which the effects of the gaseous spectral structure will be the greatest. The function $\bar{t}'$ previously defined as

$$\bar{t}' = \frac{1}{\Delta\omega} \int_{\Delta\omega} \exp\left[- (\tau_a^2 + 2\tau_a\tau_s)^{\frac{1}{2}}\right] d\omega \qquad (3-38)$$

(where $\tau_a = ku$) can be rewritten

$$\bar{t}' = \int_0^\infty \left[\frac{\bar{\tau}_a \, a}{\pi \, \tau_a^3}\right]^{\frac{1}{2}} \exp\left[a\left(2 - \frac{\tau_a}{\bar{\tau}_a} - \frac{\bar{\tau}_a}{\tau_a}\right) - \left(\tau_a^2 + 2\tau_a\tau_s\right)^{\frac{1}{2}}\right] d\tau_a \qquad (3-39)$$

3-15

Direct integration is rendered difficult by the presence of the radical in the exponential term. Before studying the general behavior of $\bar{t}'$, some limiting cases (small τ_s, large τ_s) are examined.

a) *Small τ_s*

For small values of τ_s ($\tau_s \ll \bar{\tau}_a$), expansion of the radical yields

$$(\tau_a^2 + 2\tau_a\tau_s)^{\frac{1}{2}} \approx \tau_a + \tau_s - \frac{1}{2}\frac{\tau_s^2}{\tau_a} \ldots , \tag{3-40}$$

in which terms in τ_s^3/τ_a^2 etc. have been suppressed. Substitution produces

$$\bar{t}' = \int_0^\infty \left(\frac{\bar{\tau}_a\, a}{\pi\,\tau_a^3}\right)^{\frac{1}{2}} \exp\left[2a - \tau_s - \left(\frac{a}{\bar{\tau}_a} + 1\right)\tau_a - \left(a\bar{\tau}_a - \tfrac{1}{2}\tau_s^2\right)\tau_a^{-1}\right] d\tau_a , \tag{3-41}$$

or, defining

$$a^* = a\left(1 - \frac{\tau_s^2}{2a\bar{\tau}_a}\right)^{\frac{1}{2}} , \tag{3-42}$$

and

$$\bar{\tau}_a^* = \bar{\tau}_a\left(1 - \frac{\tau_s^2}{2a\bar{\tau}_a}\right)^{\frac{1}{2}} , \tag{3-43}$$

$$\bar{t}' = e^{-\tau_s}\left(1 - \frac{\tau_s^2}{2a\bar{\tau}_a}\right)^{-\frac{1}{2}} \int_0^\infty \left(\frac{\bar{\tau}_a^* a^*}{\pi\,\tau_a^3}\right)^{\frac{1}{2}} \exp\left[2a - \left(\frac{a^*}{\bar{\tau}_a^*} + 1\right)\tau_a - \frac{a^*\bar{\tau}_a^*}{\tau_a}\right] d\tau_a \tag{3-44}$$

Since the integral is now in the standard form with new constants, we have

$$\bar{t}' = e^{-\tau_s}\left(1 - \frac{\tau_s^2}{2a\bar{\tau}_a}\right)^{-\frac{1}{2}} \exp\left\{-2a^*\left[\left(1 + \frac{\bar{\tau}_a^*}{a^*}\right)^{\frac{1}{2}} - 1\right]\right\} \tag{3-45}$$

3-16

or

$$\bar{t}' = e^{-\tau_s}\left(1 - \frac{\tau_s^2}{2a\bar{\tau}_a}\right)^{-\frac{1}{2}} \exp\left\{-2a\left(1 - \frac{\tau_s^2}{2a\bar{\tau}_a}\right)^{\frac{1}{2}}\left[\left(1 + \frac{\bar{\tau}_a}{a}\right)^{\frac{1}{2}} - 1\right]\right\} \quad . \tag{3-46}$$

To the same degree of approximation we may write

$$\bar{t}' = \exp\left\{-2a\left(1 - \frac{\tau_s^2}{2a\bar{\tau}_a}\right)^{\frac{1}{2}}\left[\left(1 + \frac{\bar{\tau}_a}{a}\right)^{\frac{1}{2}} - 1\right] - \tau_s + \frac{\tau_s^2}{4a\bar{\tau}_a}\right\} \quad . \tag{3-47}$$

b)   _Large τ_s_

In the limit of large τ_s the magnitude of the argument of the exponential term in the integral becomes large, and the minimum progressively less shallow, and occurring at smaller values of τ_a . If $\tau_s \gg \tau_a$, so that

$$(\tau_a^2 + 2\tau_a\tau_s)^{\frac{1}{2}} \approx (2\tau_a\tau_s)^{\frac{1}{2}} \quad , \tag{3-48}$$

the argument of the exponential term becomes

$$E(\tau_a) = -a\,\frac{\bar{\tau}_a}{\tau_a}\left(1 - \frac{\tau_a}{\bar{\tau}_a}\right)^2 - \left(2\tau_a\tau_s\right)^{\frac{1}{2}} \quad . \tag{3-49}$$

The magnitude of this argument has a minimum at approximately

$$\tau_a^{\min} \approx (\tau_s/2)^{-\frac{1}{3}}(a\bar{\tau}_a)^{\frac{2}{3}} \quad , \tag{3-50}$$

so that for large τ_s, $\tau_a^{\min} \ll \bar{\tau}_a$.

In the region of this minimum, the argument may be expanded:

$$E(\tau_a) \approx -3(\tfrac{1}{2}a\bar{\tau}_a\tau_s)^{1/3}$$

$$-\frac{3}{4}\left(\frac{\tau_s}{2a\bar{\tau}_a}\right)\left(\tau_a - \tau_a^{min}\right)^2 + \ldots \qquad . \qquad (3\text{-}51)$$

the expression for $\bar{t}'$ then becomes

$$\bar{t}' = \int_0^\infty \left(\frac{\bar{\tau}_a\, a}{\pi\ \tau_a^3}\right)^{\frac{1}{2}} \exp\left[-3(\tfrac{1}{2}a\bar{\tau}_a\tau_s)^{\frac{1}{3}} - \frac{3}{4}\left(\frac{\tau_s}{2a\bar{\tau}_a}\right)\left(\tau_a - \tau_a^{min}\right)^2\right] d\tau_a \quad . \qquad (3\text{-}52)$$

By recourse to the mean value theorem, noting the narrowness of the maximum of the exponential in the neighborhood of τ_a^{min}, the multiplicative factor of $\tau_a^{-3/2}$ may be taken outside the integral and evaluated at τ_a^{min}:

$$\bar{t}' \approx \left(\frac{\bar{\tau}_a\, a}{\pi\, (\tau_a^{min})^3}\right)^{\frac{1}{2}} \exp\left[-3(\tfrac{1}{2}a\bar{\tau}_a\tau_s)^{\frac{1}{3}}\right] \int_0^\infty \exp\left[-\frac{3}{4}\left(\frac{\tau_s}{2a\bar{\tau}_a}\right)\left(\tau_a - \tau_a^{min}\right)^2\right] d\tau_a \cdot \qquad (3\text{-}53)$$

The remaining integration may be performed by letting the lower bound $\to -\infty$:

$$\bar{t}' \approx \sqrt{\frac{4}{3}}\ \exp\left[-3(\tfrac{1}{2}a\bar{\tau}_a\tau_s)^{1/3}\right] \quad . \qquad (3\text{-}54)$$

This functional dependence provides an interesting analogy to the square-root region for pure gaseous absorption in which

$$\bar{t} \to \exp\left[-2(a\tau_a)^{\frac{1}{2}}\right] \quad .$$

3-18

c) _Arbitrary_ τ_s

Numerical studies have been carried out on the integral representation of the function $\overline{t}'$, given by Eq. (3-39). Some results of these calculations are shown in Figures 3-3 to 3-5, in which $\overline{t}'$ is plotted against $\overline{\tau}_a$, the mean absorption optical depth, for various values of τ_s, the scattering optical depth and a , the fine structure coefficient. The linear scale for $\overline{\tau}'$ does not show the precise asymptotic behavior at $\overline{\tau}'$ very close to 0 or 1, but does indicate a smooth, well-behaved dependence on τ_s, encouraging confidence in the approach of seeking an analytical or semi-empirical functional representation.
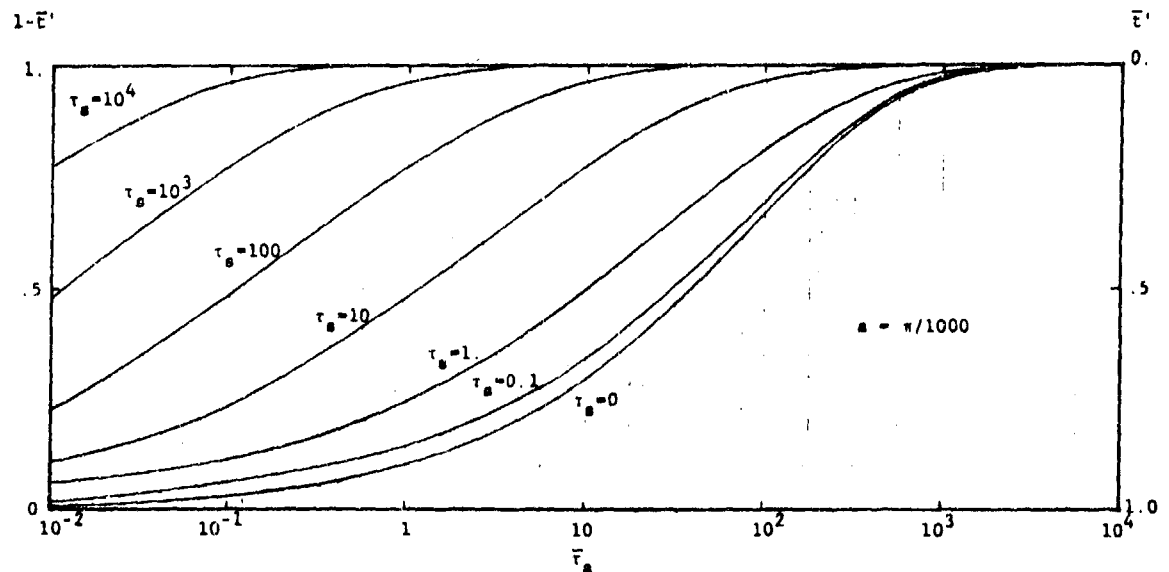
Figure 3-3.   Plot of $\overline{t}'$ vs. $\overline{\tau}_a$ for $a = \pi/1000$ and τ_s ranging from 0 to 10^4.
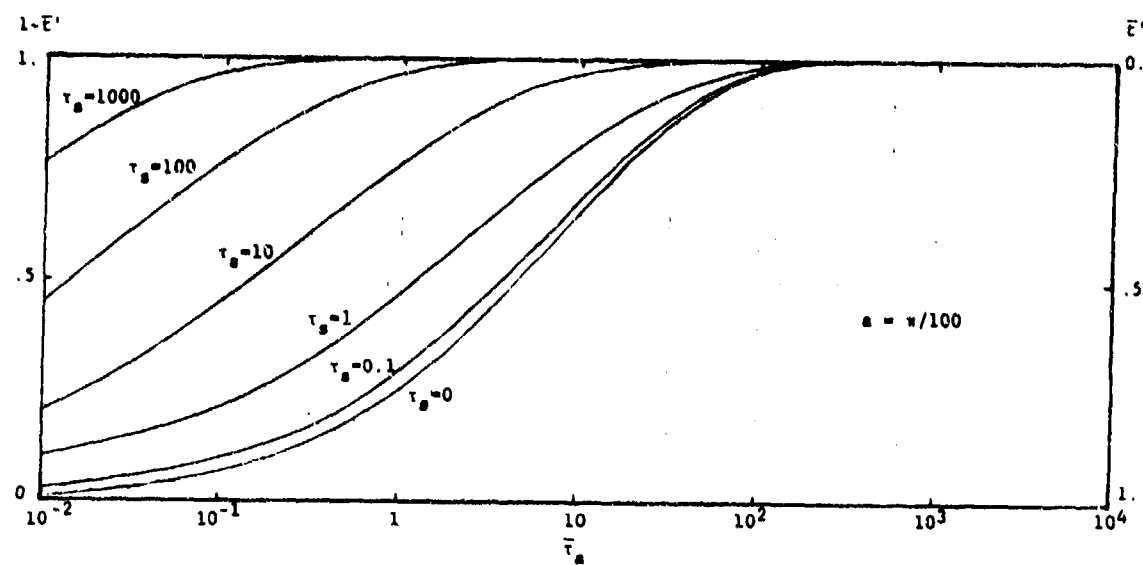
Figure 3-4. Plot of $\bar{t}'$ vs. $\bar{\tau}_a$ for $a = \pi/100$ and τ_s ranging from 0 to 10^3.
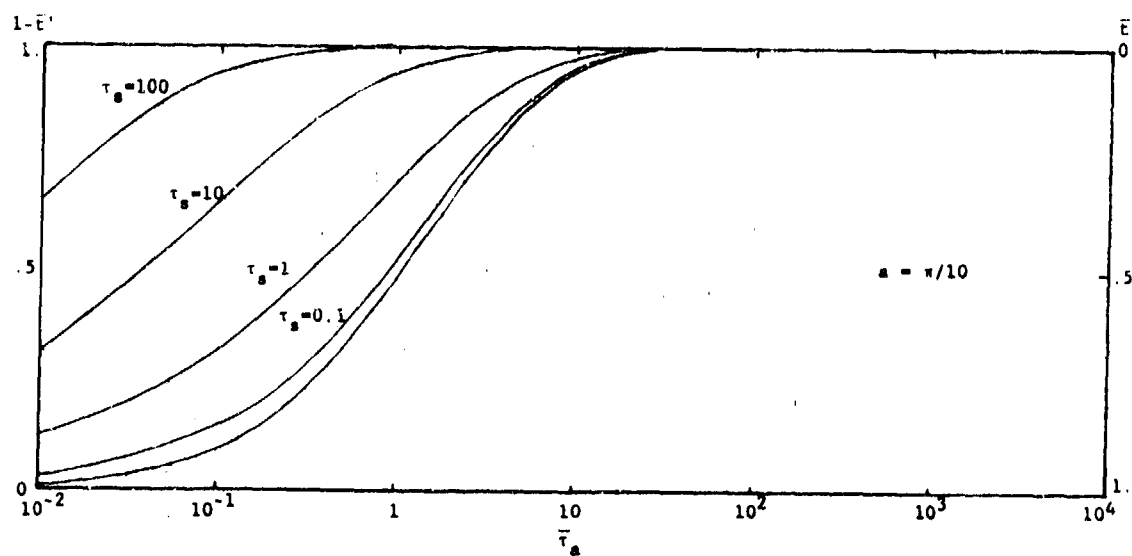
Figure 3-5. Plot of $\bar{t}'$ vs. $\bar{\tau}_a$ for $a = \pi/10$ and τ_s ranging from 0 to 10^2.

The asymptotic region of small $\bar{t}'$ was examined in detail. The conclusion was reached that the particular asymptotic form developed above [see Eq. (3-54)] is of major practical significance. A plot of the ratio $\bar{t}'/\exp[-3(\frac{1}{2}a\bar{\tau}_a\tau_s)^{\frac{1}{3}}]$ is presented in Figure 3-6. This ratio can be seen to approach the predicted theoretical value of $(4/3)^{\frac{1}{2}} = 1.1547$ closely as $a \to 0$ even for small values of
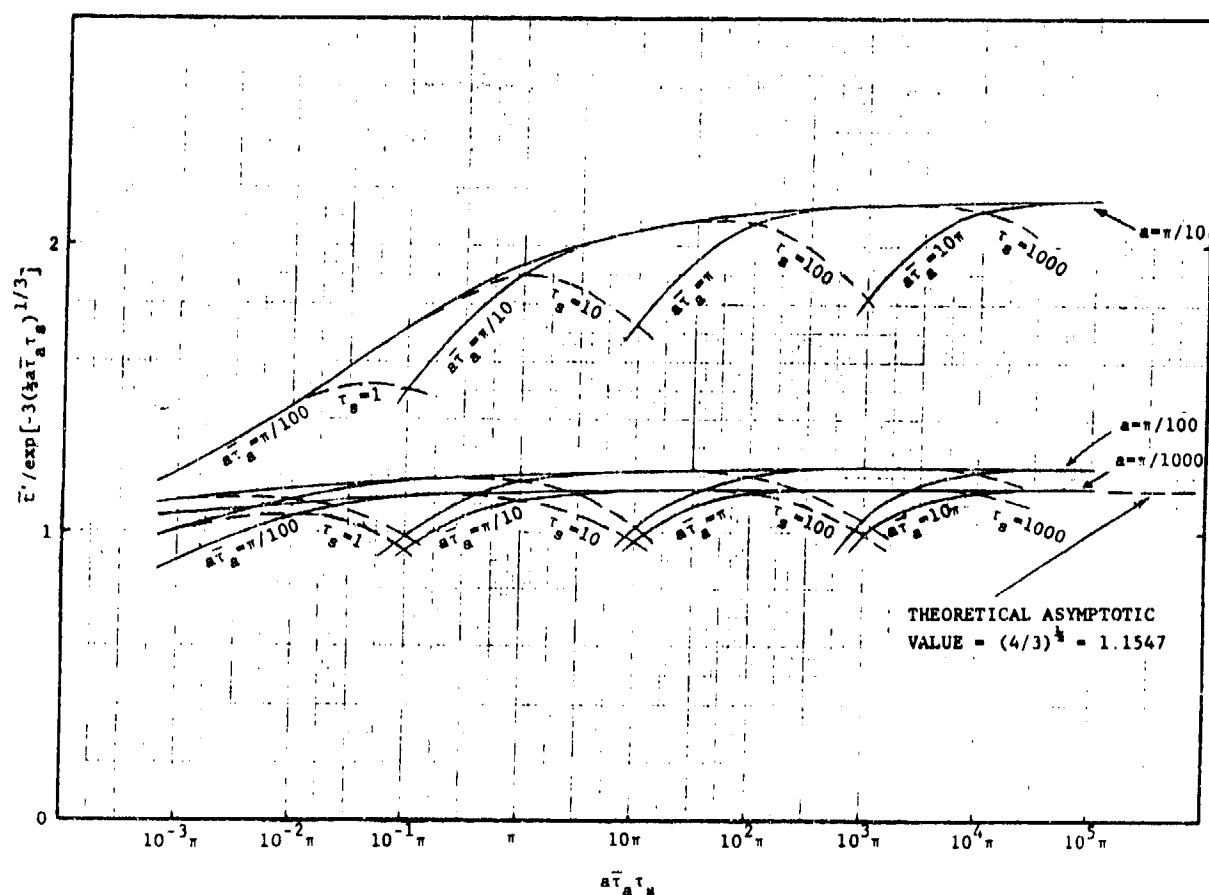
Figure 3-6. Plot of $\bar{t}'/\exp[-3(\frac{1}{2}a\bar{\tau}_a\tau_s)^{1/3}]$ vs. $a\bar{\tau}_a\tau_s$ showing asymptotic behavior for "large" τ_s (ranging from 1 to 10^3), for various values of a and $a\bar{\tau}_a$. The range of values of $a\bar{\tau}_a\tau_s$ corresponds to a range of $\bar{t}'$ from about 0.7 at the left to essentially zero at the right.

3-21

$a\bar{\tau}_a\tau_s$, when τ_s is sufficiently large. Empirically, for a $\lesssim 0.05$ and $\tau_s \gtrsim 10a\bar{\tau}_a$, the asymptotic approach is quite close (within about 10%, even for $a\bar{\tau}_a\tau_s$ as small as 10^{-2}, corresponding to transmissivities as large as 0.6). For larger values of a, an asymptotic value is approached, whose magnitude depends on the value of a. The particular functional dependence could be determined theoretically or empirically (e.g., an asymptotic value of $(4/3)^{\frac{1}{2}}\exp(2a)$ provides an excellent fit over the range of values of a considered here).

3.2.3 Empirical formulations for scattering band models. A study was made of possible empirical forms in the scattering band model representation based on the previous theoretical studies and numerical calculations. No exact explicit expressions were derived for the general case, but various limiting cases were studied, and any empirical form considered should have the appropriate theoretical asymptotic behavior. The numerical calculations then serve to select the best representation for intermediate values of the parameters.

Specifically, the function previously defined at $\bar{t}'$ (analogous to the mean transmissivity function $\bar{t}$ for the no-scattering limit) is desired to have the following limits:

A) No scattering ($\tau_s = 0$): $\bar{t}' \to \bar{t} = \exp\left|-f(\bar{\tau}_a, a)\right|$ where f is the appropriate gaseous band model curve of growth, in which a is the fine-structure parameters and $\bar{\tau}_a$ the mean absorption optical depth ($= \bar{k}u_x$ where $\bar{k}$ is the gaseous absorption coefficient and u_x the amount of the absorbing gas, in reciprocal units). The function f may include particulate absorption, i.e., be replaced by $f(\bar{\tau}_a, a) + \tau_o$, where f is the pure gas curve of growth and τ_o is a spectrally constant absorption optical depth (gaseous and/or particulate).

B) Weak scattering ($\tau_s \ll \bar{\tau}_a$)

$$\bar{t}' \approx \exp\left|-f(\bar{\tau}_a, a) - \tau_s\right|$$

in which f may include particulate absorption as in (A).

C) Constant absorption coefficient (gaseous and/or particulate).

$$(a \to \infty \; ; \; f(\bar{\tau}_a, a) \to \bar{\tau}_a \text{ for any band model})$$
$$\bar{t}' \to \exp\left|-(\bar{\tau}_a^2 + 2\bar{\tau}_a\tau_s)^{\frac{1}{2}}\right| \text{ (this is a func-}$$

tional requirement of either the two-flux or six-flux treatment for constant absorption coefficient).

D) Strong-line, large scattering limit (no particulate absorption)

$$(\bar{\tau}_a/a \text{ large, } \tau_s \text{ large})$$
$$\bar{t}' \to c_1 \exp\left|-c_2(\bar{\tau}_a a\tau_s)^{1/3}\right|$$

3-23

for a random band model, with $c_1 \sim 1$ and $c_2 \sim 2.4$. This important limiting behavior was derived in the previous study and is analogous to the strong-line limit for gaseous absorption $\bar{t} \rightarrow \exp \left[-2(\bar{\tau}_a a)^{\frac{1}{2}} \right]$.

An empirical form satisfying (A), (B), and (C) is

$$\bar{t}' = \exp \left[-f(\bar{\tau}_a, a) \left\{ 1 + \frac{2 \tau_s}{f(\bar{\tau}_a, a)} \right\}^{\frac{1}{2}} \right] \tag{3-55}$$

This is the form utilized intuitively in the Vanderbilt-Slack program. However, in limiting case (D) it approaches
$\bar{t}' \rightarrow \exp(-2\bar{\tau}_a^{\frac{1}{4}} a^{\frac{1}{4}} \tau_s^{\frac{1}{2}})$.

Alternatively, a form satisfying (A), (B), and (D) is

$$\bar{t}' = \exp \left[-f(\bar{\tau}_a, a) \left\{ 1 + \frac{3 \tau_s}{f(\bar{\tau}_a, a)} \right\}^{1/3} \right] \tag{3-56}$$

Although this form provides a better fit to the numerical values calculated for intermediate ranges of the parameters, it does not have the proper form to match limit (C); instead
$\bar{t}' \rightarrow \exp \left[-(\bar{\tau}_a^3 + 3\bar{\tau}_a^2 \tau_s)^{1/3} \right]$. For this reason, a more elaborate form containing all four limiting cases above is sought.

A convenient form having these required limits is

$$\bar{t}' = \exp \left\{ -f(\bar{\tau}_a, a) \left[1 + \frac{2\tau_s}{f(\bar{\tau}_a, a)} \right]^{\frac{1}{2}} \left[\frac{\left|(\bar{\tau}_a+c)a\right|^n}{\left|(\bar{\tau}_a+c)a\right|^n + \left|b\tau_s^2(1 - \frac{f(\bar{\tau}_a, a)}{\tau_a})\right|^n} \right]^{\frac{1}{12n}} \right\} \tag{3-57}$$

3-24

where b, c and n are empirical constants. Numerical evaluation
of this equation has shown significantly improved agreement
relative to the previous forms. The curve of growth $f(\bar{\tau}_a, a)$
may include a particulate absorption optical depth.

Figure 3-7, -9, and -11 show comparisons of the exact values
of $\bar{t}'$ previously calculated for $\pi/10^3 < a < \pi/10$ (solid lines)
with the approximation given by Equation (3-55) (dashed line).
This approximation is seen to be especially poor for large
τ_s and small a (i.e., when condition (D) should be met).

Figure 3-8, -10 and -12 show comparisons of the same values
of $\bar{t}'$ with the empirical form given by Equation (3-57) for the
case c=1, n=1, b=1/8. The improved match overall is evident.
No effort was made at optimization of the parameters b, c, and
n. It is anticiapted that an optimized version of this form
(or a very similar one) will be used in the basic formulation
of the SIRRM band model representation.

All the results shown here have been obtained for the
exponential-tailed 1/S random band model. The expression for
the absorption coefficient probability distribution function
for the Goody model is so mathematically intractable as to make
it extremely unattractive for similar theoretical or numerical
studies. However, the conclusions reached here regarding proper
asymptotic and approximate forms are certainly also applicable
to the Goody model (whose curve of growth for the non-scattering
case is only slightly different from that of the exponential-
tailed 1/S model).
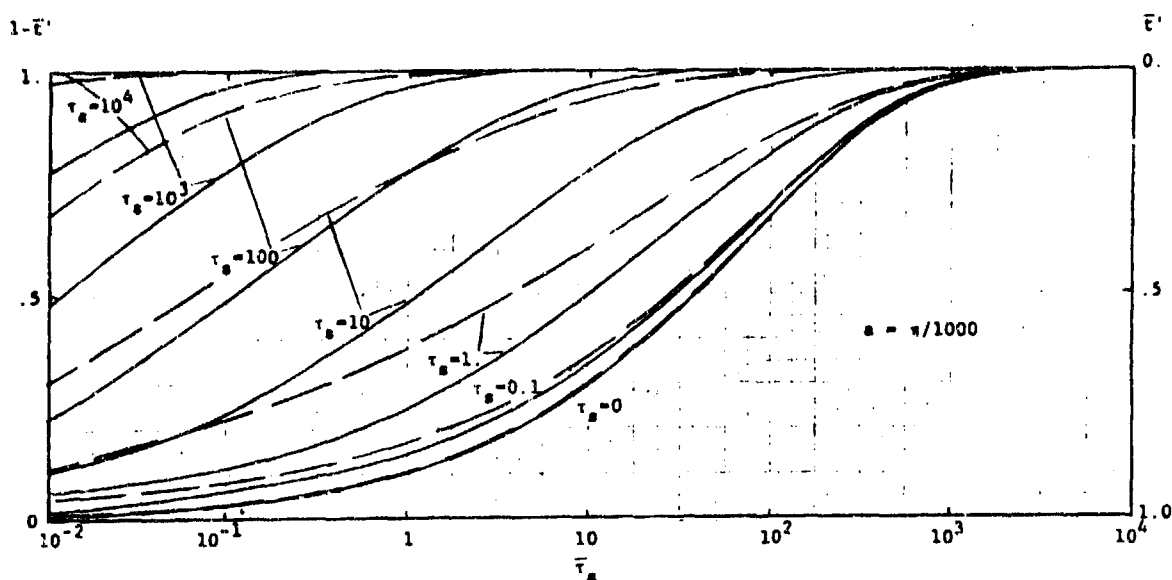
3-25

Figure 3-7. Plot of $\bar{t}'$ vs. $\bar{\tau}_a$ for $a = \pi/1000$ and τ_s ranging from 0 to 10^4 compared with approximation (1).

Figure 3-8. Plot of $\bar{t}'$ vs. $\bar{\tau}_a$ for $a = \pi/1000$ and τ_s ranging from 0 to 10^4 compared with approximation (3).
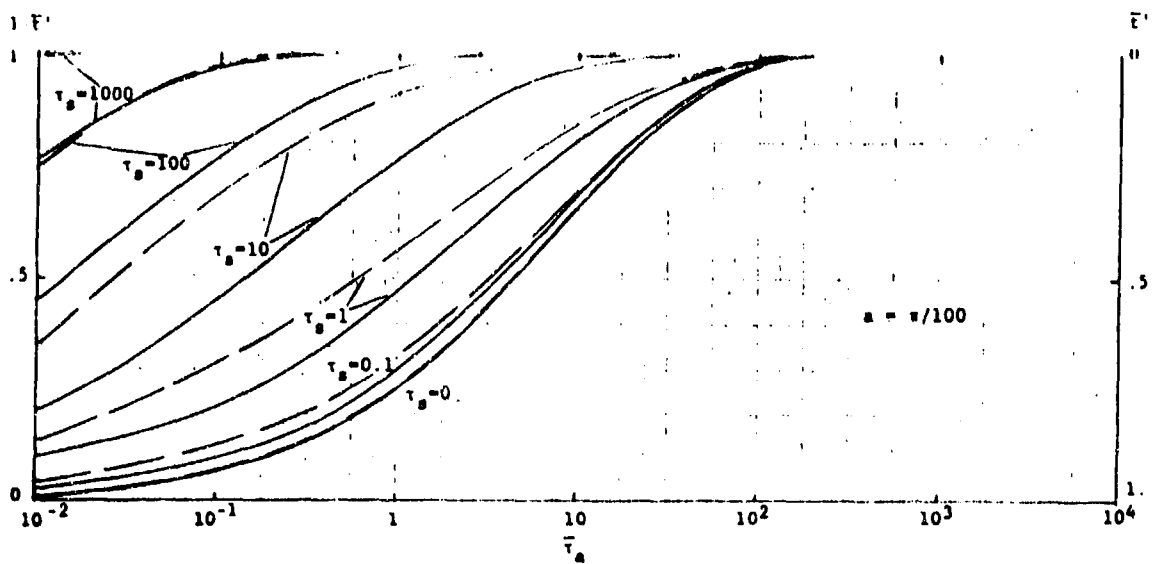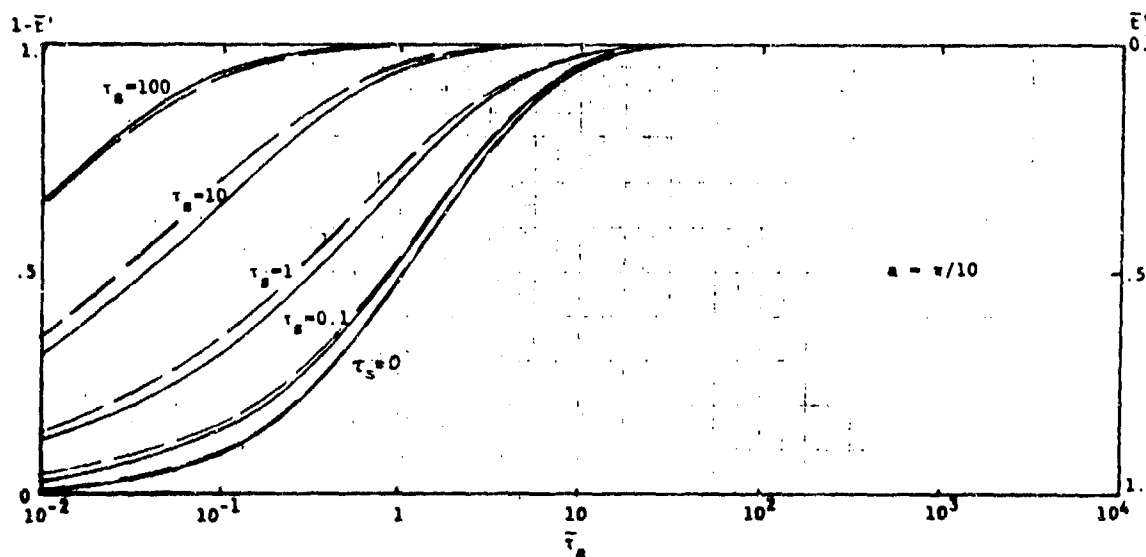
3-26

Figure 3-9.   Plot of $\bar{t}'$ vs. $\bar{\tau}_a$ for a = $\pi/100$ and
τ_s ranging from 0 to 10^3 compared with
approximation (1).

Figure 3-10.   Plot of $\bar{t}'$ vs. $\bar{\tau}_a$ for a = $\pi/100$ and
τ_s ranging from 0 to 10^3 compared with
approximation (3).

3-27
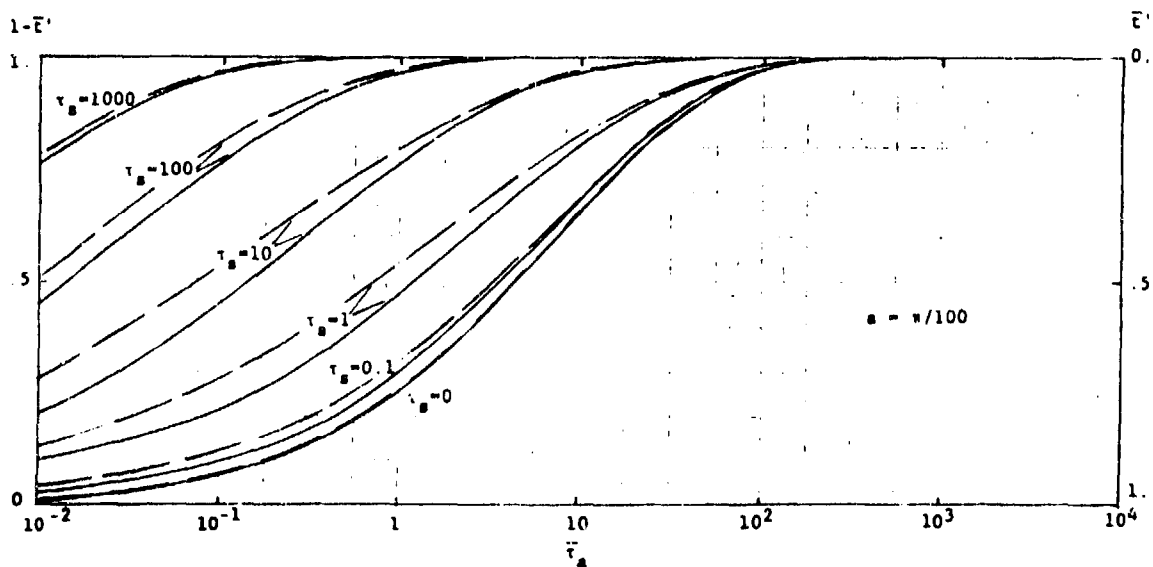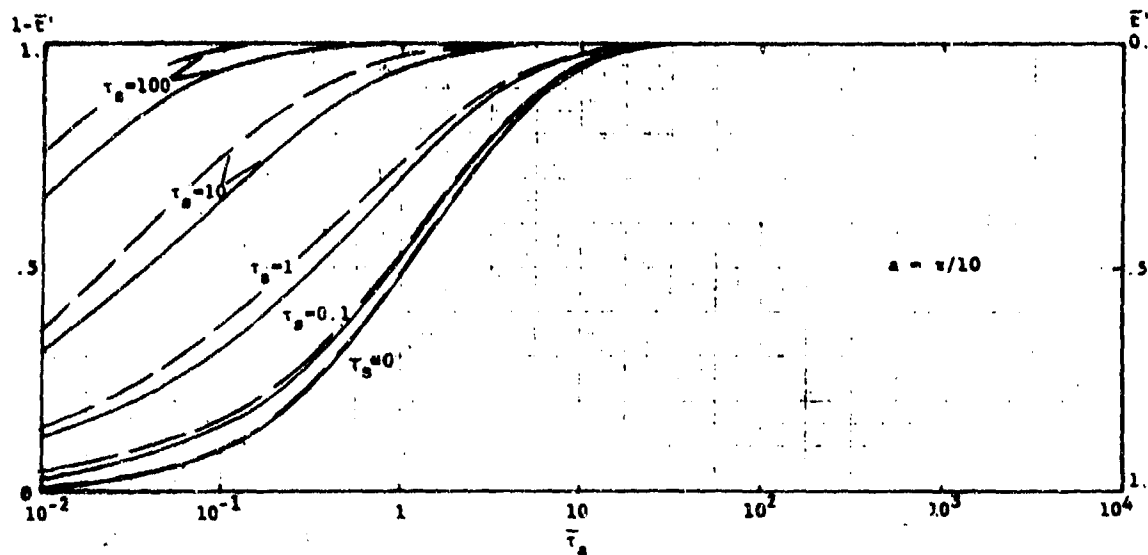
Figure 3-11.   Plot of $\bar{t}'$ vs. $\bar{\tau}_a$ for $a = \pi/10$ and
τ_s ranging from 0 to 10^2 compared with
approximation (1).

Figure 3-12.   Plot of $\bar{t}'$ vs. $\bar{\tau}_a$ for $a = \pi/10$ and
τ_s ranging from 0 to 10^2 compated with
approximation (3).

3-28

The preceding development is for single band models (with or without particle or other gaseous absorption). In practice, it is anticipated that methods of combining band model parameters will be utilized which are analogous to those in current use in gaseous radiative transfer codes (e.g., the Curtis-Godson approximation).

OPTICAL PARAMETERS OF PARTICLES

4.1. Introduction

The treatment of the gas/particles radiative transfer requires
as inputs the volume extinction coefficients and angular scat-
tering phase functions. These quantities can be derived from the
primary optical parameters by use of the Mie theory, which des-
cribes the scattering and absorption properties of a homogeneous
sphere whose optical properties are given by the complex index
of refraction. Although the Mie theory is based upon the ideal-
ization of homogeneous spherical particles, it can be considered
as a very reasonable first approximation since real plume particles
were often found to be solid spheres (Rochelle, 1967). In
addition, higher order account of particle non-uniformity and
non-sphericity is prohibitively complex (Kerker, 1969) and not
warranted by the present state of knowledge. Exact solutions
of the wave equations are obtained by the matching of boundary
conditions at the surface of the sphere. The solutions are ex-
pressed as infinite series involving Legendre polynomials and
Ricatti-Bessel functions. Evaluation of the formal series
solution proves computationally difficult for some ranges of
the parameters and considerable effort has been expended in the
past on the development of efficient and accurate computational
methods of evaluating these solutions. The most recent treat-
ment is by Dave (1972) and it is his approach that is being used
in the present program. A brief discussion together with the ex-
tension from single particles to particle distributions is given
in Section 4.2.

A preliminary listing of the particulate species of interest is given in Table 4-1 together with an indication of the availability of the index of refraction (n_1) and the absorption index (n_2) measured in a given temperature interval. Only four out of nine particulate species are sufficiently known, and these will have to serve as representatives until more information about the remaining species becomes available.

TABLE 4-1. LIST OF EXHAUST PARTICULATE SPECIES
AND THE AVAILABILITY OF n_1 and n_2.

PARTICLE		$n_1(T,\lambda)$	$n_2(T,\lambda)$	SOURCE
$A\ell_2O_3$	(s)	300-1800K	300-1800	Aerospace
C	(s)	300K	300-3000	Aerospace/PRA Estimate
MgO	(s)	300-2225K	300-2225	Aerospace
ZrO_2	(s)	300-600K	300-600	Aerospace
ZrC	(s)			
BN	(s)	300K(Na-D)		Kordes (1960)
B_2O_3	(ℓ)	300K(Na-D)		Handbook Chem.Phys.for (s)
BeO	(s)	300K(Na-D)		Handbook Chem.Phys.
Be_3N_2				

Representative results of volume coefficients and angular scattering phase functions for $A\ell_2O_3$ and carbon particle distributions are given in Section 4.3. The results indicate that the large variations in coefficients and phase functions typically observed as a function of wavelength and scattering angle for single particles are greatly reduced when realistic size distributions are introduced. In addition, the influence of the

A preliminary listing of the particulate species of interest is given in Table 4-1 together with an indication of the availability of the index of refraction (n_1) and the absorption index (n_2) measured in a given temperature interval. Only four out of nine particulate species are sufficiently known, and these will have to serve as representatives until more information about the remaining species becomes available.

TABLE 4-1. LIST OF EXHAUST PARTICULATE SPECIES
AND THE AVAILABILITY OF n_1 and n_2.

PARTICLE		$\eta_1(T,\lambda)$	$\eta_2(T,\lambda)$	SOURCE
Al_2O_3	(s)	300-1800K	300-1800	Aerospace
C	(s)	300K	300-3000	Aerospace/PRA Estimate
MgO	(s)	300-2225K	300-2225	Aerospace
ZrO_2	(s)	300-600K	300-600	Aerospace
ZrC	(s)			
BN	(s)	300K(Na-D)		Kordes (1960)
B_2O_3	(ℓ)	300K(Na-D)		Handbook Chem.Phys.for (s)
BeO	(s)	300K(Na-D)		Handbook Chem.Phys.
Be_3N_2				

Representative results of volume coefficients and angular scattering phase functions for Al_2O_3 and carbon particle distributions are given in Section 4.3. The results indicate that the large variations in coefficients and phase functions typically observed as a function of wavelength and scattering angle for single particles are greatly reduced when realistic size distributions are introduced. In addition, the influence of the

OPTICAL PARAMETERS OF PARTICLES

4.1. Introduction

The treatment of the gas/particles radiative transfer requires as inputs the volume extinction coefficients and angular scattering phase functions. These quantities can be derived from the primary optical parameters by use of the Mie theory, which describes the scattering and absorption properties of a homogeneous sphere whose optical properties are given by the complex index of refraction. Although the Mie theory is based upon the idealization of homogeneous spherical particles, it can be considered as a very reasonable first approximation since real plume particles were often found to be solid spheres (Rochelle, 1967). In addition, higher order account of particle non-uniformity and non-sphericity is prohibitively complex (Kerker, 1969) and not warranted by the present state of knowledge. Exact solutions of the wave equations are obtained by the matching of boundary conditions at the surface of the sphere. The solutions are expressed as infinite series involving Legendre polynomials and Ricatti-Bessel functions. Evaluation of the formal series solution proves computationally difficult for some ranges of the parameters and considerable effort has been expended in the past on the development of efficient and accurate computational methods of evaluating these solutions. The most recent treatment is by Dave (1972) and it is his approach that is being used in the present program. A brief discussion together with the extension from single particles to particle distributions is given in Section 4.2.

temperature on the coefficients and phase functions for solid carbon is minimal.

In the last section, we recommend a scheme for the Data File that combines flexibility and minimum requirements in the operation of the SIRRM code.

4.2 Formalism of the Mie Scattering

4.2.1 Single particle. In the Mie theory, the primary quantities:

$$S_1(a,n,\Theta)$$
$$S_2(a,n,\Theta)$$
$$Q_{ext}(a,n)$$
$$Q_{sca}(a,n)$$

are calculated (Van de Hulst, 1957) where S_1 and S_2 are amplitude functions related to the planes of polarization, Q_{ext} and Q_{sca} are the extinction and scattering efficiencies, a is the size parameter ($a=2\pi r/\lambda$, with radius r of scattering sphere and wavelength λ), n is the refractive index ($n=n(\lambda) = n_1(\lambda)-in_2(\lambda)$) and θ is the angle between the directions of incoming and scattered radiation. After the primary quantities are calculated, the intensities of the scattered radiation and their degrees of polarization can be determined. The calculation is simplified by repeated use of recursion relationships and efficient computing methods have been developed (Deirmendjian, 1969; Dave 1969, 1970A, 1970B). In the following, the approach taken by Dave (1972) is briefly described.

4-3

The intensity scattered by a single spherical particle per unit solid angle for unity incident intensity is given by

$$I(a,n,\Theta) = \frac{1}{4\pi} (\pi r^2) Q_s(a,n) M(a,n,\Theta) \qquad (4\text{-}1)$$

where $M(a,n,\theta)$ is the normalized scattering phase function, which is given by

$$M(a,n,\theta) = \sum_{k=1}^{n} \Lambda_k(a,n) P_{k-1}(\cos \Theta) \qquad (4\text{-}2)$$

where $P_{k-1}(\cos \Theta)$ are the Legendre polynomials. The coefficients of the Legendre series are given by

$$\Lambda_k(a,n) = \frac{2}{a^2 Q_s(a,n)} \left[L_k^{(1)}(a,n) + L_k^{(2)}(a,n) \right]$$

where the functions $L_k^{(1),(2)}(a,n)$ are computed from the values of the complex Mie amplitude $a_n(a,n)$ and $b_n(a,n)$. The extinction and scattering efficiencies are given by

$$\left.\begin{aligned} Q_{ext}(a,n) &= \frac{2}{a^2} \sum_{n=1}^{\infty} (2n+1) \; Re\{a_n + b_n\} \\[2em] Q_{sca}(a,n) &= \frac{2}{a^2} \sum_{n=1}^{\infty} (2n+1) \; \{|a_n|^2 + |b_n|^2\} \end{aligned}\right\} (4\text{-}3)$$

The amplitudes a_n and b_n are expressible in terms of the spherical Bessel functions of the first and second kind. Using the method of logarithmic derivative function $A_n(a,n)$ of the Bessel functions, the numerical computations are facilitated. However, difficulties

exist in computing $A_n(a,n)$ under certain conditions (Deirmendjian, 1969). Kattawar and Plass (1967) found that these difficulties can be avoided by using a downward recurrence scheme for $A_n(a,n)$ which is basically stable. Dave (1972) has adopted this scheme in his approach.

4.2.2 Particle size distribution. Since rocket exhaust plumes do not, in general, consist of particles with only one fixed size, it is necessary to investigate the characteristics of size distributions. These characteristics are described by the volume extinction coefficient β_{ext}, the volume scattering coefficient β_{sca}, the volume absorption coefficient β_{abs} and the normalized scattering phase function $M(\theta)$. These quantities are dependent on $n(\lambda)$ and various parameters describing different size distributions. They can be expressed as

$$M(\theta) = \sum_{k=1}^{K} \Lambda_k(r_j) \, P_{k-1}(\cos \theta) \qquad (4-4)$$

and

$$\beta_z(r_j) = \pi \int_{r_{min}}^{r_j} Q_z(a,n) r^2 \, N(r) dr \qquad (4-5)$$

4-5

where z stands for ext, sca or abs. The normalized Legendre coefficients become

$$\Lambda_k(r_j) = \frac{\lambda^2}{\pi \; \beta_{sca}(r_j)} \int_{r_{min}}^{r_j} L_k(a,n) \quad N(r)dr \qquad (4\text{-}6)$$

The phase function is normalized according to

$$\int_{4\pi} M(\theta)\sin\theta d\theta d\phi \;\; = \;\; 4\pi$$

The distribution N(r) is given by

$$N(r) = Nf(r) \qquad\qquad (4\text{-}7)$$

where N is total number of particles per unit volume and $\int_0^\infty f(r)dr = 1$. Dave (1972) has made provisions to use any one of three different size distribution functions. We are interested in the discontinuous power law type

$$f(r) = C \qquad\qquad \text{for } r_{min} \leqslant r \leqslant r_m$$

$$f(r) = C(r_m/r)^{\nu+1} \text{ for } r_m \leqslant r \leqslant r_{max}$$

$$\left.\vphantom{\begin{array}{c}1\\1\\1\end{array}}\right\} \quad (4\text{-}8)$$

4-6

and the modified gamma function

$$f(r) = a \, r^{\alpha} e^{-br^{\gamma}} \text{ for } r_{min} \leqslant r \leqslant r_{max} \qquad (4\text{-}9)$$

It is found that the modified gamma function is representative of size distributions encountered in exhaust plumes with Al_2O_3 particles (Dawbarn, 1978). However, many different size distributions have been encountered which sometimes depend upon the method of collection (see Figure 4-1). The coefficients a, α, b and γ can be adjusted to represent any of the measured or calculated size distributions.
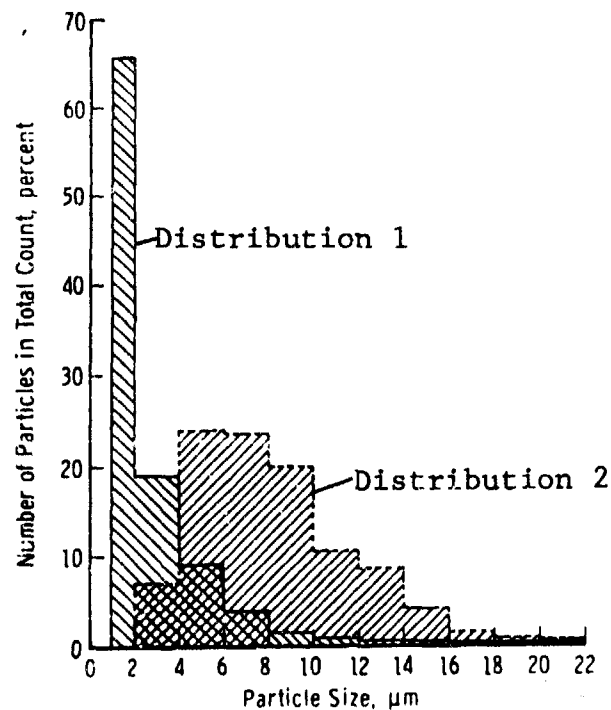
Figure 4-1. Two Al_2O_3 particle size distributions of Titan IIIc using two different collection methods (Dawbarn, 1978)

4-7

The parameters for the modified gamma function are not in-
dependent of each other and they have to be adjusted in a certain
manner to obtain a given size distribution that has its maximum at
radius r_m . This interdependence was investigated. The four
parameters may be reduced to two by utilizing the conditions

$$\frac{d\ f(r)}{dr} = 0 \quad \text{for} \quad r = r_m \qquad (4\text{-}10)$$

and

$$\int_c^\infty f(r) = 1$$

These conditions lead to

$$\alpha/b = \gamma\ r_m^{\ \gamma} \qquad (4\text{-}11)$$

$$1 = a\ \gamma^{-1}\ b^{-\xi}\Gamma(\xi) \qquad (4\text{-}12)$$

where $\xi = \dfrac{\alpha + 1}{\gamma}$ and $\Gamma(\xi)$ is the gamma function. At $r = r_m$,
$f(r)$ must assume a value between zero and unity (as determined by
experiment). Introducing Equations (4-11) and (4-12) into (4-10)
and solving for r_m results in

$$f(r) = \gamma^{1-\xi}\ \frac{\alpha^\xi}{\Gamma(\xi)}\ \frac{e^{-\alpha/\gamma}}{r_m} \qquad (4\text{-}13)$$

Assuming upper and lower values for $f(r_m)$, Equation (4-13) has
been solved for $f(r_m) \sim 1$ and $f(r_m) \sim .2$ using different values
of α and γ . The solutions are shown graphically in Figure 4-2.
A family of curves is made up for a given α , the upper and

lower limits of which are given by $f(r_m) \sim 1$ and $f(r_m) \sim .2$. Thus, pairs of α and γ can be chosen to describe any size distribution for r_m between 0.01 and 10 μm. The choice is dictated by the known (measured) standard deviation of the distribution function. The higher values of α and γ produce smaller standard deviations.
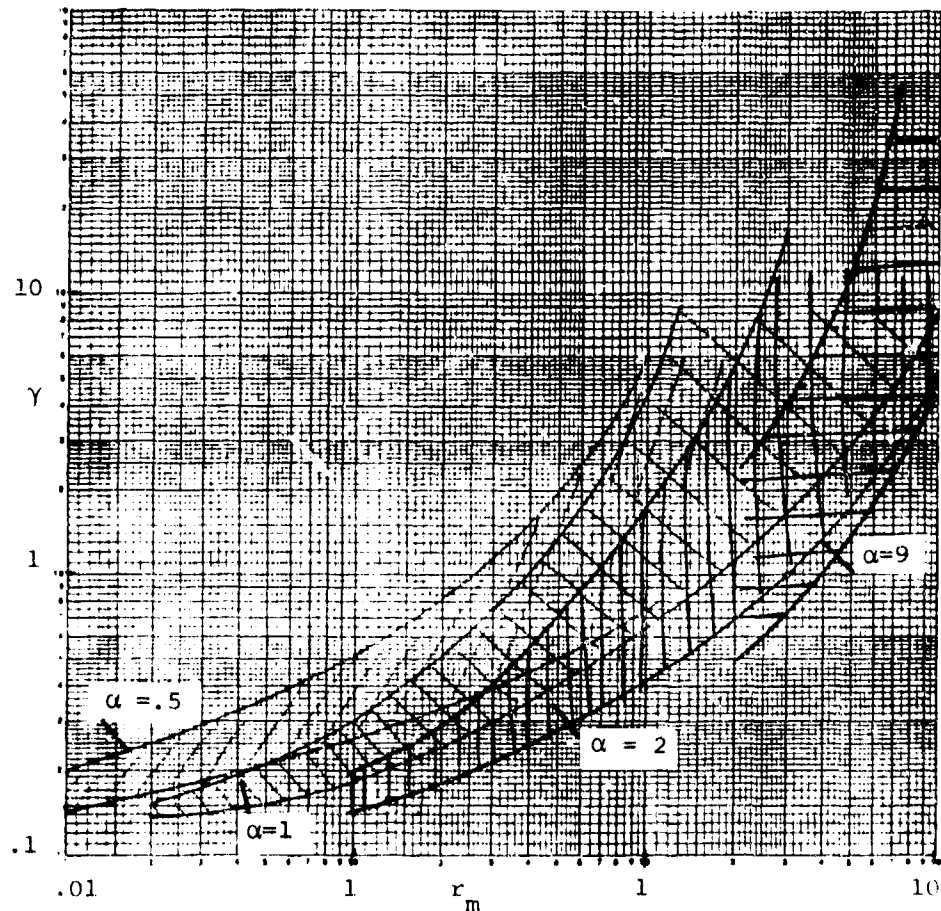
Figure 4-2. Families of Curves for which $0.2 \leq f(r_m) \leq 1$ at a given r_m as determined by pairs of γ and α.

Following a similar argument as was presented above for the
modified gamma function, the adjustable parameters in the dis-
continuous power law (Eq. 4-8) are determined through

$$\int_0^\infty f(r) = C \int_0^{r_m} dr + C \, r_m^{\nu+1} \int_{r_m}^\infty r^{-(\nu+1)} \, dr = 1$$

$$\nu = \frac{r_m}{1/C - r_m}$$

Based on a review of existing experimental data (Rochelle, 1967),
we have chosen r_m = 0.03 μm for solid carbon particles and C = 1.
With these assumptions, then $\nu \approx 0$. The size distribution is
shown in Figure 4-3. It resembles that used by Stull and Plass
(1960) which was based on data by Tesner (1959). Included in the
same figure is also the size distribution based on Equation (4-9).
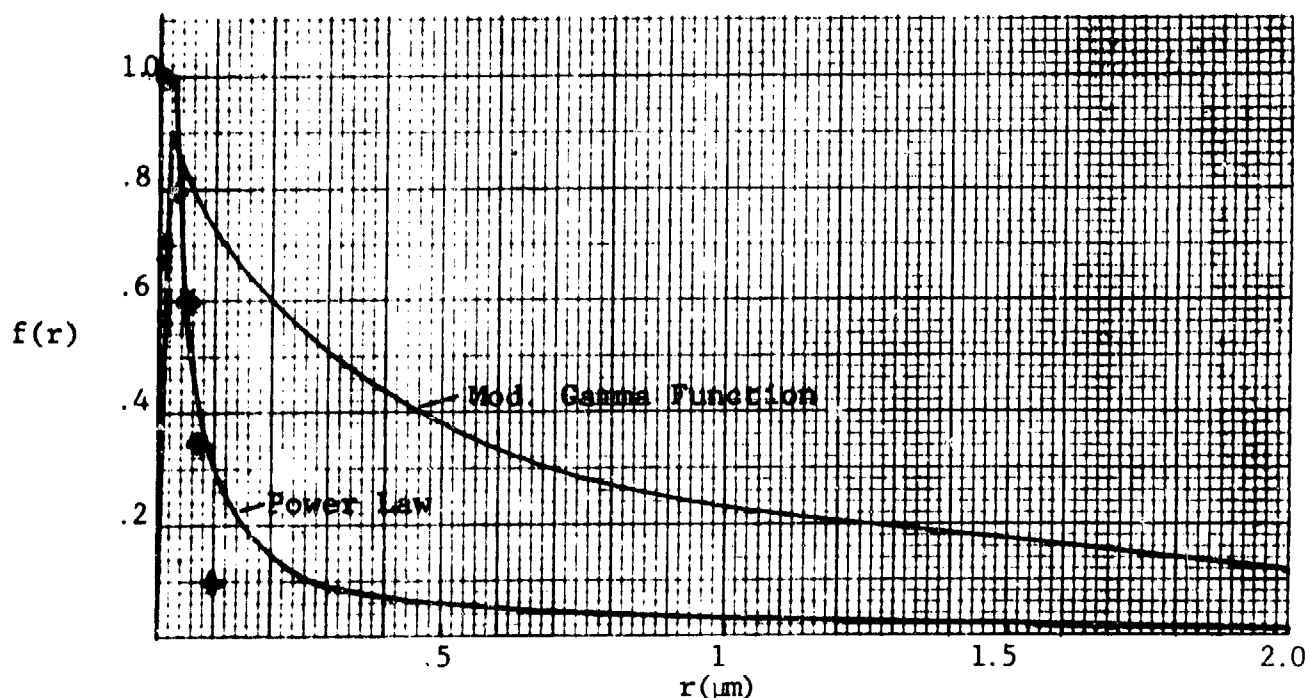
Figure 4-3. Size Distribution of Solid Carbon Particles in Rocket
Exhaust, based on the Two Distribution Functions Des-
cribed in the Text. Distribution used by Stull and
Plass (1960) is indicated by (+).

4.3 Optical Parameters

A set of representative values of n_1 and n_2 were collected by the Aerospace Corporation for Al_2O_3, C, MgO, and ZrO_2 (Whitson, 1975). Additional data for these particles were presented by Dowling and Randall (1977) in part based on experiments conducted during the "Particle Optical Properties Measurement (POPM) Program". Our effort was concentrated in comparing these data and study the influence of higher temperatures.

Carbon

As an example of the wide differences of measured refractive index n_1, and absorption n_2, Dowling and Randall have compared data on polycrystalline and pyrolytic graphite, pressed carbon soot, and a microcrystalline polished slab of graphite. The results for n_2 are shown in Figure 4-4. We have added the NASA Handbook
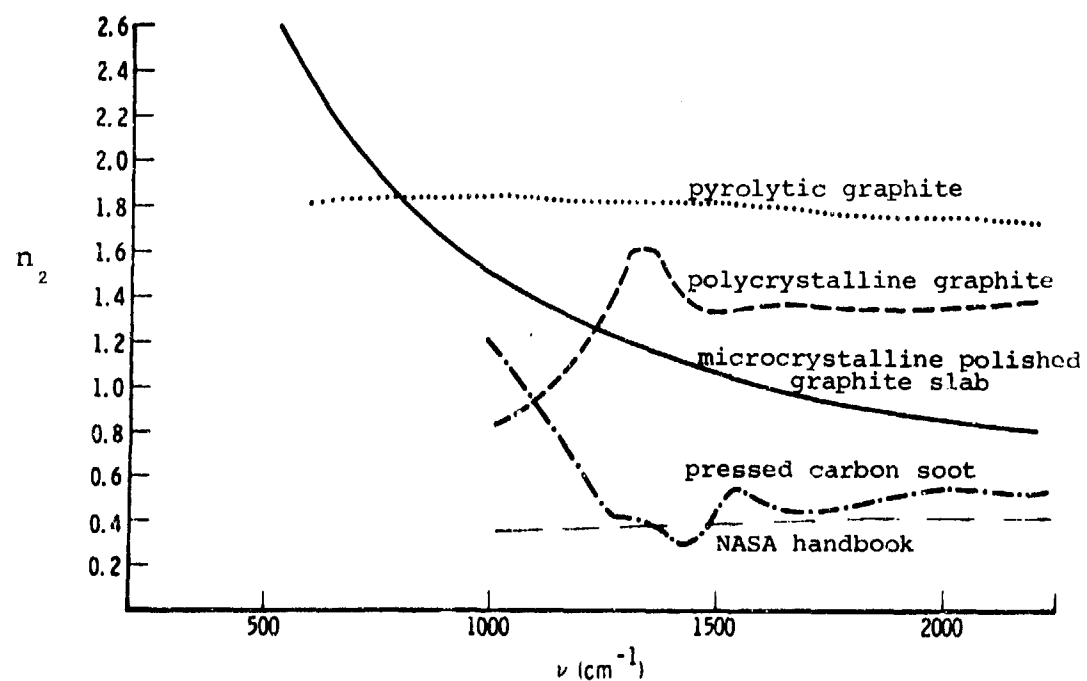
Figure 4-4. The Absorption Index of Carbon Materials in the Wavenumber Region 400 cm^{-1} to 2200 cm^{-1}.

data for room temperature. The "representative" values chosen by Whitson are those for the polycrystalline graphite.

In addition to room temperature data, the NASA Handbook lists high temperature data for the absorption coefficient of small carbon particles. These data were based in part on theoretical work and in part on measurements. We have extrapolated those data to 3000 K and to $\lambda = 25$ µm, using the relationship

$$k = k_c \frac{\lambda}{2\pi} \rho_o$$

to convert the absorption coefficients k_c (cm²/gm) into absorption indices, where $\rho_o = 2$g/cm³ was chosen as a representative value for the density of carbon. The results are plotted in Figure 4-5. We recommend to use these values for n_2 until more experimental data become available. For large particles compared with λ, the computed particle emissivity approaches the emissivity of a plane bulk sample. Dowling and Randall have calculated $\epsilon_n = .71$ for $\lambda < 25$ µm, choosing $n_1 = 3$ and $n_2 = 1$. Using the same formula, we have calculated ϵ_n parametrically for $0 \leqslant n_1 \leqslant 4$ and $0.5 < n_2 < 1.5$. The results are shown in Figure 4-6. Measured spectral emissivities as reported by Whitson range from .8 to 1.0 for different samples of graphite (except for pyrolytic, c-face) in the temperature regime from 1100 to 2300 K, pointing to a somewhat lower value of n_1 at higher temperatures.

Figure 4-6. Normal Emissivity of Plane Bulk Carbon as a Function of Index of Refraction for Different Extinction Coefficients.

Figure 4-5. Absorption Index of Carbon for Different Temperatures based on NASA Handbook and Room Temperature Data given by Whitson as "representative" (✱✱✱), and high temperature data by Krascella (---).

The only high temperature data for n_1 listed by Whitson
are due to N. K. Krascella (1966), and are plotted in Figure 4-7
together with Whitson's "representative" values at room tempera-
ture and our extrapolation to longer wavelengths.
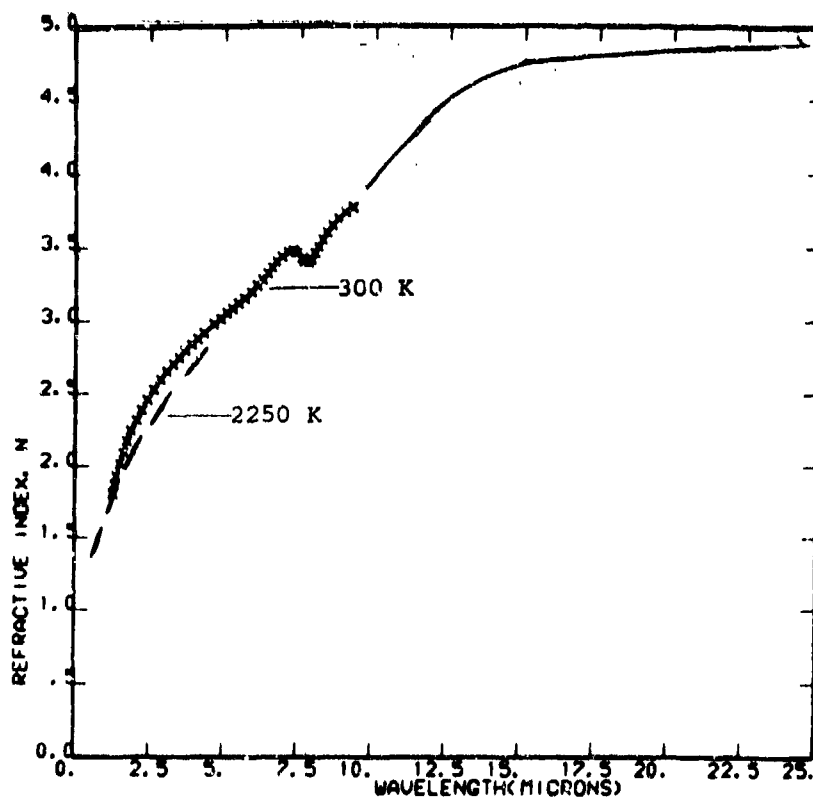
Figure 4-7. n_1(Carbon) vs. λ for $T = 300$ and 2250K,
based on the Compilation by Whitson
and our Extrapolation.

Al_2O_3

Experimental reflectivity measurements in the POPM program
at 300 and 678 K were used to determine n_1 and n_2 of Al_2O_3
(Dowling and Randall, 1977). The results are shown in Figure
4-8 and 4-9 and they indicate that n_1 and n_2 are reduced at
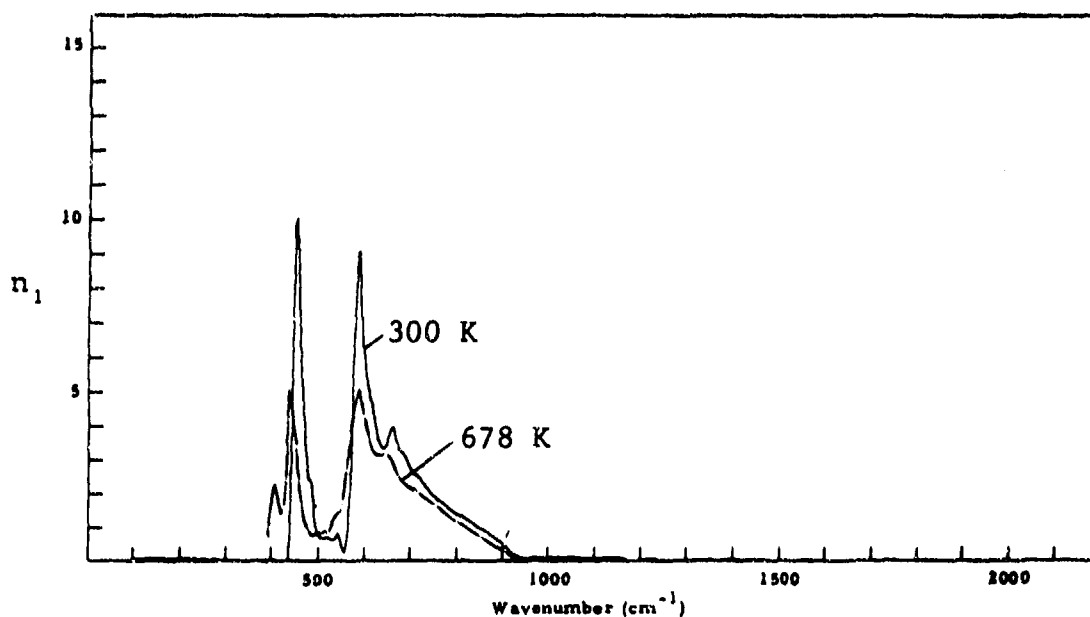
Figure 4-8. The Refractive Index (n_1) of Al_2O_3 in the Region 400 cm^{-1} to 2200 cm^{-1} as Determined from a Kramers-Kronig Analysis of Reflectivity Data taken at T=300 and 678 K (Dowling and Randall, 1977).
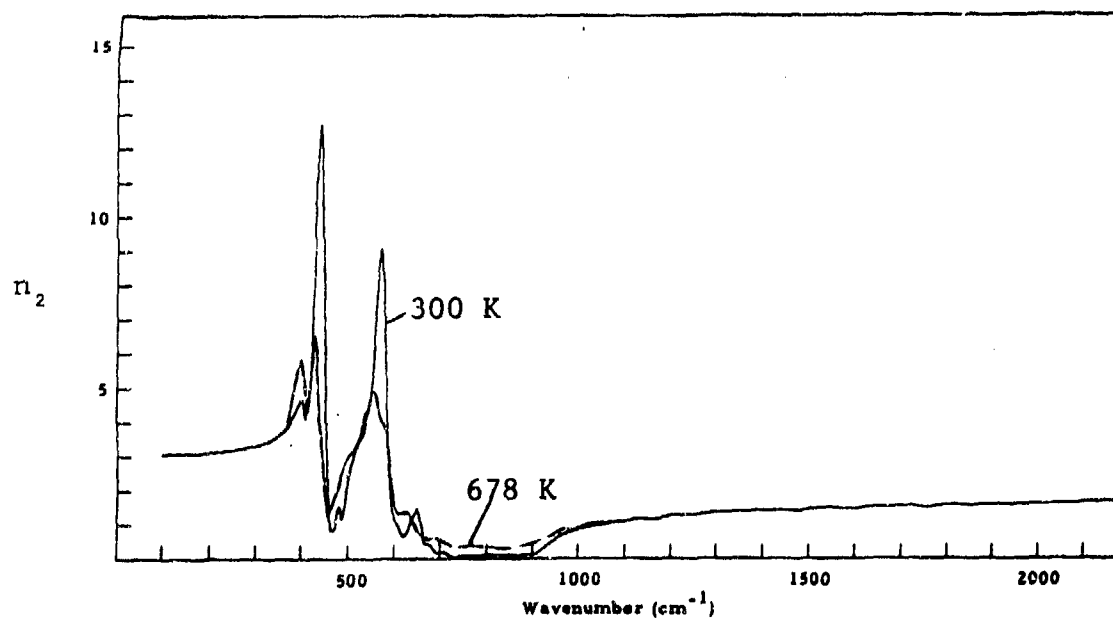
Figure 4-9. The Absorption Index (n_2) of Al_2O_3 in the 400 cm^{-1} to 2200 cm^{-1} as Determined from a Kramers-Kronig Analysis of Reflectivity Data taken at T=300 and 678 K (Dowling and Randall, 1977).

4-15

higher temperatures in the resonance region. A comparison with
the "representative" values by Whitson shows good agreement for the
room temperature data. Also the qualitative behavior at higher
temperatures in the resonance region has been observed by B. Piriou
(1966). The data as presented by Whitson are shown in Figures 4-10
and 4-11.
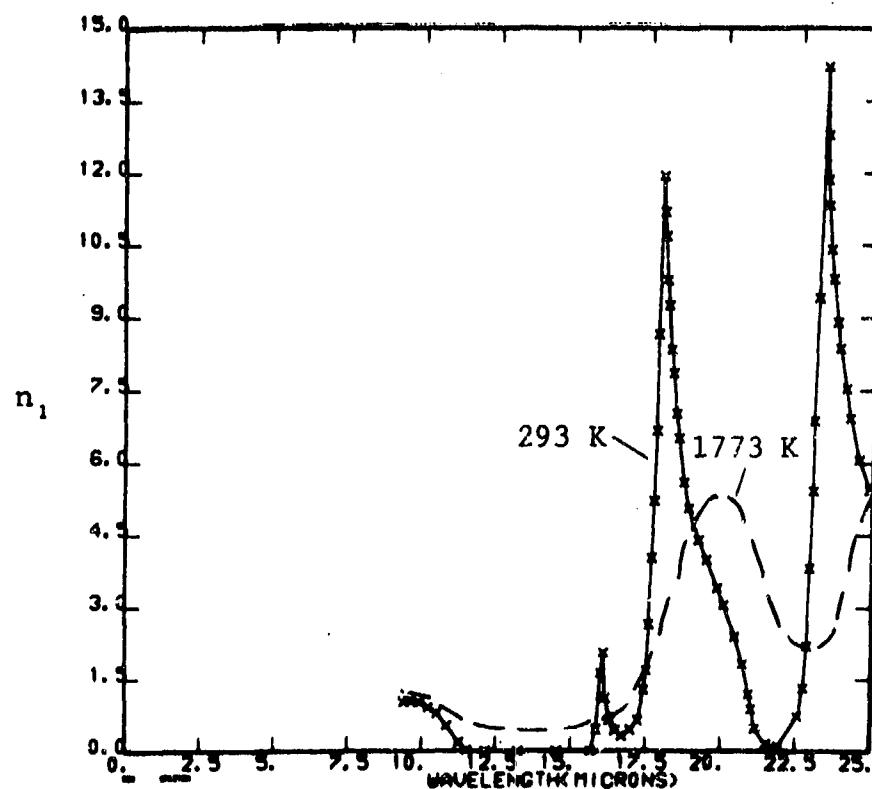
Figure 4-10. $n_1(Al_2O_3)$ as a Function of λ for Two Temperatures as Presented by Whitson (1975).
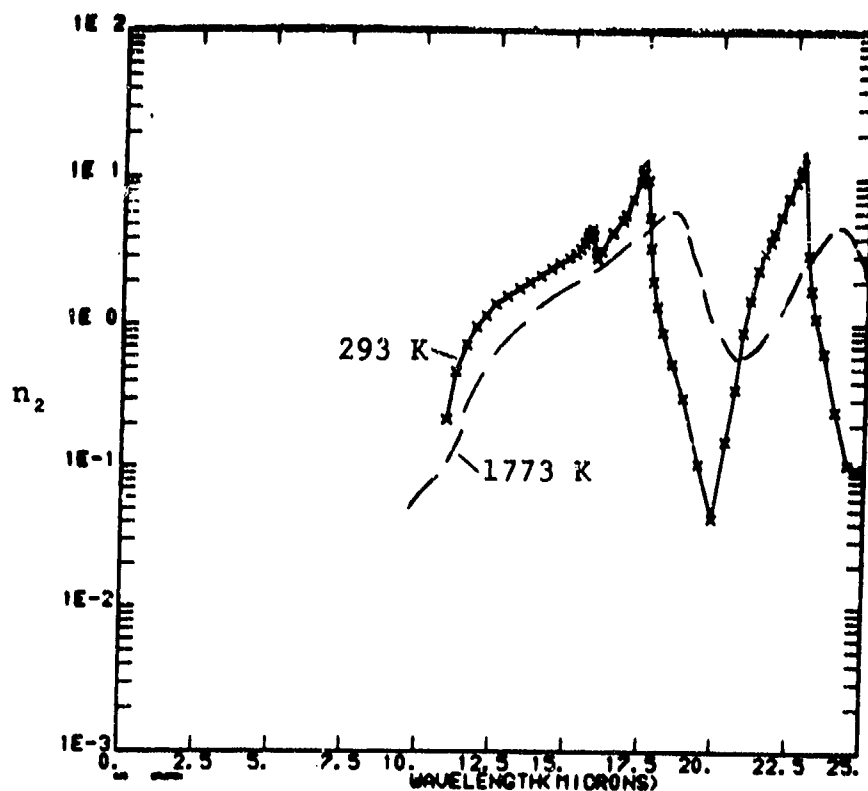
Figure 4-11. $n_2(Al_2O_3)$ as a Function of λ for Two Temperatures as Presented by Whitson (1975).

MgO

M. E. Whitson (1975) has listed experimental data of n_1 and n_2 taken by several workers. All of these are in general agreement and the "representative" values at room temperature are based on these values. There appears to be little or no dependency on temperature, as the data by B. Piriou (1966) indicate (see Figure 4-12 and 4-13). The experimental study and subsequent data analysis using classical dispersion theory by Dowling and Randall (1977) confirm these data. A comparison of n_1 and n_2 with Whitson's representative room temperature data
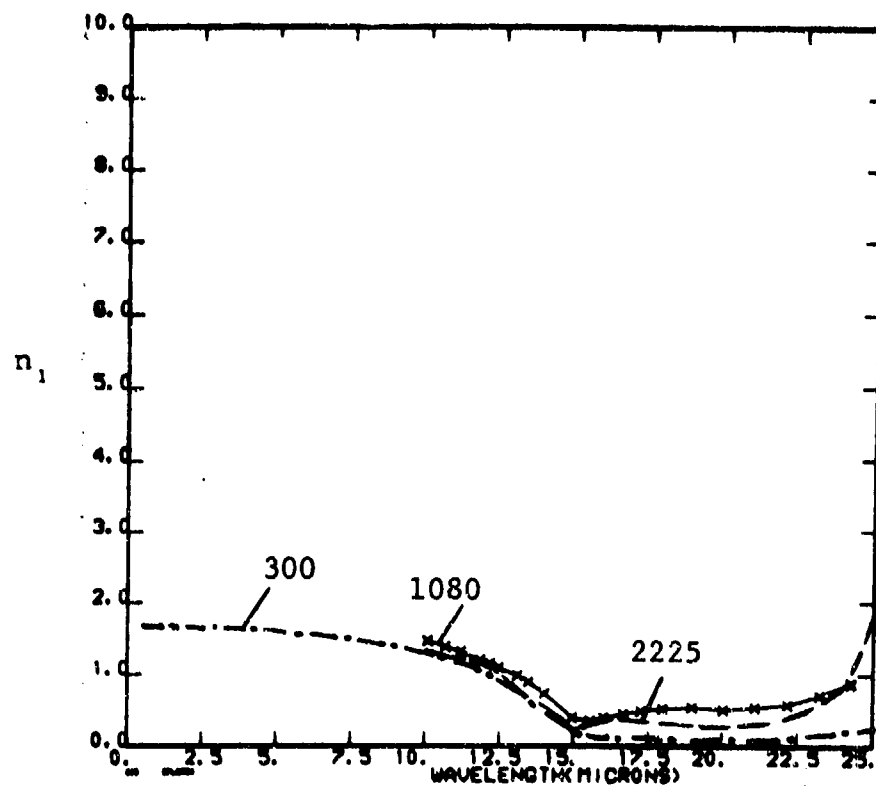
Figure 4-12. n_1 of MgO vs. λ for Three Different Temperatures.
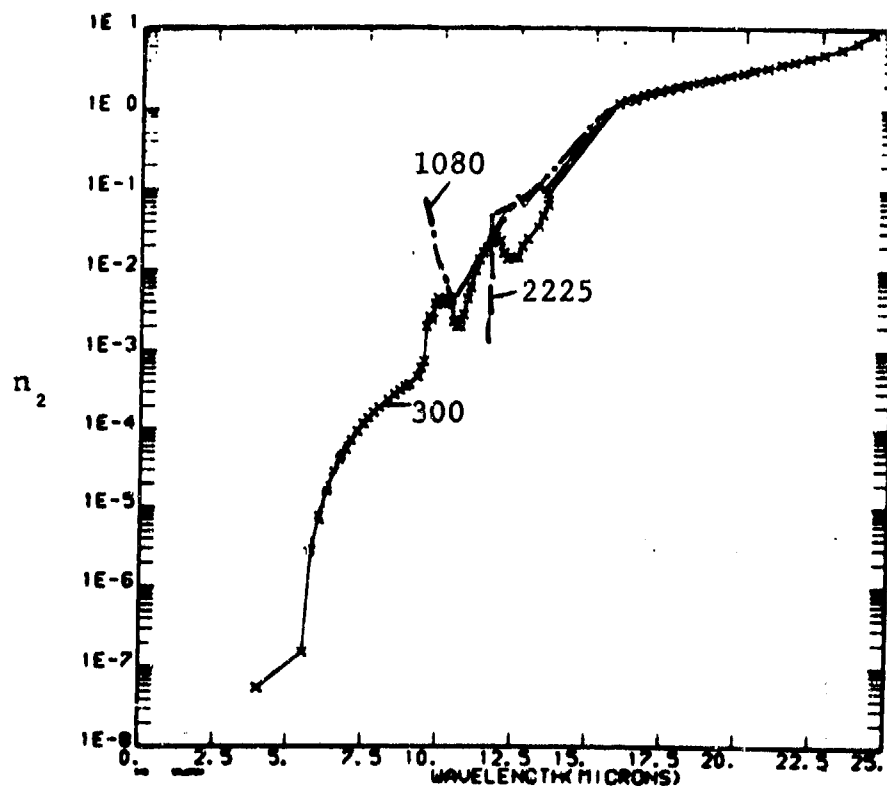
Figure 4-13. n_2 of MgO vs. λ for Three Different Temperatures.

4-18

show good agreement (see Figures 4-14 and 4-15). In addition,
Dowling and Randall's data at elevated temperature (573 K) show
little or no temperature dependency (see Figures 4-16 and 4-17).

ZrO_2

Whitson's report does not contain any data of n_1 and only
a limited set of n_2 at room temperature between 5 and 9 μm.
Thus, the data obtained by Dowling and Randall filled an important
gap. The reflectivity between 400 and 2200 cm^{-1} was measured
at room temperature and $573°K$. The spectral structure is similar
to that reported by Whitson, albeit lower by about 20%. The
results for n_1 and n_2 are shown in Figures 4-18 and 4-19,
respectively.

4.4 Numerical Results for Al_2O_3 and Carbon

The volume extinction, scattering and absorption coefficients
and the scattering phase function have been calculated for Al_2O_3
and carbon with a code developed by Dave (1972). These two
species are the most important particulate constituents in
present missile exhausts and possess very different optical and
geometrical properties. Thus, the results give insight into
the functional dependencies of β and M on size distributions,
wavelength and temperature. For Al_2O_3, the modified gamma
function was used for representing the size distribution 2 as
given in Figure 4-1, viz.

$$N(r) = N\left[.0551 \; \gamma \; e^{-.004r^4}\right]$$

4-19
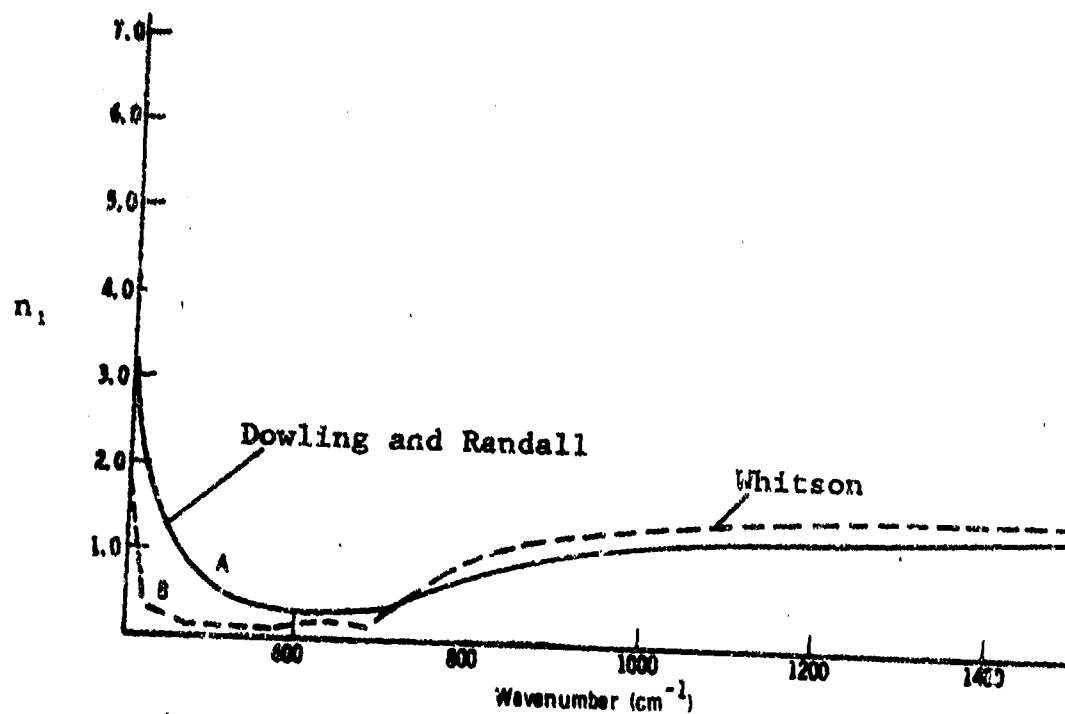
Figure 4-14. Comparison of Index of Refraction (n_1) for MgO.
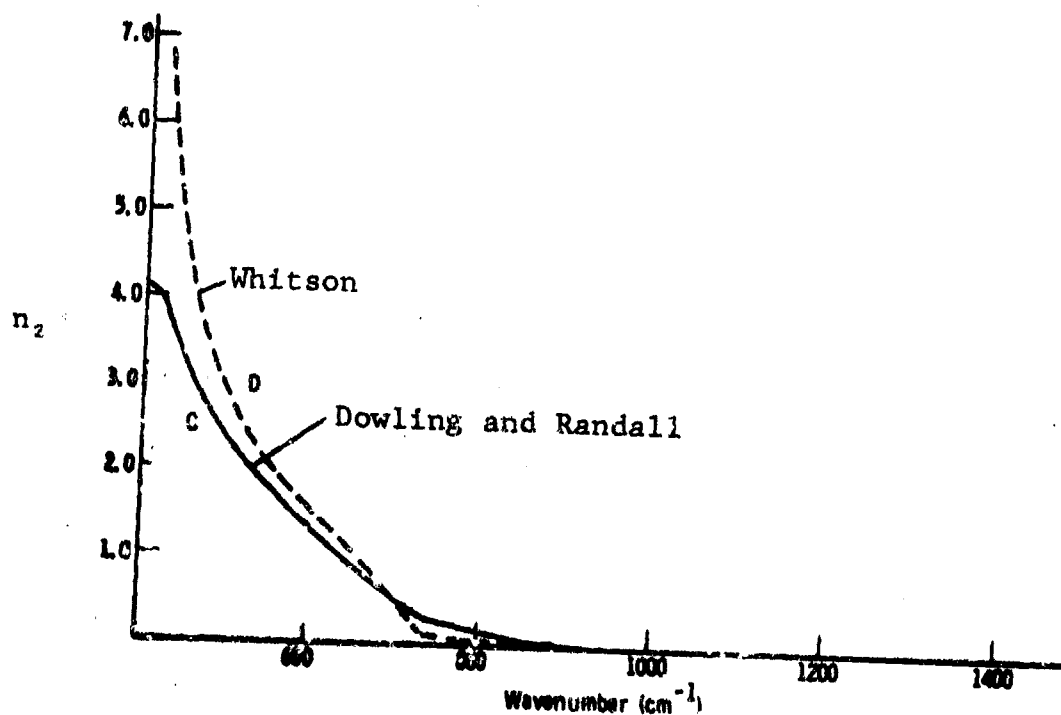
Figure 4-15. Comparison of Absorption Index (n_2) for MgO.
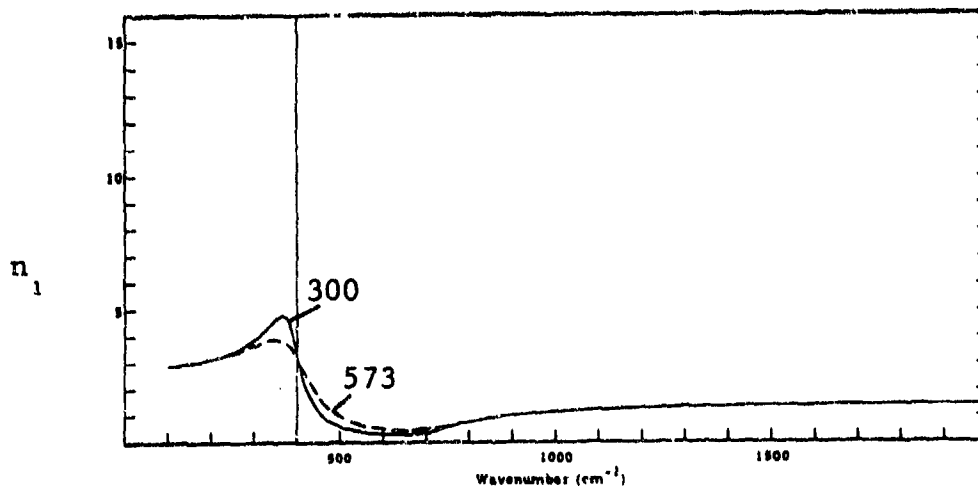
Figure 4-16. The Index of Refraction (n_1) of MgO from 400 cm^{-1} to 2000 cm^{-1} as Derived by Classical Dispersion Analysis (T = 300°K).
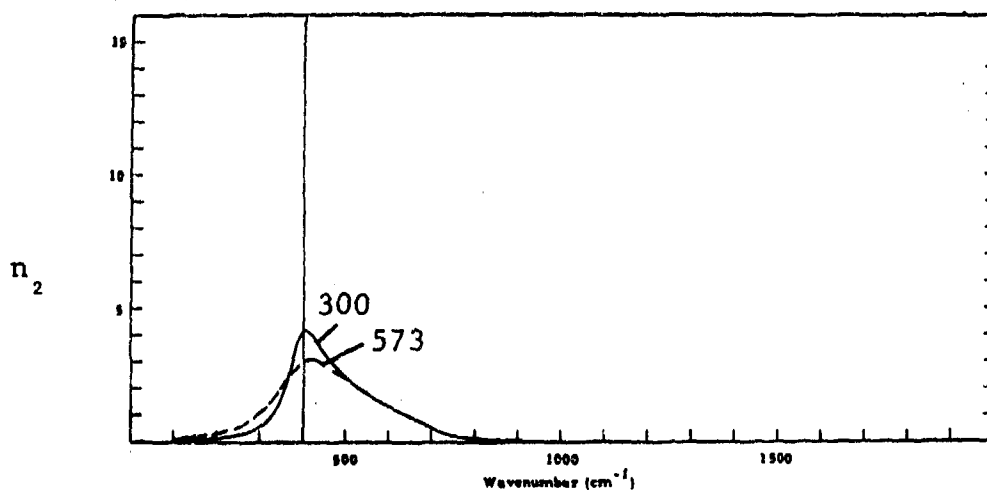
Figure 4-17. The Absorption Index (n_2) of MgO from 400 cm^{-1} to 2000 cm^{-1} as Derived by Classical Dispersion Analysis (T = 300°K).

4-21
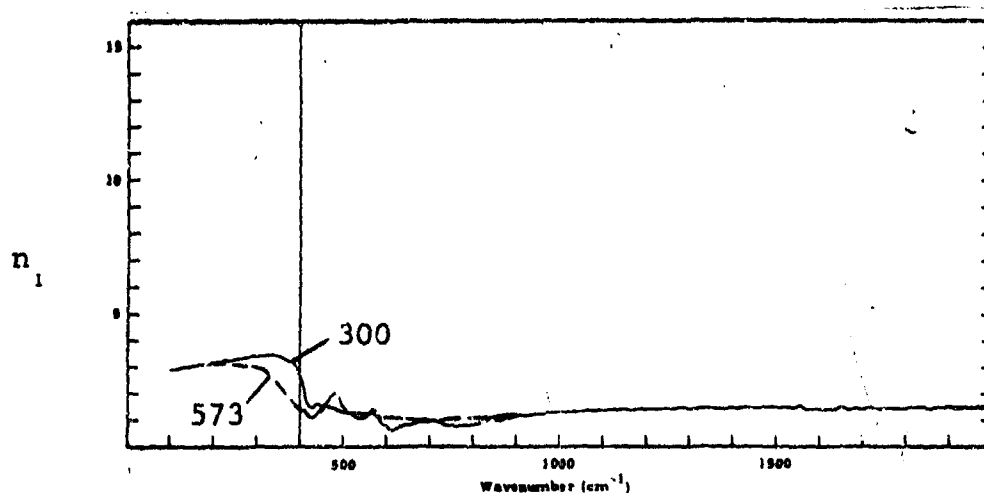
Figure 4-18. The Refractive Index (n_1) of ZrO_2 from 400 cm^{-1} to 2000 cm^{-1} as Determined from a Kramers-Kronig Analysis of the Reflectivity Data.
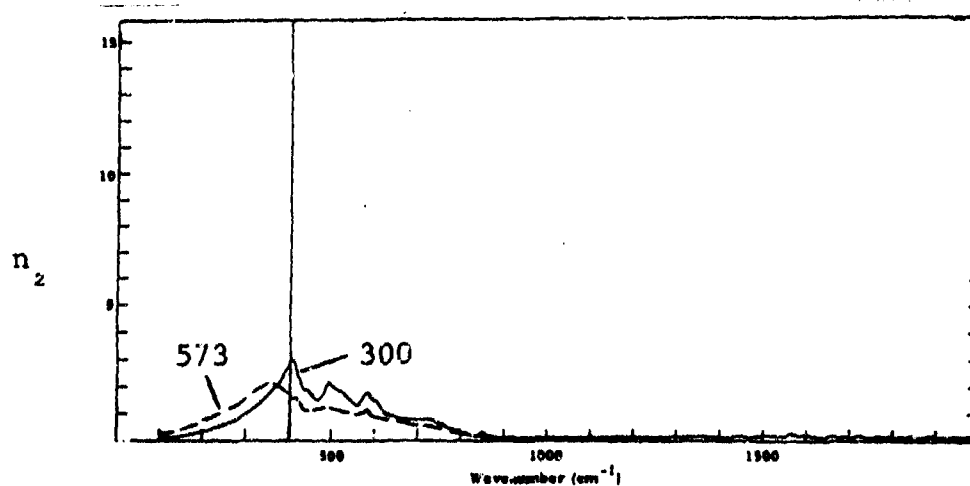
Figure 4-19. The Absorption Index (n_2) of ZrO_2 from 400 cm^{-1} to 2000 cm^{-1} as Determined from a Kramers-Kronig Analysis of the Reflectivity Data.

The total number of particles chosen was $10^6 \, cm^{-3}$ which corresponds to a mole fraction of about 30% when the mean radius is 5 μm. The min and max radii chosen were 1 and 9 μm, respectively. The input for a_{min}, a_{max}, n_1 and n_2 as a function of λ for a temperature of 1773°K are given in Table 4-2.

TABLE 4-2. INPUT PARAMETERS USED FOR Al_2O_3

λ(μm)	a_{min}	a_{max}	n_1	n_2
1	6.29	56.55	2	1.5^{-3}
3	2.09	18.85	2	2.0^{-3}
5	1.26	11.31	2	6.0^{-3}
7	.90	8.08	1.5	1.8^{-2}
9	.70	6.28	1.2	8.0^{-2}
11	.57	5.14	.5	.3
13	.48	4.35	.3	1.0
15	.42	3.77	.3	2.5
17	.37	3.33	.5	6.0
19	.33	2.98	4.0	.6
21	.30	2.69	3.5	.8
23	.27	2.46	3.0	6.0
25	.25	2.26	5.0	1.0

The results for the volume extinction, scattering and absorption coefficients and albedo ($\bar{\omega} = \beta_{sca}/\beta_{ext}$) as a function of λ (in steps of 2 μm) are listed in Table 4-3 and the angular scattering functions $M(\theta)$ as functions of θ are shown in Figures 4-20 through 4-32. It can be seen that the scattering becomes more and more isotropic as the wavelength increases. This is also shown in Figure 4-33, where the ratio of the side to forward scattering component is plotted vs. λ.

TABLE 4-3. Results for β_{ext}, β_{sca}, β_{abs} and $\bar{\omega}$ as a Function of λ for $A\ell_2O_3$ Particles in Rocket Plume Exhaust at 1773K.

$\lambda(\mu m)$	β_{ext}	β_{sca}	β_{abs}	$\bar{\omega}$
1	2.182	1.961	.221	.899
3	2.374	2.237	.138	.942
5	2.517	2.259	.258	.897
7	2.983	2.550	.433	.855
9	1.641	.893	.748	.544
11	1.800	1.164	637	.647
13	2.683	1.877	.806	.700
15	3.890	3.331	.559	.856
17	2.760	2.637	.123	.955
19	2.848	1.540	1.307	.541
21	2.941	1.499	1.442	.510
23	2.760	2.217	.543	.803
25	2.808	1.584	1.224	.564

The dependency of β_{ext}, β_{sca}, β_{abs} and $M(\theta)$ on the temperature is not expected to be strong, since n_1 and n_2 do not show large variations due to the temperature. As will be seen for carbon particles, relatively large variations in n_2 due to temperature produce only moderate variations in the coefficients and negligible ones in the scattering function. Similar results for the efficiency factors of single aluminum particles were also found by Plass (1965).
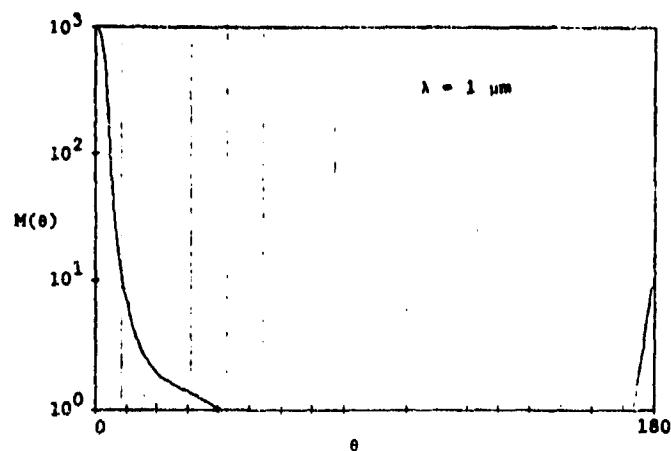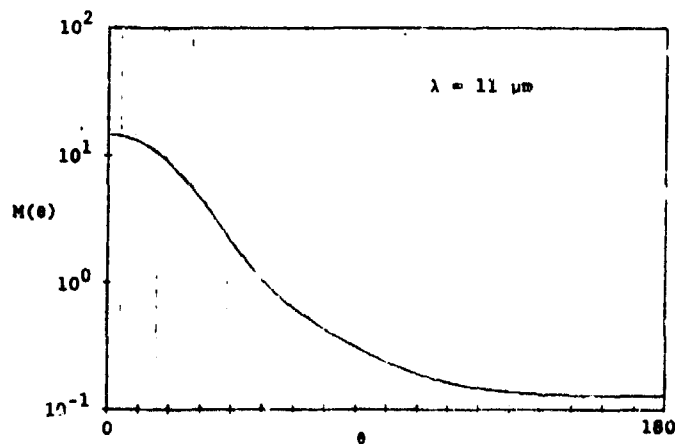
Figure 4-20. Angular Scattering Phase Function $M(\theta)$
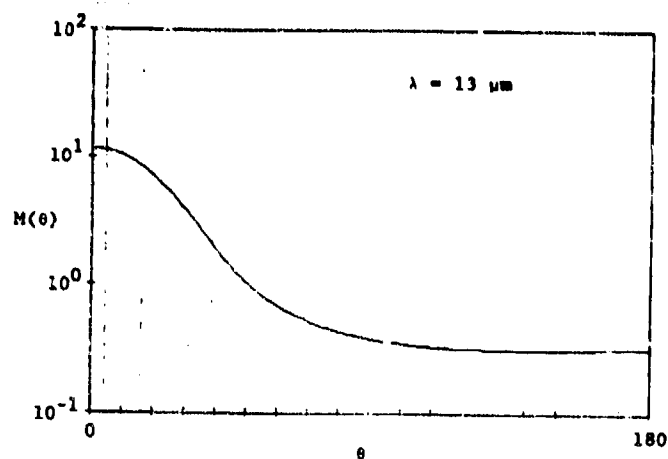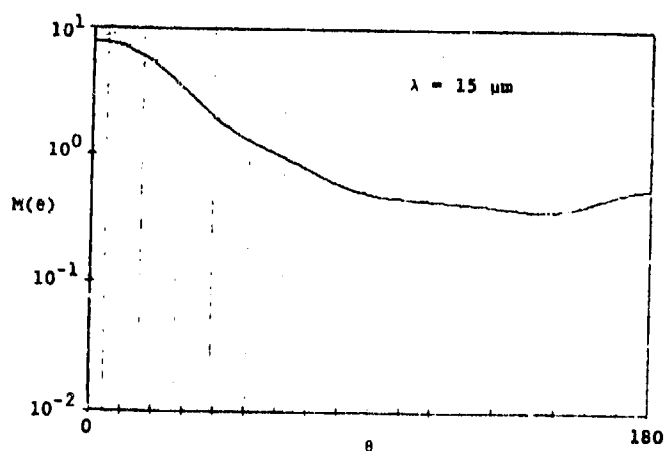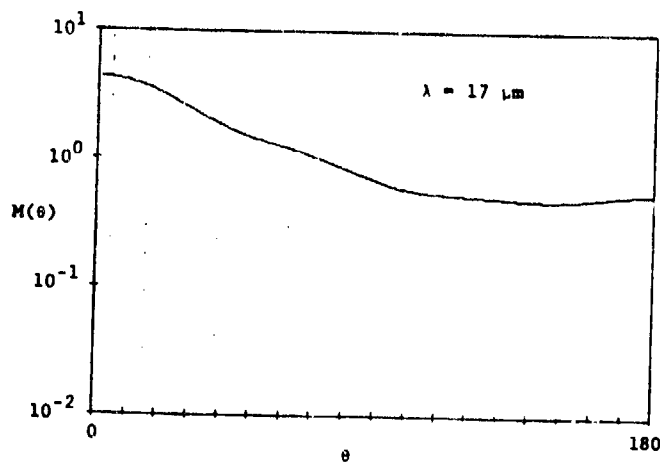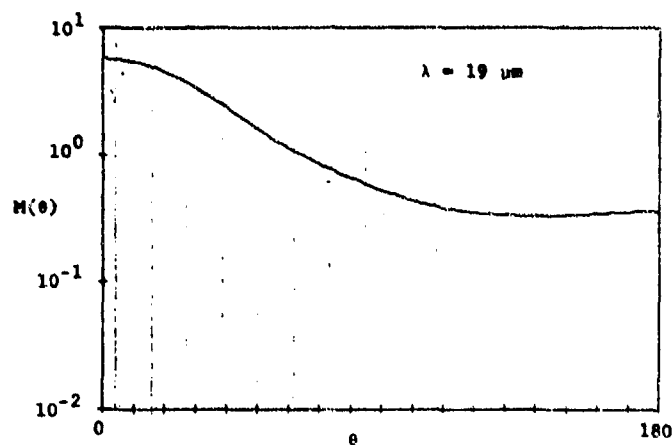for Al_2O_3 at $\lambda = 1$ μm.
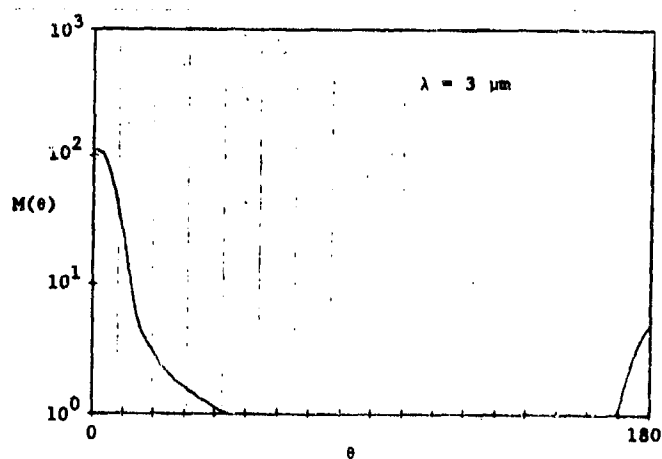
Figure 4-21. Angular Scattering Phase Function $M(\theta)$
for Al_2O_3 at $\lambda = 3$ μm.
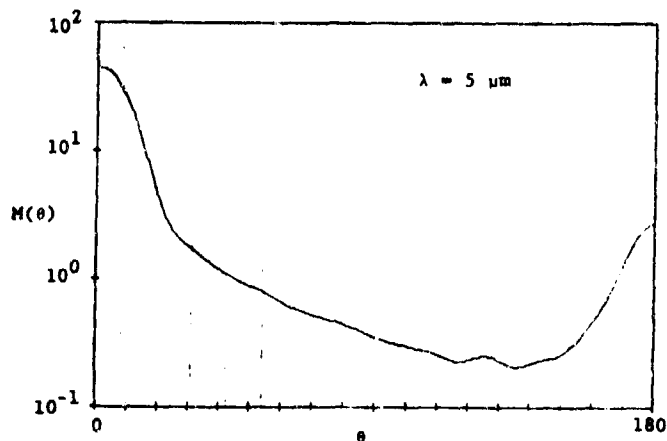
Figure 4-22. Angular Scattering Phase Function $M(\theta)$
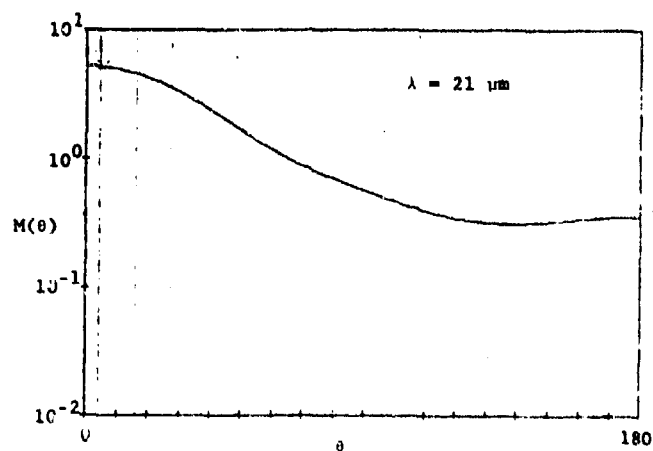for Al_2O_3 at $\lambda = 5$ μm.

4-25
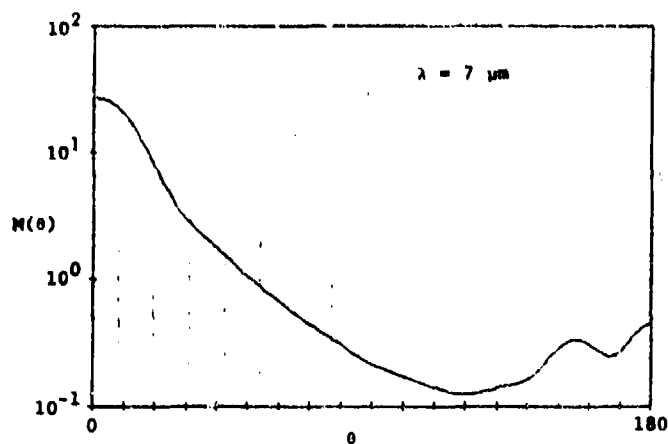
Figure 4-23.   Angular Scattering Phase Function $M(\theta)$
for $A\ell_2O_3$ at $\lambda = 7\,\mu m$.
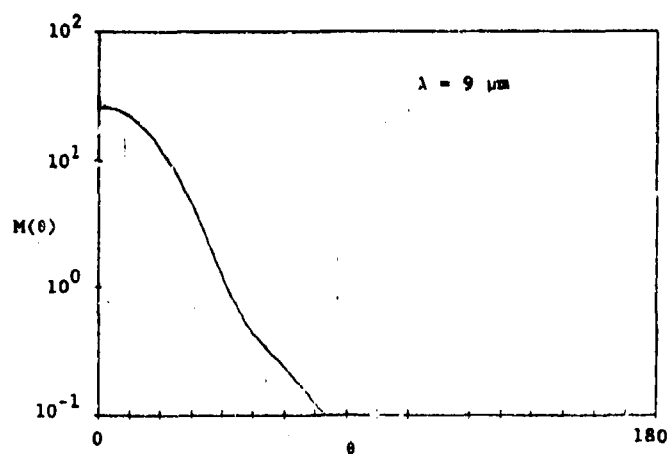
Figure 4-24.   Angular Scattering Phase Function $M(\theta)$
for $A\ell_2O_3$ at $\lambda = 9\,\mu m$.

Figure 4-25.   Angular Scattering Phase Function $M(\theta)$
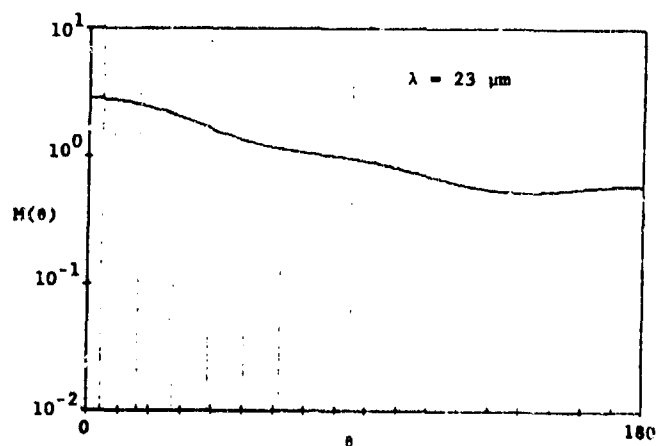for $A\ell_2O_3$ at $\lambda = 11\,\mu m$.

4-26

Figure 4-26.   Angular Scattering Phase Function $M(\theta)$
for $A\ell_2O_3$ at $\lambda = 13\,\mu m$.

Figure 4-27.   Angular Scattering Phase Function $M(\theta)$
for $A\ell_2O_3$ at $\lambda = 15\,\mu m$.

Figure 4-28.   Angular Scattering Phase Function $M(\theta)$
for $A\ell_2O_3$ at $\lambda = 17\,\mu m$.

4-27

Figure 4-29. Angular Scattering Phase Function M(θ) for Al_2O_3 at $\lambda = 19\,\mu m$.

Figure 4-30. Angular Scattering Phase Function M(θ) for Al_2O_3 at $\lambda = 21\,\mu m$.

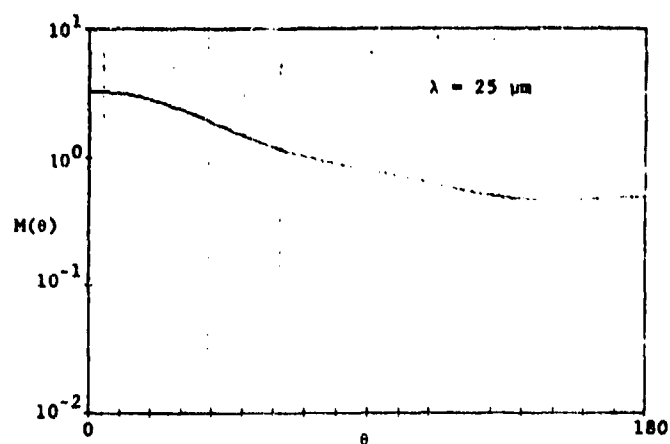Figure 4-31. Angular Scattering Phase Function M(θ) for Al_2O_3 at $\lambda = 23\,\mu m$.

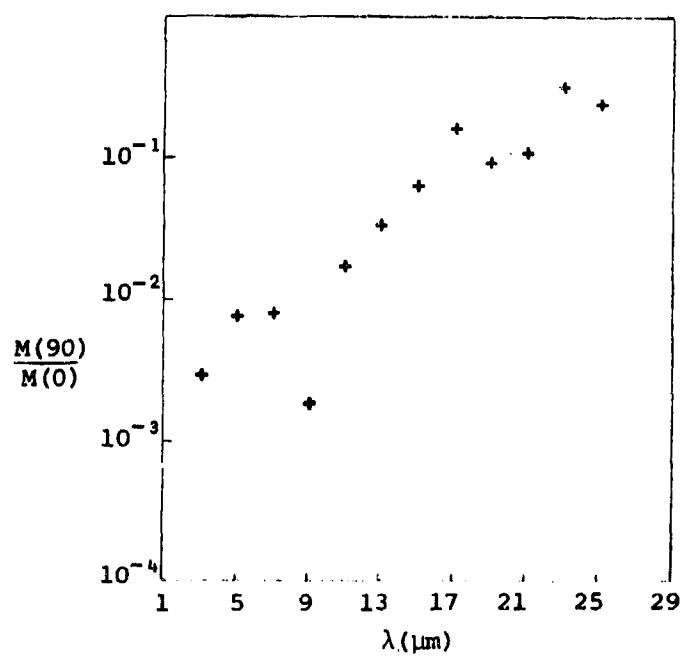Figure 4-32. Angular Scattering Phase Function $M(\theta)$ for $A\ell_2O_3$ at $\lambda = 25$ μm.

Figure 4-33. Ratio of Side to Forward Scattering Components vs. Wavelength for $A\ell_2O_3$

4-29

For the second particulate species, the volume coefficient and angular scattering functions have been calculated for carbon. The discontinuous power law was used to represent the size distribution as reported in the literature (Rochelle, 1967), viz.,

$$N(r) = N \qquad \text{for } .01 < r < .03 \; \mu m$$

$$N(r) = N(\frac{.03}{r})^2 \text{ for } .03 < r < 2 \; \mu m$$

The total number of particles was arbitrarily chosen to be $10^{13} cm^{-3}$ which corresponds to about 20% mole fraction ($r_{mean} \sim .02 \mu m$). The inputs for a_{min}, a_{max}, n_1 and n_2 are listed in Table 4-4. In order to study the influence

TABLE 4-4. INPUT PARAMETERS FOR CARBON PARTICLES

λ	a_{min}	a_{max}	n_1	n_2 (1000K)	n_2 (2500K)
1	.013	18.8	1.5	.3	.5
3	.0042	6.25	2.7	.37	1.1
5	.0025	3.77	3.0	.4	1.5
7	.0018	2.69	3.5	.4	1.9
9	.0014	2.09	3.7	.4	1.7
11	.0011	1.71	4.1	.32	1.3
13	.0010	1.45	4.4	.29	1.1
15	.0009	1.26	4.7	.23	.9
17	.0007	1.11	4.8	.21	.75
19	.0006	.99	4.8	.18	.6
21	.0006	.90	4.8	.15	.5
23	.0005	.82	4.8	.13	.4
25	.0005	.75	4.8	.12	.3

of the temperature, n_2 is given for 1000 and 2500K. The results of β_{ext}, β_{sca}, β_{abs} and $\bar{\omega}$ for 1000 and 2500 K are shown in Tables 4-5 and 4-6. Although the absorption index is higher by a factor of about 3 for the higher temperature throughout the wavelength region from 1 to 25 μm, the parameters β_{ext}, β_{sca}, β_{abs} and $\bar{\omega}$ are not greatly affected. The influence on the scattering phase function is even less, as can be seen in Figures 4-34 through 4-46.

As for Al_2O_3, we have used the ratio of the phase function at 90° and 0° to indicate the degree of isotropic scattering of C(s). The ratio is plotted in Figure 4-47 and compared with that of Al_2O_3.

TABLE 4-5. Results for β_{ext}, β_{sca}, β_{abs} and $\bar{\omega}$ as a Function of λ for C(s) Particles in Rocket Plume Exhaust (T = 1000 K, N = $10^{13}/cm^3$.

λ (μm)	β_{ext}	β_{sca}	β_{abs}	$\bar{\omega}$
1	1921	934	987	.486
3	2134	1107	1027	.519
5	2096	1075	1022	.513
7	2006	1039	968	.518
9	1885	962	922	.510
11	1698	812	886	.478
13	1578	800	778	.507
15	1407	717	690	.510
17	1305	661	643	.507
19	1308	693	614	.530
21	1229	746	484	.607
23	954	588	365	.616
25	819	475	344	.580

TABLE 4-6. Results for β_{ext}, β_{sca}, β_{abs} and $\bar{\omega}$ as a Function of λ for C(s) Particles in Rocket Plume Exhaust (T = 2500 K, N = $10^{13}/cm^3$).

$\lambda(\mu m)$	β_{ext}	β_{sca}	β_{abs}	$\bar{\omega}$
1	1927	936	992	.486
3	2137	1106	1031	.518
5	2095	1082	1013	.524
7	1977	1044	932	.528
9	1844	927	917	.503
11	1698	812	886	.478
13	1560	714	846	.458
15	1415	610	805	.431
17	1283	520	763	.405
19	1198	481	717	.402
21	1090	461	629	.423
23	913	397	517	.435
25	777	327	450	.421
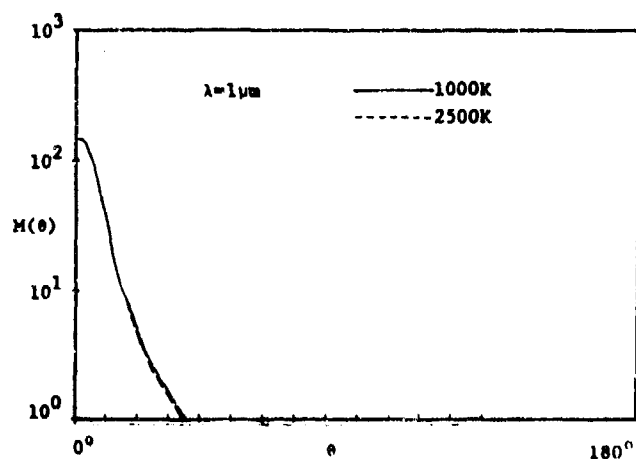
Figure 4-34. Angular Scattering Phase Function $M(\theta)$ for Carbon Particles at λ = 1 μm.
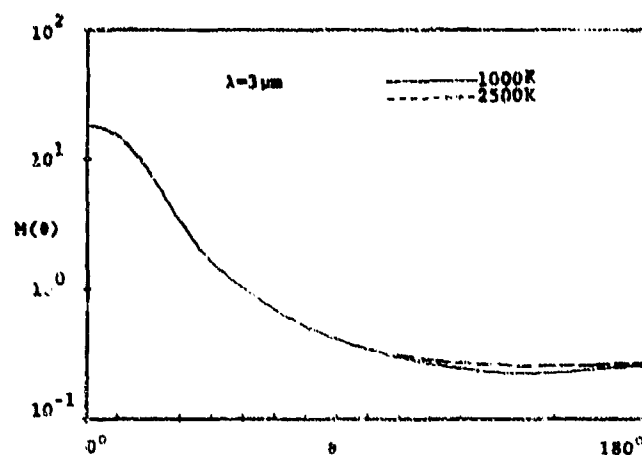
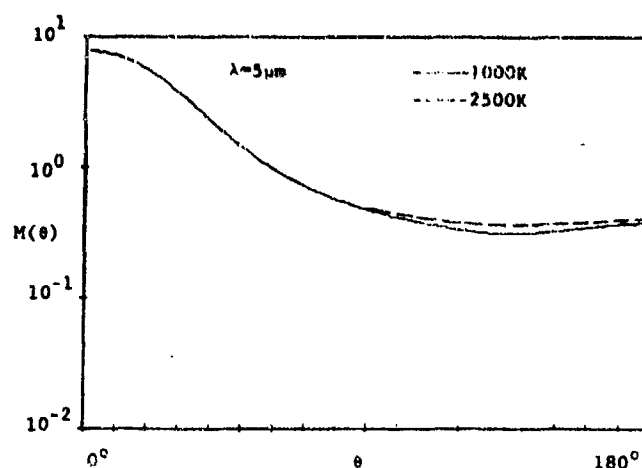Figure 4-35. Angular Scattering Phase Function M(θ) for Carbon Particles at λ = 3 μm.

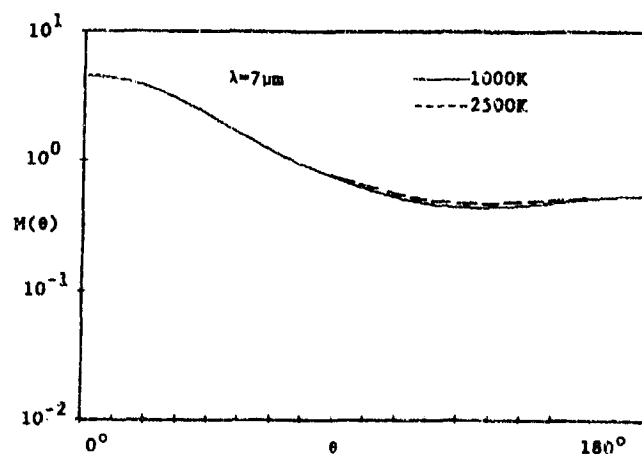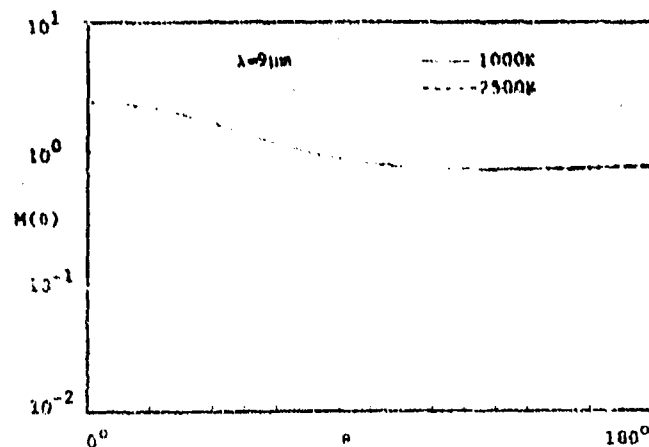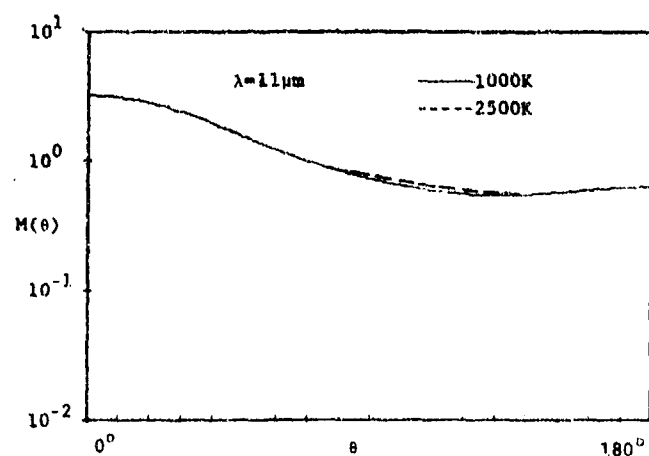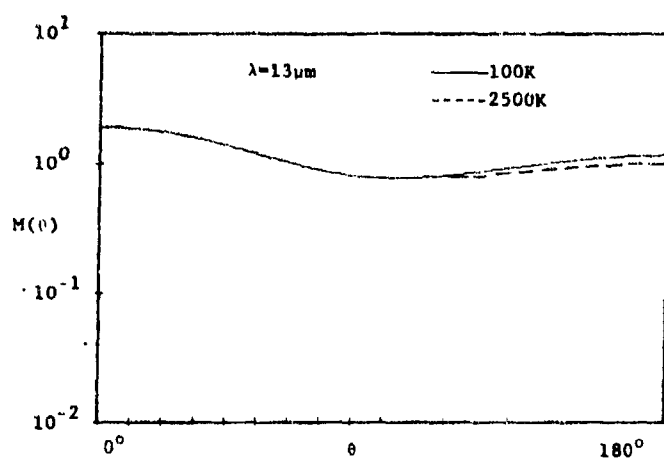Figure 4-36. Angular Scattering Phase Function M(θ) for Carbon Particles at λ = 5 μm.

Figure 4-37. Angular Scattering Phase Function M(θ) for Carbon Particles at λ = 7 μm.

Figure 4-38. Angular Scattering Phase Function M(θ) for Carbon Particles at λ = 9 μm.

Figure 4-39. Angular Scattering Phase Function M(θ) for Carbon Particles at λ = 11 μm.

Figure 4-40. Angular Scattering Phase Function M(θ) for Carbon Particles at λ = 13 μm.
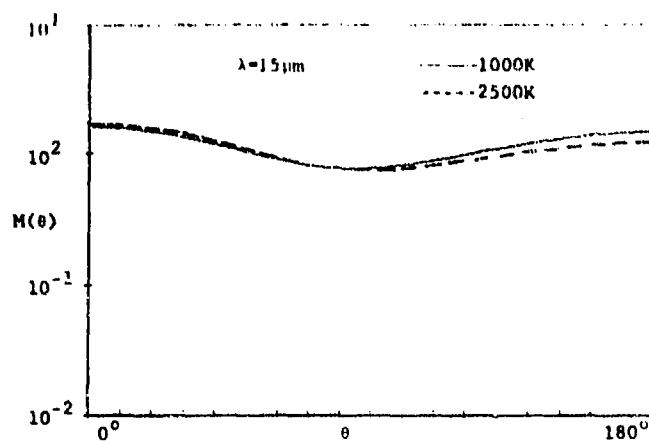
Figure 4-41.   Angular Scattering Phase Function $M(\theta)$
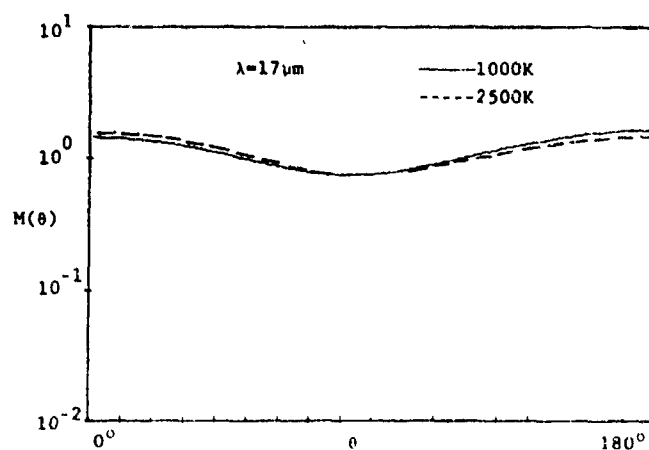   for Carbon Particles at $\lambda = 15 \, \mu m$.

Figure 4-42.   Angular Scattering Phase Function $M(\theta)$
                for Carbon Particles at $\lambda = 17 \, \mu m$.

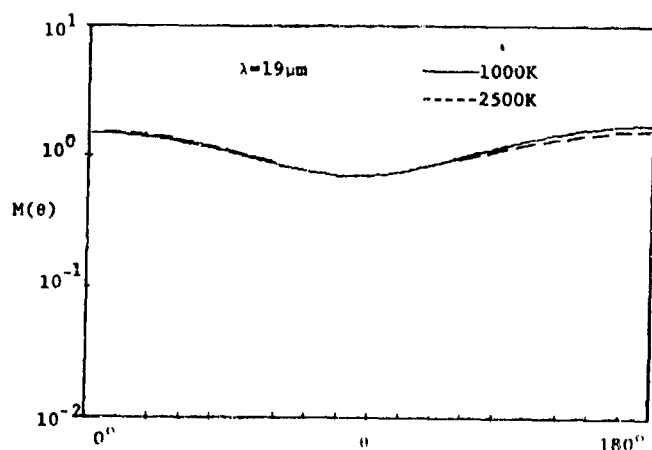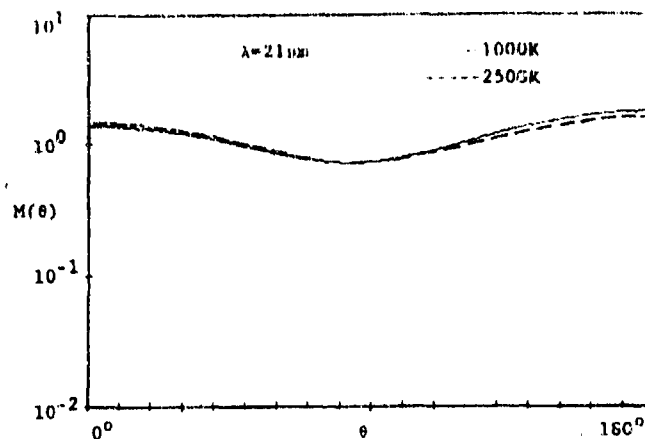
Figure 4-43.   Angular Scattering Phase Function $M(\theta)$
                for Carbon Particles at $\lambda = 19 \, \mu m$.

Figure 4-44.   Angular Scattering Phase Function M(θ)
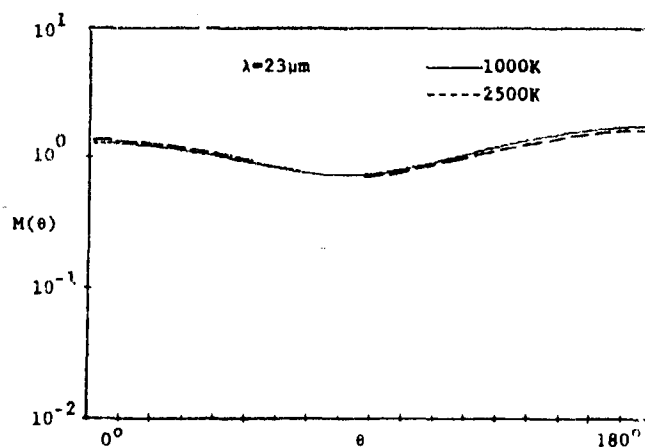   for Carbon Particles at λ = 21 μm.

Figure 4-45.   Angular Scattering Phase Function M(θ)
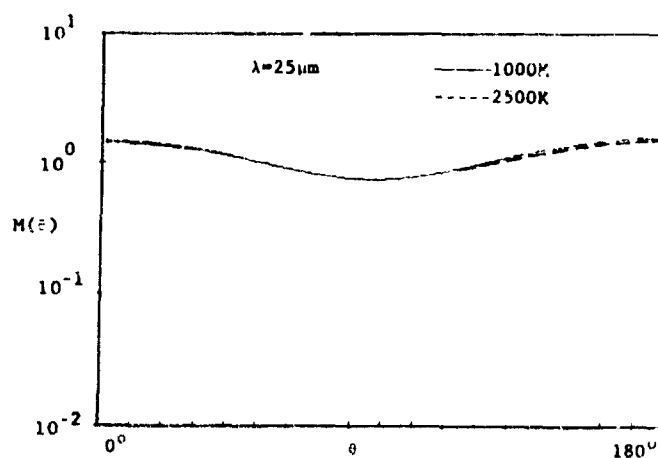   for Carbon Particles at λ = 23 μm.

Figure 4-46.   Angular Scattering Phase Function M(θ)
               for Carbon Particles at λ = 25 μm.

4-36
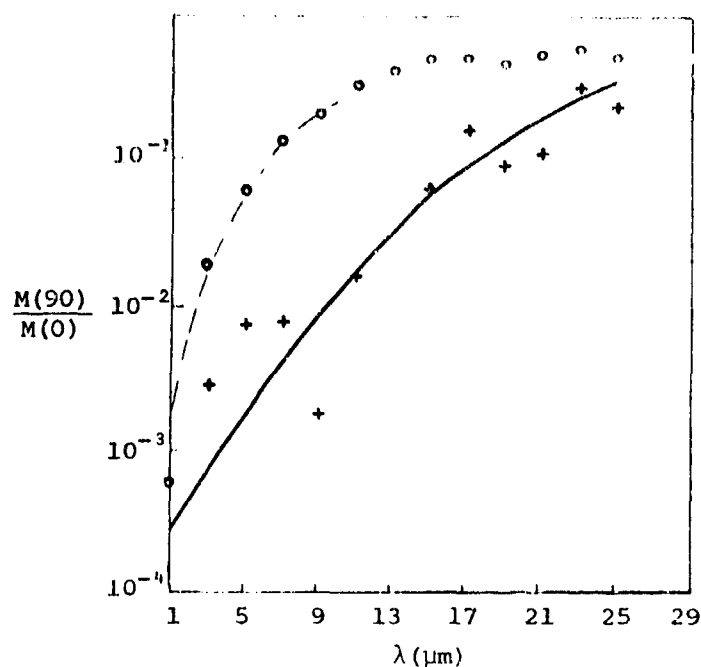
Figure 4-47. The Ratio of the Phase Function at
90° and 0° Scattering Angle as a
Function of λ_a for $A\ell_2O_3$ (+ — +)
and C(s) (o --- o).

4.5 Recommended Data File and Update Procedure

Based on the studies of the scattering properties of
particles performed during Subtask IA it is recommended that
SIRRM shall include

> (1) a permanent Data File of $n_1^s(\lambda,T)$, $n_2^s(\lambda,T)$
> $\beta_{ext}^{s,d}(\lambda,T)$, $\beta_{ext}^{s,d}(\lambda,T)$ and $M^{s,d}(\lambda,\Theta,T)$ for
> each species s and for each size distribution
> d; (this Data File may be minimized to as few
> temperatures and size distributions as indicated
> by experience);

(2) a subroutine that allows the user to update this Data File or add to it as new optical parameters ($n_1(\lambda, T)$, $n_2(\lambda, T)$ and size distributions) become available;

(3) a subroutine that compares the size distribution as calculated by the JANNAF flow field with those stored in the Data File and that will indicate to the user whether or not the stored size distribution(s) is (are) sufficient. We consider also the option of an automatic updating.

The advantages of the recommended approach are the following:

- Computer time is minimized by using a stored Data File;

- Storage requirements are minimized by using as few size distributions for each species as possible;

- Flexibility is maintained by allowing the user to update the Data File at his discretion;

- Indication is given to the user before execution whether an update of the Data File in terms of new and/or additional size distributions is necessary.

A tentative logic flow diagram of the recommended approach is shown in Figure 4-48. After the JANNAF flow field is read in and the relevant flow field positions for the line-of-sight calculations are determined, a subroutine calculates the analytical expression for the size distributions for each position. This is necessary since the JANNAF flow field does not give the analytical expression but does provide the number density for several specific particle sizes (private communications, S. Dash, May 1979). Different analytical expressions will be used,
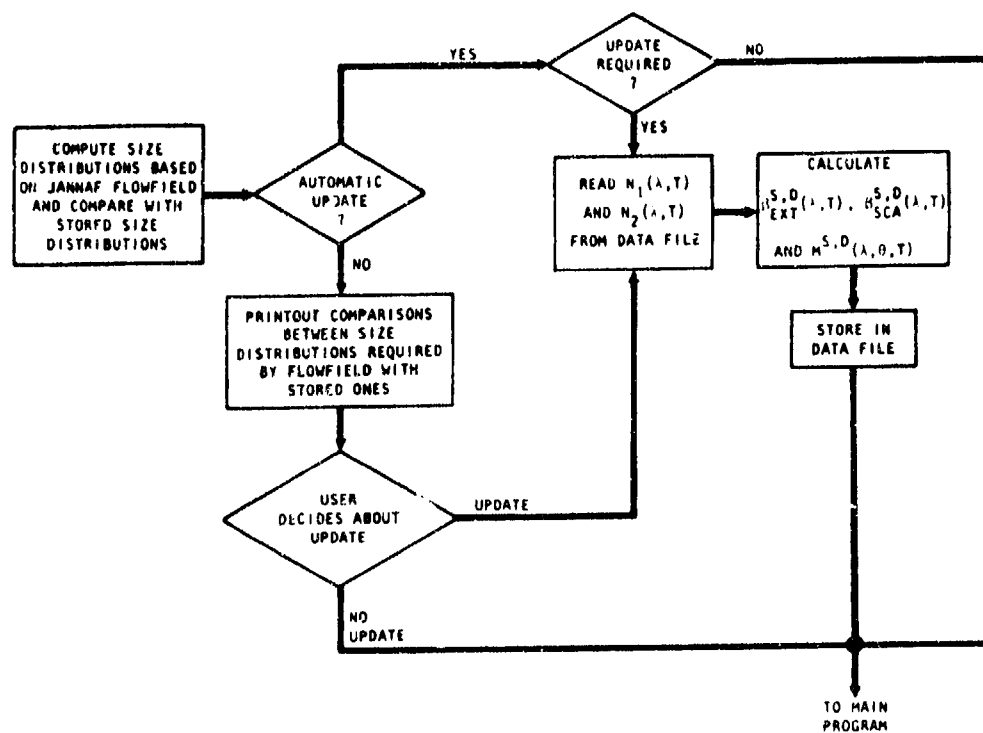
4-38

Figure 4-48.   Logic Flow Diagram of Data File Update Procedure

such as the discontinuous power law for particles with very small radii (carbon) and modified gamma function for particles with larger radii ($A\ell_2O_3$, etc.)

The computed size distributions will be compared with those already stored in the Data File. If the differences are minor (criteria must yet be established) no update is required. If the differences are major, β_{ext}, β_{sca} and $M(0)$ may have to be calculated and stored in the Data File. If the decision for an update is desired to be automatic (probably a default input), SIRRM will read the appropriate n_1 and n_2 and will calculate β_{ext}, β_{sca} and $M(\theta)$. If the decision is not to be automatic, the user has the option whether or not new values of β_{ext}, β_{sca} and $M(\theta)$ should be calculated. As more experience is gained about the influence of different size distributions on the radiation field using the six-flux and N-flux models, the decision about updating the Data File may become straightforward.

REFERENCES

Arduini, R. F. and B. Barkstrom, (1978) "Application of the Diffusion Approximation to the Transfer of Visual Radiation in Clouds of Finite Size", being published.

Barkstrom, B., (1976) JQSRT 16, 725

Bellman, R.E. et al (1963) Icarus 1, 297

Bellman, R.E. et al (1965) Icarus 4, 119

Bellman, R.E. et al (1966) JQSRT 6, 479

Bellman, R.E. et al (1969) Icarus 11, 417

Bellman, R.E. et al (1973) JQSRT 13, 1273

Bobco, R.P., (1967) J. Heat Transfer C89, 313

Busbridge, I.W. (1960) "The Mathematics of Radiative Transfer", Cambridge, Uni. Press. London

Busbridge, I.W. (1967) Astrophys J. 149, 195

Canosa, J. and H. R. Penafiel (1973) JQSRT 13, 21

Case, K., and P. Zweifel (1967) "Linear Transport Theory", Addison-Wesley, Palo Alto

Carlson, D.J. et al (1965) "Study of Thermal Radiation, Particle Impingement Heating and Flow Field Analysis of Solid Propellant Rocket Exhausts." Aeronutronic P-15245 (U),

Carlstedt, J.L. and T.W. Mullikin, (1966) Astrophys. J. Suppl. 12, 449

Chandrasekhar, S. (1950) "Radiative Transfer" (Oxford, Uni. Press. London)

Chandrasekhar, S., (1958) Proc. Nat. Acad. Scie. 44, 933

Chin, J. H. and S. W. Churchill, (1965) J. Heat Transfer, p. 167

Chou, Y.S., (1978) Appl. Opt. 17, 364

Chu, C.M., and S. Churchill (1955) J. Phys. Chem. 59, 855

Chu, C.M. et al (1963) "Numerical Solution for Multiple Aniso-
    tropic Scattering," in "Electromagnetic Scattering," M.
    Kerker, Editor, The MacMillan Co., New York

Collins, D.G. and M.B. Wells (1965) Rep. RRA-T54 (Radiation Res.
    Associates, inc. Ft. Worth, Texas)

Collins, D.G. et al (1972) Appl. Opt. 11, 2684

Crosbie, A., and T. Linsenbardt, (1976) JQSRT 19, 257

Dash, S. (1979) Private Communications

Danielson, R.E., et al (1969) J. Atm. Scie. 26, 1078

Dave J. V., (1964) Astrophys, J. 140, 1292
Dave J. V., (1969) Applied Optics 8, 155
Dave J. V., (1970) Applied Optics 9, 2673
Dave J. V., (1970B) Applied Optics 9, 1888
Dave J. V., and J. Gazdag (1970) Applied Optics 9, 1457
Dave J. V., (1972) Development of Programs for Computing
    Characteristics of Ultraviolet Radiation, Technical Report
    under Contract No. NAS5-21680

Davison, B., (1958) "Neutron Transport Theory" Oxford, Uni. Press
    London

Dawbarn, R. (1978) "Aluminum Oxide Particles Produced by Solid
    Rocket Motors" ARO, Inc., AFML-TR-78-190; also Proc. USAF/
    NASA Intern. Spacecraft Contam. Conf, USAF AC., Colorado
    Springs

Deirmendjian, D., (1969) "Electromagnetic Scattering on Spherical Polydispersions", New York, American Elsevier, p. 290

Deuze, J. L. et al (1973) Nouv. Rev. Optique, $\underline{4}$, 307

Domoto, G. A., JQSRT $\underline{14}$, 935 (1974)

Dowling, J.M. and C.M. Randall (1977) "Infrared Emissivities of Micron-Sized Particles of C, MgO, $A\ell_2O_3$, and ZrO_2, "AFRPL-TR-77-14

Fishburne, E., (1977) "Effects of Solid Particulates on Exhaust Plume Radiation, "ARAP Report No. 304

Fontenat, J.E. (1965) AIAA J. $\underline{3}$, 970

Grant, I.P. and G.E. Hunt (1969), Proc. Roy, Soc. London A $\underline{313}$,183

Gulrajani, B.K., (1964) "Analysis of Radiant Heat Transfer from Exhaust Plume of a Solid Propellant Rocket," Boeing Report D2-30861-1

Hansen, J.E. (1969), J. Atm. Science $\underline{26}$, 478
  Astrophys, J. $\underline{155}$, 565; $\underline{158}$, 337
Hansen, J.E. (1971), J. Atm. Science $\underline{28}$, 1400; JQSRT $\underline{11}$, 809
Hansen, J. and L.Travis (1974) Space Science Reviews $\underline{16}$,527

Hartel, W. (1940) Das Licht $\underline{40}$, 141

Heasley, J.N. (1977) JQSRT $\underline{18}$, 541

Herman, B.M. (1963), Ph.D Thesis, U. Arizona
Herman, B.M. et al (1965) J. Atm. Sci, $\underline{22}$, 559
Herman, B.M. et al (1970) J. Atm. Sci, $\underline{28}$, 419

Hovenier, J.W. (1971), Astron. Astrophys. $\underline{13}$, 7

Hunt, J.D., (1966) "Thermal Radiation from Solid Propellant Exhaust Plumes", Boeing Report, D5-12260

Irvine, W. M., (1964), Bull. Astron. Inst. Neth. 17, 266

Irvine, W. M., (1975) Icarus 25, 175

Irvine, W. M., (1965) JOSA 55, 16

Irvine, W. M., (1969) J. Atm. Sci. 26, 973

Jefferies, J. T., (1955) Optica Acta 2, 109 and 163

Kaper, H. G. et al (1970), J. Comp. Phys. 6, 288

Kattawar, G. W., and G. N. Plass (1967) Applied Optics 6, 1377

Kattawar, G. W., and G. N. Plass (1971) Applied Optics 10, 74

Kattawar, G. W., and G. N. Plass (1973) Applied Optics 12, 1071

Kerker, M., (1969) "The Scattering of Light and Other Electro-
    magnetic Radiation", Academic Press, New York

Kofink, W. (1967) "Development in Transport Theory", Academic
    Press, New York

Kordes, E. (1960) "Optische Daten" Verlag Chemie, GMBH

Krascella, N.L., (1966) JQSRT 5,245

Krook, M.(1955) Harvard College Observatory, Under Contract
    AF 19(604)-146, Geophys. Res. Director., AFCRC

Kuscer, I. and N. J. McCormick (1974) Int. Conf. Rad. Rem. Probing
    Atmos. pp. 196-226

Lacis, A.A., and J. E. Hansen (1974) J. Atm. Sci. 31, 118

Lenoble, J. (1956), Rev. Opt. 35, 1

Leung, C.M., (1976) JQSRT 16, 559

Leung, C.M., (1975) Astrophys. J. 199, 340

Liou, K. N., (1974) J. Atm. Sci. 31, 1473

Liou, K. N., (1973) J. Atm. Sci. 30, 1303

Love, T. J., and R. J. Grosh (1965) J. Heat Transfer, p. 161

Marchuk, G.I., and G.A. Mikhailov (1967) Atmosph. Ocean. Phys. 3, 258; 3, 394

McKee, T.B. and S. K. Cox (1974) J. Atm. Sci. 31, 1885

Mika, J.R. (1961) Nucl. Scie. Eng. 11, 415

Pahor, S. and I. Kuscer (1966), Astrophys. J. 143, 888

Piriou, B. (1966) Rev. Hautes Temp. et Refract. 3, 109

Plass, G.N. (1965) Applied Optics 4, 1616

Plass, G.N. and G.W. Kattawar (1968) Applied Optics, 7, 415

Plass, G.N. and G.W. Kattawar (1971) Applied Optics, 10, 738

Plass, G.N. and G.W. Kattawar (1973) Applied Optics, 12, 314

Poon, P.T.Y. and S. Ueno (1974) JQSRT 14, 85

Preisendorfer, R.W., (1965) "Radiative Transfer on Discrete Spaces: Pergamon Press, Oxford

Rieger, T.J., et al (1974) "Studies of IR Signatures on Low Altitude Rocket Exhaust," Aerodyne Research Report ARI-RN-41

Rochelle, W.C. (1967) "Review of Thermal Radiation from Liquid and Solid Propellant Rocket Exhaust," NASA TM x-53579

Samuelson, R.E., (1969) Icarus 10, 258

Sanford, M.T., and T.A. Pauls (1973), Astrophys. J. 179, 875

Sobolev, V.V., (1972) "Light Scattering in Planetary Atmospheres," Pergamon Press

Sobolev, V. V., (1973) Astrofizika 8, No. 2

Stull, V. R., and G. N. Plass (1960) JOSA 50, 121

Tesner, P. A., (1959) Seventh Int. Symp. Comb.

Twomey, S., et al (1966) J. Atm. Sci. 23, 289

Uesugi, A. and W.M. Irvine (1970), Astrophys. J. 161, 243

Van Blerkom, D., (1971) Astrophys. J. 166, 235

Van de Hulst, H.C., (1957) "Light Scattering by Small Particles,"
  New York, John Wiley and Sons, Inc., 470 pp.

Van de Hulst, H.C., and W.M. Irvine (1962), Mem. Soc. Roy.
  Sci., Liege, 15th, 7, 78

Van de Hulst, H.C., (1968), J. Comp. Phys. 3, 291

Van de Hulst, H.C., (1970), Astron. Astrophys. 9, 374; 9, 366;
  9, 359

Vanderbilt, D., and M. Slack (1976) "A Model for Emission and
  Scattering of Inrared Radiation from Inhomogeneous Combustion
  Gases and Particles," Grumman Research Department Memorandum
  RM-621

Viskanta, R. (1964) "Advances in Heat Transfer VIII" Academic Press,
  New York

Weinman, J.A., and P.J. Guetter (1972) J. Applied Meteor. 11, 136

Whitney, C., (1972) J. Atmos. Sci. 29, 1520

Whitney, C., (1974), JQSRT 14, 591

Whitson, M.E., (1975) "Handbook of the Infrared Optical Properties
  of $A\ell_2O_3$, C, MgO, and ZrO_2", SAMSO-TR-75-131

Wilson, K., et al. (1973) "Particle Radiation Effects", Lockheed
  Missiles & Space Co., B305283 and B324207.

Wing, G.M., (1962) "An Introduction of Transport Theory", J. Wiley
  New York

Wiscombe, W., (1977) J. Atmos. Sci. 34, 1408